University of Genoa

Polytechnic School

Ph.D. course in Science and Technologies for Electrical, Naval Engineering and Complex Mobility Systems

Curriculum: Electrical Engineering

Advanced Primary Controllers for Inverter Based Power Sources: Microgrids and Wind Power Plants

Supervisor

Prof. Renato Procopio

Candidate

Alessandro Giuseppe Labella

Abstract

The aim of this doctoral thesis is to present the research activity fulfilled during the Ph.D. studies.

The research project of the candidate was focused on two main cores.

The first core is centred in the microgrid area; in particular in islanded microgrid modelling and control. Firstly, the model was compared with experimental results collected in some facilities available at University of Genoa. Then traditional controllers for islanded microgrid are analysed and explored, proposing a new stability estimation procedure for droop controlled microgrid. Finally, a new control strategy based on Model Predictive Control (MPC) is proposed in order to collect many functionalities in just one control layer. MPC is widely used in MG environment, but just for power and energy management at tertiary level; instead here it is here proposed with an inedited use. Some experimental validations about this new methodology are obtained during a research period in Serbia and Denmark.

The second core is related with synthetic inertia for wind turbine connected to the main grid, i.e. frequency support during under-frequency transients. This aspect is very important today because it represents a way to increase grid stability in low inertia power systems. The importance of this feature is shared by all the most important Transmitter System Operators (TSO) all over the world.

INDEX

Abbreviations

CS	Critical Source
DER	Distributed Energy Resource
DG	Distributed Generation
EMS	Energy Management Strategy
FBL	FeedBack Linearization
FS	Frequency Support
MG	MicroGrid
MPC	Model Predictive Control
MPP	Maximum Power Point
MT	MicroTurbine
NCC	Nominal Current Capacity
NCS	Non-Critical Source
NO	Normal Operation
ODE	Ordinary Differential Equation
PCC	Point of Common Coupling
PLL	Phase Locked Loop
PMW	Power Management Strategy
POI	Point of Interconnection
PP	Power Priority
PV	PhotoVoltaic
RES	Renewable Energy Resource
RSR	Rotor Speed Recovery
SM	Smart Grid
SOC	State Of Charge
SP	SOC Priority
SPM	Savona Polygeneration Microgrid
SQ	Switchgear
VHIE	Variable Hidden Inertia Emulation
WT	Wind Turbine
WTG	Wind Turbine Generator

1 Introduction

The aim of this chapter is to introduce the structure, the goals, the contribution obtained and achieved during the Ph.D. studies.

1.1 Background

The need of reducing emissions in the electricity generation field, recent technological developments in the microgeneration domain, and electricity business restructuring are the main factors responsible for the growing interest in the use of microgeneration.

Electrical grids tend to be more distributed, intelligent, and flexible. New power-electronic equipment will dominate the electrical grid in the next decades. The trend of this new grid is to become more and more distributed and hence energy generation and consumption areas cannot be conceived separately. Nowadays, electrical and energy engineering must face a new scenario in which small distributed power generators and dispersed energy-storage devices have to be integrated together into the grid. The new electrical grid, also named Smart Grid (SG), will deliver electricity from suppliers to consumers using digital technology to control appliances at consumers' homes to save energy, thus reducing cost and increasing reliability and transparency. In this sense, the expected whole energy system will be more interactive, intelligent, and distributed. The use of Distributed Generation (DG) of energy systems makes no sense without using distributed storage systems to cope with the energy balances. Microgrids (MGs), are becoming important concepts to integrate DG and energy-storage systems. The concept has been developed to cope with the penetration of renewable-energy systems, which can be realistic if the final user is able to generate, store, control, and manage part of the energy that it will consume.

Today power generation comes essentially from large power plants mainly fuelled by fossil fuels, nuclear and hydroelectric power that operate through well-established transmission and distribution systems. Although these systems have offered efficient ser-vice around the world for over a century, the times are changing. Demand for energy is growing rapidly due to rapid social developments in many parts of the world, but also because modern digital economies increasingly depend on electricity availability. This dependence relationship imposes new structural developments in order to avoid network problems.

At the same time, modern societies have realized that, in order to combat climate change, it is necessary to reduce emissions. Optimum use of traditional sources has to underpin the development of production from non-traditional sources such as wind, solar, solar, geothermal, and biomass power plants. Thus, there is a great variety of energy sources whose integration and optimum use yield complex problems relevant to the design and management of electrical grids.

The impact of climatic conditions on the availability of wind and solar energy, together with the need to develop distributed facilities (e.g., domestic photovoltaic systems), further complicates the scenario, imposing the need for designing local networks capable of receiving and delivering electricity. In this connection, the power grid itself

is used in new ways. Instead of serving relatively small geographic areas with links to other regions to ensure security of supply, networks are currently used as energy-efficient channels for longer distances.

All these elements bring a change of paradigm that allows the final user to be not only a consumer but also a part of the grid. Consequently, it opens new possibilities and new solutions. Nowadays there is no a "winner" methodology yet among the many solutions proposed; this is because *i*) the market is still young and in fast evolution and *ii*) the variety and complexity in grids lead to different solutions.

1.2 Main Contribution

The main contributions of this thesis are summarised below:

- **Chapter 3** proposes a simplified, first harmonic model for a generic structure of MG characterized by its use of only electronic power converter interfaced generation. The main advantages of the proposed method lie in the model's simplicity and its reduced solving time, thanks to the limited number of necessary parameters to describe the system. Moreover, the developed formulation allows the avoidance of specific (and often licensed) software to simulate the system
- A new approach to evaluate the stability of a droop-controlled microgrid as stated in **Chapter 4**. It has a simple formulation that It does not require to find the final equilibrium point and to calculate the system matrix eigenvalues in that point as it is required in the (more widely used) small signal stability approach.
- An innovative control technique for the primary regulation of an islanded MG composed only by power converters and without any rotating electrical machine. The proposed method is based on the Model Predictive Control (MPC) technique and is deeply investigated in **Chapter 5**. The proposed control system is a decentralized one since each inverter is equipped with its own control system that requires only local measurements and has the advantage of avoiding any frequency or voltage deviations.
- **Chapter 6** proposes a new approach for the synthetic inertia of Wind Turbine Generators (WTGs) to ensure an effective impact on the system frequency avoiding unstable operation of the WTG and minimizing secondary frequency drop due to the rotor speed restoration. Furthermore, the chapter details the definition of the switching logics to activate and deactivate the frequency support controller and its implementation in available industrial controllers.

1.3 List of Publication

This Ph.D. has originated the following scientific publications on journals and conferences.

1.3.1 International journals

Bonfiglio, A., Brignone, M., Invernizzi, M., Labella, A., Mestriner, D., & Procopio, R. (2017). A simplified microgrid model for the validation of islanded control logics. *Energies*, *10*(8), 1141.

Bonfiglio, A., Delfino, F., Labella, A., Mestriner, D., Pampararo, F., Procopio, R., & Guerrero, J. M. (2018). Modeling and experimental validation of an islanded no-inertia microgrid site. *IEEE Transactions on Sustainable Energy*, *9*(4), 1812-1821.

Bonfiglio, A., Invernizzi, M., Labella, A., & Procopio, R. (2018). Design and Implementation of a Variable Synthetic Inertia Controller for Wind Turbine Generators. *IEEE Transactions on Power Systems*, *34*(1), 754-764.

Labella, A.; Filipovic, F.; Petronijevic, M.; Bonfiglio, A.; Procopio, R. (2020) An MPC Approach for Grid-Forming Inverters: Theory and Experiment. *Energies*, *13*, 2270.

1.3.2 International conferences

Bonfiglio, A., Delfino, F., Invernizzi, M., Labella, A., Mestriner, D., Procopio, R., & Serra, P. (2015, September). Approximate characterization of large Photovoltaic power plants at the Point of Interconnection. In *2015 50th International Universities Power Engineering Conference (UPEC)* (pp. 1-5). IEEE.

Labella, A., Mestriner, D., Procopio, R., & Brignone, M. (2017, March). A new method to evaluate the stability of a droop controlled micro grid. In *2017 10th International Symposium on Advanced Topics in Electrical Engineering (ATEE)* (pp. 448-453). IEEE.

Labella, A., Mestriner, D., Procopio, R., & Delfino, F. (2017, June). A simplified first harmonic model for the Savona Campus Smart Polygeneration Microgrid. In *2017 IEEE International Conference on Environment and Electrical Engineering and 2017 IEEE Industrial and Commercial Power Systems Europe (EEEIC/I&CPS Europe)* (pp. 1-6). IEEE.

Labella, A., Mestriner, D., Pampararo, F., & Procopio, R. (2017, October). Measurement campaign and experimental results of an islanded microgrid. In *2017 International Conference on energy and environment (CIEM)* (pp. 31-35). IEEE.

Bonfiglio, A., Gonzalez-Longatt, F. M., Labella, A., & Procopio, R. (2017, October). Implementation of primary frequency regulation on fully rated wind turbine generators. In *2017 International Conference on ENERGY and ENVIRONMENT (CIEM)* (pp. 316-320). IEEE.

Blanco, F., Labella, A., Mestriner, D., & Rosini, A. (2018, June). Model Predictive Control for Primary Regulation of Islanded Microgrids. In *2018 IEEE International Conference on Environment and Electrical Engineering and 2018 IEEE Industrial and Commercial Power Systems Europe (EEEIC/I&CPS Europe)* (pp. 1-6). IEEE.

Bonfiglio, A., Labella, A., Mestriner, D., Milani, F., Procopio, R., & Ye, Y. (2018, June). ITER Fast Discharging Units: A Black Box Model Approach for Circuital Simulations. In *2018 IEEE International Conference on Environment and Electrical Engineering and 2018 IEEE Industrial and Commercial Power Systems Europe (EEEIC/I&CPS Europe)* (pp. 1-7). IEEE.

Labella, A. (2019, March). A Novel Synthetic Inertia Control for Wind Turbine Integration into Traditional Grids. In *2019 Advances in Science and Engineering Technology International Conferences (ASET)* (pp. 1-6). IEEE.

Labella, A. (2019, March). Power Management Analysis in PV-BESS Islanded AC Microgrid. In *2019 11th International Symposium on Advanced Topics in Electrical Engineering (ATEE)* (pp. 1-6). IEEE.

Mestriner, D., Labella, A., Bonfiglio, A., Benfatto, I., Li, J., Ye, Y., & Song, Z. (2019, June). ITER Reactive Power Compensation Systems: analysis on reactive power sharing strategies. In *2019 IEEE International Conference on Environment and Electrical Engineering and 2019 IEEE Industrial and Commercial Power Systems Europe (EEEIC/I&CPS Europe)* (pp. 1-6). IEEE.

1.4 List of patents

1.4.1 Patents under review

Patent Application: ITALY – 07/08/2018

Application Number: 102018000007930

Title: Metodo e sistema di controllo di generatori non inerziali, in particolare di generatori eolici, mediante emulazione di inerzia

Patent Application: ITALY – 15/07/2019

Application Number: 102019000011739

Title: Metodo e sistema per il controllo di inverter in microreti

Patent Application: ITALY – 05/06/2019

Application Number: 102019000008163

Title: Metodo e sistema per valutare la stabilità di microreti in modalità

2 Microgrid State of the Art[1]

The aim of this chapter is to present the state of the art of microgrid in terms of modelling, controls and possibilities.

Recent developments in the electric utility industry and ICT are encouraging the entry of power generation and energy storage at the distribution level. Together, they are identified as DG units. Several new technologies are being developed and marketed for distributed generation. The DG includes microturbines, photovoltaic systems, wind energy systems and batteries among others.

2.1 Microgrid Definition

The MG concept assumes a cluster of loads and microsources operating as a single controllable system that provides both power and heat to its local area. This concept provides a new paradigm for defining the operation of distributed generation. The microgrid study architecture consists of a group of radial feeders, which could be part of a distribution system. There is a single point of connection to the utility called point of common coupling (PCC). The feeders have sensitive loads which should be supplied during the events. The feeders can also have the presence of microsources consisting of photovoltaic units (PV), wind turbines (WT), a microturbines (MT), battery storage and others equipment.

To serve the load demand, electrical power can be produced either directly by PV, WT or by MT.

Each component of the microgrid system is separately modelled according to its characteristics and constraints. The characteristics of some equipment as wind turbines are available from the appropriate manufacturers.

Microgrid technologies are playing an increasingly important role in the world's energy portfolio. They can be used to meet baseload power, peaking power, backup power, remote power, power quality, and cooling and heating needs. Customers usually own small-scale, on-site power generators, but they may be owned and operated by a third party.

If the distributed generators do not provide 100% of the customer's energy needs at all times, it can be used in conjunction with a distributed energy storage device or a connection with the local grid for backup power. The microgrid resources support and strengthen the central-station model of electricity generation, transmission, and distribution [1].

2.2 Reasons for Microgrids

The conventional arrangement of a modern large power system offers a number of advantages. Large generating units can be made efficient and operated with only a relatively small number of personnel. The interconnected high voltage transmission

[1] This Chapter is from "F. Katiraei, R. Iravani, N. Hatziargyriou, and A. Dimeas, "Microgrids Management – controls and operation aspects of microgrids," *IEEE Power and Energy Magazine*, vol. 6, no. 3, 2008."

network allows the generator reserve requirement to be minimized, the most efficient generating plants to be dispatched at any time, and bulk power to be transported through large distances with limited electrical losses.

The distribution network can be designed for unidirectional flows of power and sized to accommodate customer loads only. However, over the last few years several influences have combined to lead to the increased interest in microgrid schemes.

The policy drivers encouraging microgrids are [1]:

- Reduction in gaseous emissions (mainly CO_2).
- Energy efficiency or rational use of energy.
- Deregulation or competition policy.
- Diversification of energy sources.
- National and global power requirements.

2.3 Motivation of Microgrids

Currently a lot of research is being undertaken into microgrids. Although components of the microgrids are fairly well understood, the system as a whole is not. When several sources are connected to form a microgrid, the system behavior is unpredictable. This being the case, modelling the system and simulating it, in order to develop an appropriate management system, is the heart of microgrid research. Nowadays, several research groups around the world are investigating the feasibility and benefits that the microgrids may provide [2]. Some problems are encountered including dealing with the unbalanced loads and harmonics associated with the system. This work does not intend to address such problems, rather it is concerned with the modelling of the microgrid for management.

Modelling is an important component for power system energy management system. A precise model helps the electric utility to make unit commitment decisions and to reduce operating costs and emission level properly.

Besides playing a key role in meeting the load demand, it is also essential to the reliability of the microgrid.

2.4 Importance of Microgrids

The environmental and economic benefits of the microgrid, and its acceptability and degree of proliferation in the utility power industry, are primarily determined by the envisioned controller capabilities and the consequently operational features.

Depending on the type and depth of penetration of DER units, load characteristics, power quality constraints and market participation strategies, the required control and operational strategies of a microgrid can be significantly, and even conceptually, different from those of the conventional power systems.

The main reasons are the following [3]:

- steady-state and dynamic characteristics of DER units, particularly electronically coupled units, are different than those of the conventional large turbine-generator units;

- a microgrid is inherently subject to a significant degree of imbalance due to the presence of single-phase loads and/or DER;
- a noticeable portion of supply within a microgrid can be from "not controllable" sources;
- short and long-term energy storage units can play a major role in control and operation of a microgrid;
- economics often dictates that a microgrid must readily accommodate connection and disconnection of DER units and loads while maintaining its operation;
- a microgrid may be required to provide pre-specified power quality levels or preferential services to some loads;
- in addition to electrical energy, a microgrid is often responsible for generating and supplying heat to all or parts of its loads.

The following pages provide an overview of the existing microgrid controls and highlight the importance of power and energy management strategies and describe potential approaches for market participation.

2.5 Structure and Characteristics in Microgrids

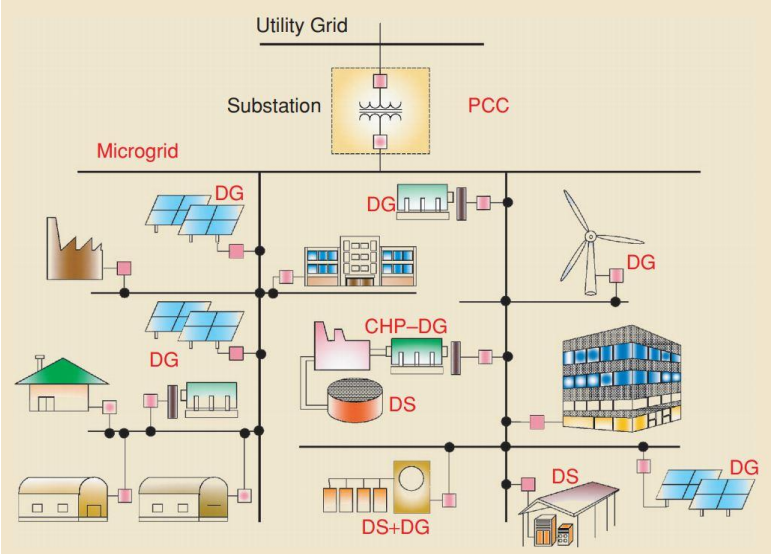

Fig. 1 A typical microgrid structure including loads and DER units

Fig. 1 shows a microgrid schematic diagram. The microgrid encompasses a portion of an electric power distribution system that is located downstream of the distribution substation, and it includes a variety of DER units and different types of end users of electricity and/or heat. DER units include both DG and distributed storage (DS) units with different capacities and characteristics.

The electrical connection point of the microgrid to the utility system, at the low-voltage bus of the substation transformer, constitutes the microgrid PCC. The microgrid serves a variety of customers, e.g., residential buildings, commercial entities, and industrial parks.

The microgrid in Fig. 1 normally operates in a grid-connected mode through the substation transformer. However, it is also expected to provide sufficient generation capacity, controls, and operational strategies to supply at least a portion of the load after being disconnected from the distribution system at the PCC and remain operational as an autonomous (islanded) entity.

The existing power utility practice often does not permit accidental islanding and automatic resynchronization of a microgrid, primarily due to the human and equipment safety concerns. However, the high amount of penetration of DER units potentially necessitates provisions for both islanded and grid-connected modes of operations and smooth transition between the two to enable the best utilization of the microgrid resources.

DER units, in terms of their interface with a microgrid, are divided into two groups. The first group includes conventional or rotary units that are interfaced to the microgrid through rotating machines.

The second group consists of electronically coupled units that utilize power electronic converters to provide the coupling media with the host system. The control concepts, strategies, and characteristics of power electronic converters, as the interface media for most types of DG and DS units, are significantly different than those of the conventional rotating machines. Therefore, the control strategies and dynamic behavior of a microgrid, particularly in an autonomous mode of operation, can be noticeably different than that of a conventional power system.

Furthermore, in contrast to the well-established operational strategies and controls of an interconnected power system, the types of controls and power/energy management strategies envisioned for a microgrid are mainly determined based on the adopted DER technologies, load requirements, and the expected operational scenarios. Fig. 2 shows a schematic representation of the building blocks of a micro-grid that includes load, generation/storage, electricity, and thermal grids.

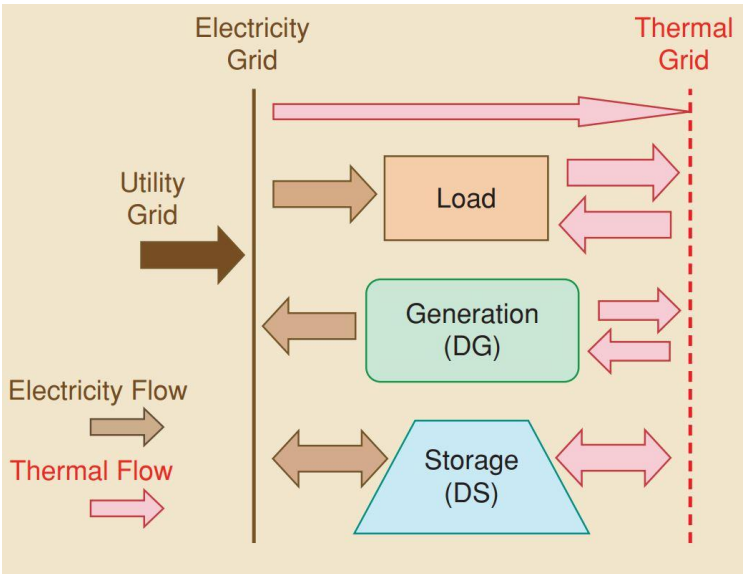

Fig. 2 general representation of the microgrid building blocks

Fig. 2 implies two levels of controls; i.e. component-level and system-level controls.

2.6 The DER Units

Both DG and DS units are usually connected at either medium or low-voltage levels to the host microgrid.

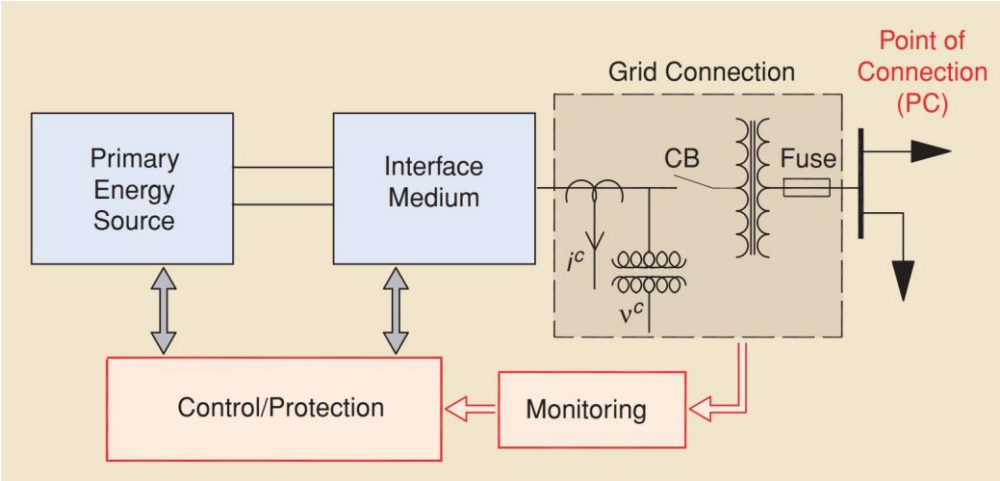

Fig. 3 Block representation of a DG unit

Fig. 3 shows a DG unit comprising a primary energy source, an interface medium, and switchgear at the unit point of connection (PC).

In a conventional DG unit the rotating machine:

- converts the power from the primary energy source to the electrical power
- acts as the interface medium between the source and the microgrid.
- For an electronically coupled DG unit, the coupling converter:
- can provide another layer of conversion and/or control; e.g. voltage and/or frequency control
- acts as the interface medium with the microgrid.

The input power to the interface converter from the source side can be AC at fixed or variable frequency or DC. The microgrid-side of the converter is at the frequency of either 50 or 60 Hz.

Fig. 3 also provides a high-level representation of a DS unit for which the “primary energy source” should be replaced by the “storage medium”.

2.7 DER Controls

Control strategies for DER units within a microgrid are selected based on the required functions and possible operational scenarios. Controls of a DER unit are also determined by the nature of its interactions with the system and other DER units. The main control functions for a DER unit are voltage and frequency control and/or active/reactive power control. Table 1 provides a general categorization of the major control functions of a DER unit and divides the strategies into the grid-following and grid-forming controls.

Each category is further divided into not-interactive and grid-interactive strategies.

Table 1 Classification of control strategies for electronically coupled DER units

	Grid-Following Controls	Grid-Forming Controls
Noninteractive Control Methods	Power export (with/without MPPT)	Voltage & frequency control
Interactive Control Methods	Power dispatch Real and Reactive power support	Load sharing (droop control)

The grid-following approach is employed when direct control of voltage and/or frequency at the PC is not required. Furthermore, if the unit output power is controlled independently of the other units or loads (not-dispatchable DER unit), it constitutes a grid-not-interactive strategy. An example of the grid-not-interactive strategy is the MPPT control of a solar-PV unit.

A grid-interactive control strategy is based on specifying real/reactive power set points as input commands. The power set points are either specified based on a power dispatch strategy or active/reactive power compensation of the load or the feeder.

2.8 Power and Energy Management

Sound operation of a microgrid with more than two DER units, especially in an autonomous mode, requires a Power Management Strategy (PMS) and an energy management strategy (EMS).

Fast response of the PMS/EMS is more critical for a microgrid compared with a conventional power system. The reasons are:

- presence of multiple, small DER units with significantly different power capacities and characteristics
- potentially no dominant source of energy generation during an autonomous mode; i.e. lack of infinite bus
- fast response of electronically coupled DER units that can adversely affect voltage/angle stability when appropriate provisions are not in place.

Fig. 4 shows information/data flow and functions of a PMS/EMS for a microgrid.

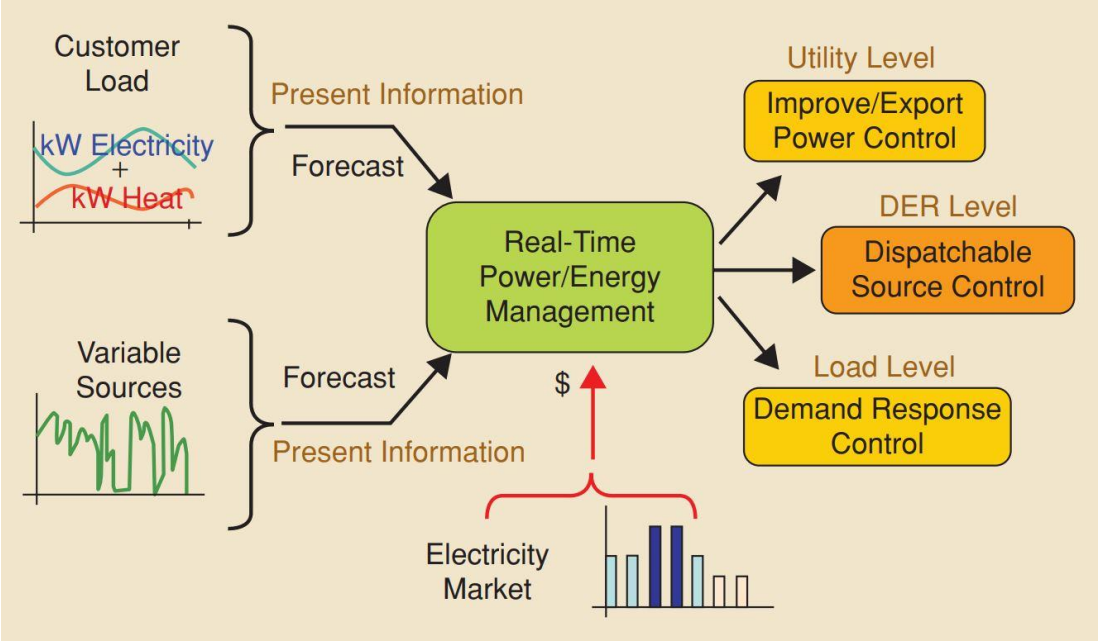

Fig. 4 Information flow and functions of a real-time PMS/EMS for a microgrid

The real-time management block receives the present and the forecasted values of load, generation, and market information to impose appropriate controls on power flow, output generation, consumption level of the utility grid, dispatchable sources, and controllable loads, respectively.

The PMS/EMS assigns real and reactive power references for the DER units to:

- appropriately share real/reactive power among the DER units
- appropriately respond to the microgrid disturbances and transients
- determine the power set points of the DER units to balance the microgrid power and restore the frequency

enable resynchronization of the microgrid with the main grid, if required.

In a grid-connected mode, the DER units supply prespecified power, e.g. to minimize power import from the e.g., islanding transients, and damp out power and frequency oscillations.

The PMS/EMS should accommodate both short-term power balancing and long-term energy management requirements.

The short-term power balancing may include:

- provisions for load-following capability, voltage regulation, and frequency control based on real power sharing among DER units and/or load shedding to alleviate power mismatch
- provisions for acceptable dynamic response, and voltage/frequency restoration during and subsequent to transients
- provisions to meet power quality constraints of sensitive loads
- provision for resynchronization subsequent to the main system restoration.

The long-term energy management may include:

- provisions to maintain an appropriate level of reserve capacity while rescheduling the operating points of dispatchable DER units based on an optimization process to
- control the net power import/export from/to the main grid,
  minimize power loss
  maximize power outputs of the renewable-based units
  minimize the cost of energy production of fuel-based units
- consideration for specific requirements/limitations of each DER unit, including type of unit, cost of generation, time dependency of the prime source, maintenance intervals, and environmental impacts
- provisions for demand response management (load-profile control) and restoration of non-sensitive loads that are disconnected/shed during the microgrid transients; for instance, in response to a load-shedding requirement subsequent to an islanding event.

3 Microgrid Modelling

The aim of this chapter is to define the modelling approach proposed by the candidate.

The present chapter aims at developing a simplified model that accounts for all the details typical of a fundamental frequency analysis. Moreover, it should be able to evaluate all the voltage and frequency transients necessary to test a primary regulation scheme

3.1 Introduction

MGs can easily integrate RES into the electric network guaranteeing an optimized management both from the economic and the environmental point of view and a higher level of power quality [4, 5]. Moreover, if a MG is capable of working in islanded configuration and to seamless transit form islanded to grid connected and vice-versa, this could generate a scenario where the power system is capable of modulate itself in accordance to the need of having a stable asset using the MG capabilities to modulate the balance between load and generation. Due to their complexity and to the variety of their sources and infrastructures, MGs also represent one of the best environments for the testing of innovative and advanced control and energy management systems. In this framework, the necessity to have a reliable model of a MG is essential in order to use it for the control system design, the tuning of its parameters and the validation of innovative energy management logics.

This goal can be reached, in one way, representing the MG in an electromagnetic power systems simulator (e.g. PSCAD-EMTDC - Power System CAD - ElectroMagnetic Transient and DC - [6], SPICE [7], PLECS [8]). The advantage of this approach is that the resulting model is extremely detailed; on the other hand, *i*) it requires a lot of time set up the model; *ii*) trained users are required and *iii*) each simulation becomes very cumbersome from a CPU point of view. It is well known that any model introduces approximations and has a domain of validity. The value of a model is represented by the trade-off between reliability, accuracy and simplicity: in particular, this last characteristic results very important to reduce the computational efforts and to give the users the possibility to handle the model easily and to have the sensitivity of the way variables interact with each other. Indeed, another possible approach is to develop a simplified model that is able to describe all the phenomena that have to be taken into account when designing a proper control system suited on the specific MG. Simplified equivalent models are very strong instruments for analysing the MG behaviour; an overview on these models is presented in [9, 10]. One of the most used approximations consists of neglecting the voltage drop along the connection (i.e. the so-called Single Bus Bar (SBB) model, according to which generators and loads are positioned at the same bus [11-13]). In other works [14-16], in order to evaluate the power flow easily, voltages are considered equal to 1 per unit so that it is possible to mismatch current with apparent power. Moreover, in [17] a simplified Ordinary Differential Equations (ODEs) system to evaluate the MG behaviour is presented, for economic purposes only.

The most relevant part of bibliography deals with the developing of MG models in the view of energy management systems accounting for longer time horizon (several

seconds, hours, days) in order to manage power sharing and the stochastic behaviour of loads and renewables [18-21]. The literature is much reduced if one considers islanded microgrids and especially those characterized by no synchronous generators connect directly to the main AC system. In this configuration, the issue of frequency and voltage control and load sharing is trickier and cannot rely on the scheme adopted for the traditional regulation. For this reason, a simplified way of representing the dynamic behaviour of a MG characterized by only power electronic interfaced generation would represent a useful tool to study and test innovative control strategies for islanded MGs.

As will be clarified later in the text, contrarily to the SBB approximation, the methodology proposed in this chapter does not neglect voltage deviations and/or power losses [13-17, 22] and allows to perform a complete analysis of the evolution of all the electric variables. The proposed approach results in a system of ODE that can be implemented in any general purpose software, giving the possibility to interface it with both traditional MG control systems [23-26] and more advanced ones [27-29] and allowing to account both for islanded and grid-connected configurations. In other words, the challenge of the proposed model, from here on Simplified Model (SM), which represents an optimal trade-off between accuracy and simplicity, is that it can be used as a universal general MG emulator, just like a base brick compatible with many lids, representing the control logics (Fig. 5). These lids can be elementary, as droop [24], isochronous [30] and current sharing [31], but also based on complex and advanced optimization and control algorithms (e.g. Model Predictive Control (MPC) [32-34], Feedback linearization (FBL) [35]). In conclusion, the advantages of the proposed model can be summarized as follows:

- Provide a simple but reliable model for islanded MGs characterized by all the generation interfaced to the AC part of the MG by means of power electronic devices;
- Running the model does not require a dedicated often licensed specific software, a relevant time to set-up the model and a high computational effort;
- The model is presented as a system of ODE that does not need too many input parameters and can be used to design different controllers and tune their parameters.

The proposed model has been validated comparing its results with the ones provided by PSCAD-EMTDC model, from here on PSCAD model, and on the Smart Polygeneration Microgrid (SPM) of the Savona Campus of Genoa University [36], highlighting a very good agreement between the two simulators and actual measurement.

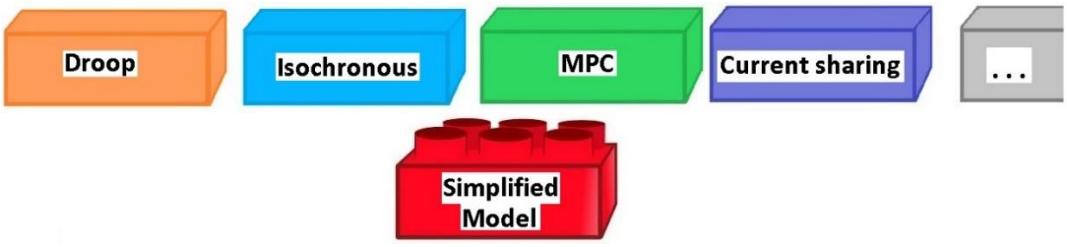

Fig. 5 Graphical representation of the proposed concept of defining a simplified model that can be used with various control strategies

3.2 The Microgrid test facility - The Savona Campus Smart Polygeneration Microgrid

The SPM is a tri-generative, Low Voltage (LV) MG realized in the Savona Campus of Genoa University in operation since February 2014. The SPM is an infrastructure realized for demonstrative and research purposes and is intended as a test-bed facility for innovative solutions for MG management and control. In order to achieve this goal, the SPM accounts for various types of generations (tri-generative micro-turbine, photovoltaic and CSP units), storage devices, electric vehicle charging stations, thermal production units and the campus as electric and thermal load. The SPM project represents nowadays an important research area for the validation of new algorithms, logics and management strategies to provide and improve innovative solutions to the problem of the integration of DERs and energy storages, fundamental requirements, for example, to the European 20-20-20 calls (Horizon 2020 Programme for Research) [37]. In 2017, a portion of SPM is being tested in an islanded configuration and analysed in terms of stability and load sharing. Such portion is represented in Fig. 7 and consists of:

- The public grid connected to switchgear (SG) Q1;
- N.1 Sodium-Nickel ST unit manufactured by FIAMM and characterized by 141 kWh energy capacity and 62 kVA rated power connected to bus Q2 (Fig. 6a);
- N.3 aggregated PV power plants each characterized by 5 kWp rated power (for a total of 15 kWp) connected to bus Q1 by means of a LV cable, from now on PV1 (Fig. 6b);
- N.1 77 kWp PV plant connected to bus Q2, from now on PV2 (Fig. 6c);
- An adjustable resistive symmetric load connected to bus Q2, rated power of 10kW. This load is used to simulate load variations in a controllable way (see Fig. 6d).

Fig. 6. a) FIAMM storage; b) PV1 generating unit; c) PV2 generating unit; d) adjustable load

Moreover, both PV2 and the storage have a transformer, whose rated values are 80kVA, 6%, 200/400 V and 70 kVA, 4%, 400/400 V respectively.

The sources ratings and the main data of the network components are reported in Table 2.

Table 2 Sources data.

	PV 1	PV 2	Storage	Load
Rated Power	3x5 kWp	77 kWp	62 kW	
Cable resistance to Q2	157.2 mΩ	20.8 mΩ	43.5 mΩ	181 mΩ
Cable inductance to Q2	3023.7 μH	14.15 μH	12.42 μH	14.59 μH

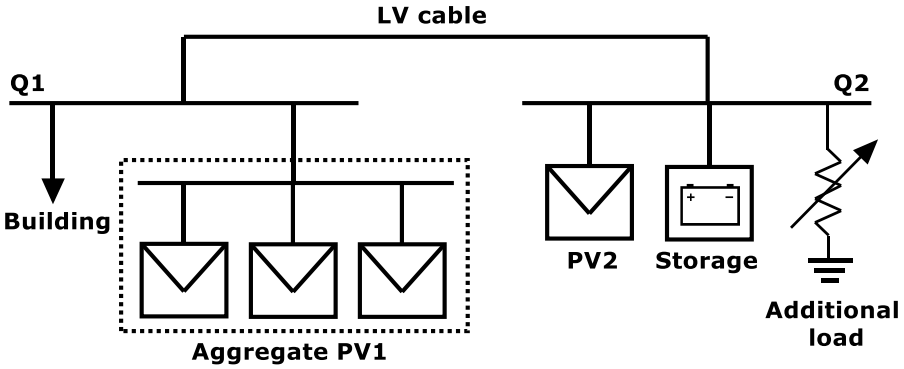

Fig. 7 SPM portion used to create the island

3.3 MG Sources and main Elements

In the present section, a mathematical modelling of the SPM components involved in the islanded portion is presented.

3.3.1 PV units model

The PV modules are modelled as a DC dipoles whose voltage-current characteristic curve (dependent on the irradiance α in W/m^2, the temperature T in °C and the V voltage expressed in V) in the I-V plane is described as follows [38]:

$$I(\alpha,T,V)=\frac{\alpha}{1000}I_{SC}\tau_i(T)\left[\frac{1-e^{\frac{V}{b\left(1+\frac{V_{MAX}-V_{MIN}}{V_{MAX}}\cdot\frac{\alpha-\alpha_{MAX}}{\alpha_{MAX}-\alpha_{MIN}}\right)\cdot(V_{MAX}+\tau_V(T))}-\frac{1}{b}}}{1-e^{-\frac{1}{b}}}\right] \quad (1)$$

where the meaning of symbols and their values are reported in in Table 3. The number p of parallel modules and s of series modules is: p=3 and s=22 for PV1 and p=14 and s=24 for PV2.

Table 3. PV Module parameters

PV Module parameters		
Short circuit current in Standard Test Conditions (STC)	I_{SC}	8.75 A
Rated external temperature	T_N	25°C
Temperature coeff. of the short circuit current	T_{CI}	0.06
Temperature coeff. of the open module voltage	T_{CV}	-0.31

Minimum solar radiation to supply energy	α_{MIN}	0.2 kW/m^2
Maximum solar radiation to supply energy	α_{MAX}	1 kW/m^2
Open voltage module at α_{MIN}	V_{MIN}	35 V
Open voltage module at α_{MAX}	V_{MAX}	37.11 V
Maximum power point voltage in STC	V_{MPP}	29.7 V
Maximum power in STC	P_{MPP}	240 W
Model fit parameter	b	0.0777

3.3.2 Electric storage model

The electric storage system is a FIAMM SoNick battery (Zebra), with rated capacity of 141 kWh, 228 Ah of nominal current capacity (NCC), rated power of 62 kW when suppling and 30 kW when absorbing. It is structured in N_m=6 modules in parallel each one composed by the series of N_c=240 cells [39]. The storage is represented by a non-ideal DC voltage generator, where the produced voltage V is a function of its state of charge (SOC) [40], its internal resistance R_{int} and the current I injected by the storage, according to the following equation:

$$V \equiv V\left(SOC, I\right) = E\left(SOC\right) - IR_{int} \tag{2}$$

where the internal voltage (E) is an unknown function of the SOC, to be deduced from measured data. The model proposed in (2) is justified observing Fig. 8, where it can be noticed that discharging the battery at different (constant) currents results in a rigid translation of the curve. Under this assumption, for a fixed value of the SOC, the voltage V depends proportionally on the current. In terms of electric equivalent, if there is a linear relationship between voltage and current, there is an internal resistance, whose value can be estimated by simply knowing two voltage-current couples.

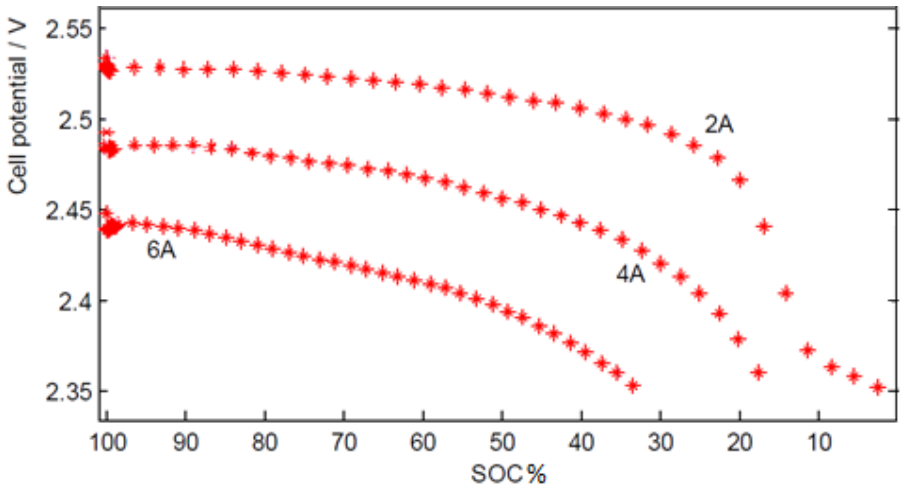

Fig. 8 V/SOC cell characteristic [40]

For each current I, a set of N measurements is available in Fig. 8, formally encoded in the following

$$\left\{\left(SOC_k, V_{k,\mathrm{I}_p}\right): k=1,\ldots,N \text{ and } p=1,\ldots,N_i\right\} \tag{3}$$

where, for our measurements, N_I=3 and I_1=2A, I_2=4A and I_3=6A. The cell resistance value can be calculated as the following average

$$R_{cell} = \frac{1}{N_I N}\sum_{k=1}^{N}\left[\sum_{\substack{p,q=1 \\ I_q>I_p}}^{N_I}\left(\frac{V_{k,I_p}-V_{k,I_q}}{I_q-I_p}\right)\right] \tag{4}$$

that allows to obtain that R_{cell}=0.028 Ω. As a consequence, the pairs (SOC_k, $E_{cell,k}$) can be obtained as follows:

$$E_{cell,k} = V_{k,\mathrm{I}_1} + R_{cell}\cdot I_1 \tag{5}$$

Finally the possible analytical expression for the link between the internal voltage and the SOC can be obtained fitting the pairs (SOC_k, $E_{cell,k}$) with the following polynomial formula:

$$E_{cell} = \sum_{i=0}^{6} a_i \cdot SOC^i \tag{6}$$

where the coefficients a_i have been found with a least square method aimed at minimizing the difference between the polynomial output and the measured sequence $E_{cell,k}$. The numerical values of the coefficients are reported in Table 4 and the resulting curve is depicted in Fig. 9.

Table 4 Polynomial coefficients

[A]	a_6	a_5	a_4	a_3	a_2	a_1	a_0
0 [A]	1.6 10^{-11}	-4. 10^{-9}	6. 10^{-7}	-3.3 10^{-5}	7.5 10^{-4}	5.2 10^{-4}	2.42

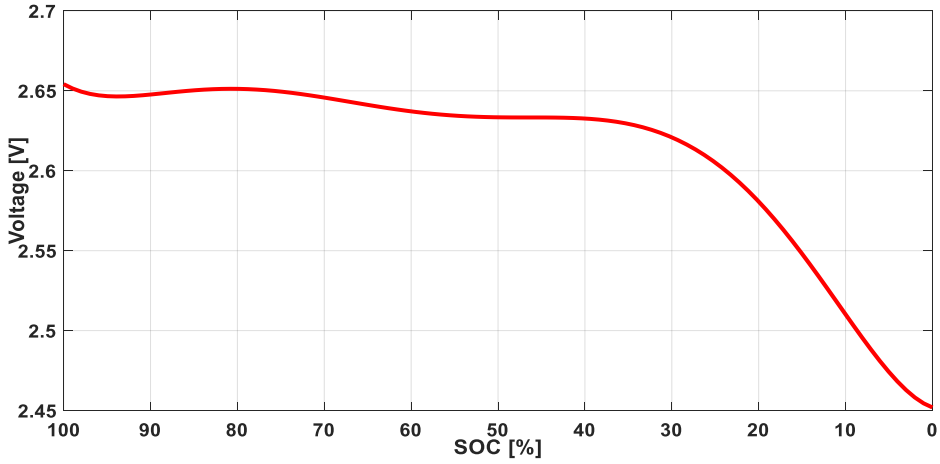

Fig. 9 Voltage against SOC cell characteristic

Then, the maximum voltage of a single cell results:

$$E_{cell}\left(SOC=100\%\right)=2.66\ \mathrm{V} \tag{7}$$

therefore, the maximum voltage of the overall storage is

$$E\left(SOC=100\%\right)=E_{cell}\left(SOC=100\%\right)\cdot N_c=2.66\text{V}\cdot 240=640\text{ V} \tag{8}$$

and the internal resistance is

$$R_{int}=\frac{R_{cell}\cdot N_c}{N_m}=\frac{R_{cell}\cdot 240}{6}=1.12\ \Omega \tag{9}$$

The dependence of the voltage from the temperature is neglected according to Zebra features [41]. Often, and thus also in this MG, between the storage and its inverter, a DC/DC bidirectional converter is interposed (that will be discussed in detailed in the following).

3.3.3 Inverter model

The aim of the inverter is to couple the DC sources to the AC grid correctly. Each inverter is modelled by the mean-values input/output relation, thus

$$\dot{V}_{AC}=\frac{mV_{DC}e^{j\delta}}{2\sqrt{2}} \tag{10}$$

where $\dot{V}_{AC}$ is voltage phasor, m is the modulation index, V_{DC} is the voltage at DC terminals, j as usual is the imaginary unit, and δ is the angle of the phasor.

Each inverter presents a filter posed at its AC terminals in order to attenuate high frequencies harmonics and a capacitor of 2.5 μF at the DC terminals in order to stabilize the voltage. Fig. 10 and Table 5 present the configuration and the parameters of the filter.

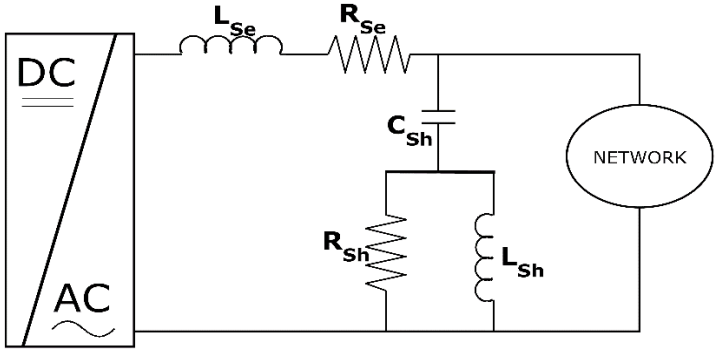

Fig. 10 Inverter AC filter configuration

Table 5. AC filter parameters

L_{se}	R_{se}	L_{sh}	C_{sh}	R_{sh}
1 [mH]	0.314 [mΩ]	0.0166 [mH]	1 [μF]	2.61 [kΩ]

3.3.4 DC/DC Converter Model

In order to allow a proper operation of the inverter it is necessary to keep its DC voltage as much constant as possible. Thanks to the MPPT algorithm, PV inverters are controlled in a way that keep the DC voltage almost constant, since the MPP voltage do not vary so much [42]. The storage inverters, on the other hand, are characterized by a sensible variation of the voltage on the battery, thus they need a dedicated control

of the voltage obtained by the insertion of a DC/DC bi-directional (buck-boost) chopper. The DC/DC converter has the structure depicted in Fig. 11 [43].

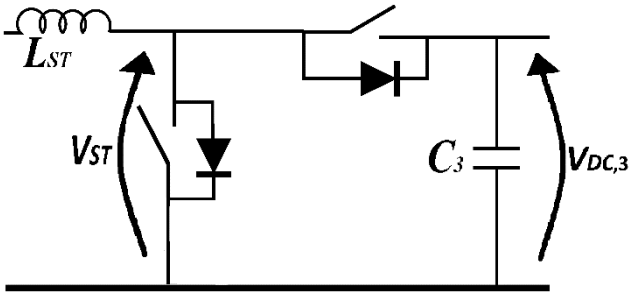

Fig. 11 DC/DC converter circuital layout

The well-known chopper input/output relationship [43] is given by:

$$V_{DC,3} = K_{ST} V_{ST} \tag{11}$$

being $V_{DC,3}$ and V_{ST} the DC/DC output (inverter side) and input (battery side) voltages respectively, while K_{ST} is related to the switch duty cycles D_1 (boost) and D_2 (buck) according to the following:

$$K_{ST} = \begin{cases} \dfrac{1}{1-D_1} & P_{ST} \geq 0 \\ \dfrac{1}{D_2} & P_{ST} < 0 \end{cases} \tag{12}$$

being P_{ST} the power injected by the storage into the network. Moreover, a filter consisting of a series inductor and a shunt capacitor have been inserted, whose values are 1 mH and 0.5 mF respectively.

3.4 The Proposal

The aim of this subsection is to propose an approximate model able to adequately represent both the transient and the steady state of any MG, after any contingency.

The final goal is to define a simple but effective model for no-inertia islanded MGs expressed in terms of a system of Ordinary Differential Equations (ODEs) capable of capturing all the dynamics of the involved electric quantities with a reduced set of input parameters. The proposed model keeps the system non-linearity and assumes the control input of the MG converters as its own inputs in order to be interfaced with any proposed control strategy. Moreover, it does not need any specific licensed software to be implemented and requires a limited CPU effort to run.

To do this, the following simplifications are introduced:

- Each input/output power electronics converter relationship neglects the presence of the higher order harmonics
- The shunt sections of inverters AC filters are neglected for simplicity (indeed it can be noted from Table 5 that the shunt filter impedance at fundamental frequency is more than 3 kΩ). If one considered it, this would imply only an enlargement of the network admittance matrix Y without changing the model structure.

- The AC-side portion of the MG (the inverter filter too) is supposed to be at steady state (assuming that both the angular frequency of the sources and their voltage amplitude can vary), while all the DC dynamics are accounted
- The loads are described with a constant impedance model. Consequently, as typical in RMS transients they are inserted in the network model, giving origin to the so called extended admittance matrix Y_E [44].

Let us assume that the MG is composed by N power generating units and N_L load buses and let us use the index k to represent the generic *k-th* inverter. The overall schematic representation of the off-grid MG considered for the SM is depicted in Fig. 12.

Thus, in the case of the SPM, the portion described in Fig. 7 collapses in the one shown in Fig. 12.As will be clear writing the equations, it is apparent that the description of the AC grid with the extended admittance matrix allows to couple in a simple but effective way the sources dynamics.

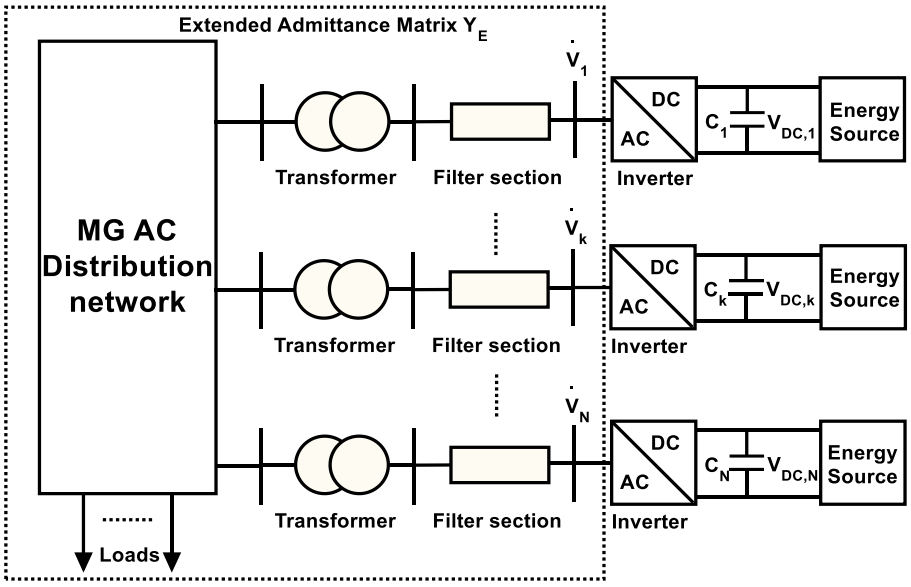

Fig. 12 Simplified model of the islanded portion of the SPM

The first assumption allows to write that [43]:

$$\dot{V}_k(t) = \frac{m_k(t)}{2\sqrt{2}} V_{DC,k}(t) e^{j\delta_k(t)} \tag{13}$$

where j, as usual, is the imaginary unit, and, for the k-th source, m_k is the modulation index (in accordance to its linear meaning [43], its lays in the range [0, 1.15]) and δ_k is the angle such that:

$$\delta_k(t) = \psi_k(t) + \varphi_k(t) \tag{14}$$

where

$$\frac{d\,\psi_k(t)}{dt} = \omega_k(t) \tag{15}$$

while ω_k and φ_k are the angular frequency and the phase of the k-th source, respectively. The main network is an independent voltage source, whose phasor is given by:

$$\dot{V}_k = V e^{j\delta_k} \tag{16}$$

Thus, the active power injected by the k-th source is given by:

$$P_{AC,k}(t) = 3\,\mathrm{Re}\left\{\dot{V}_k \dot{I}_k^*\right\} = 3\,\mathrm{Re}\left\{\dot{V}_k \sum_{i=1}^{N}\left(\dot{Y}_{E,ki}^*\left(\dot{\mathbf{V}}_L\right)\dot{V}_i^*\right)\right\} \tag{17}$$

where $Y_{E,ki}=G_{ki}+jB_{ki}$ is the (k,i) element of the extended admittance matrix and $\left[\dot{\mathbf{V}}_L\right]=\left[\dot{V}_{L1}..\dot{V}_{LN_L}\right]^T$ being $\dot{V}_{Li}$ the *i-th* load bus voltage. As stated before, Eq. (17) shows the strong coupling of the sources through Y_E.

Indicating with $G_{ki}\left(\dot{\mathbf{V}}_L\right)$ and $B_{ki}\left(\dot{\mathbf{V}}_L\right)$ $\dot{Y}_{E,ki}\left(\dot{\mathbf{V}}_L\right)$ real and imaginary part, it is possible rewriting (17) as:

$$P_{AC,k} = 3\frac{m_k V_{DC,k}}{8}\sum_{i=1}^{N}\left\{m_i V_{DC,i}\begin{bmatrix}\cos\left(\delta_k-\delta_i\right)G_{ki}\left(\dot{\mathbf{V}}_L\right)+\\ +\sin\left(\delta_k-\delta_i\right)B_{ki}\left(\dot{\mathbf{V}}_L\right)\end{bmatrix}\right\} \tag{18}$$

Moreover, on the DC side of the inverter a capacitor C_k is connected with the aim of supporting the DC inverter voltage during power transients. The capacitor power balance can be written as:

$$C_k V_{DC,k}\frac{dV_{DC,k}}{dt} = P_{DC,k} - P_{\mathrm{AC},k} \tag{19}$$

$P_{DC,k}$ being the power injected by the *k-th* energy source at the DC link.

The generic *n-th* ST is modelled as a non-ideal DC voltage generator representing the battery units connected to the DC side of the inverter by means of an intermediate DC/DC chopper in buck-boost configuration. The DC/DC converter is needed in order to keep a constant voltage at the DC side of the converter while the buck-boost configuration allows a bi-directional power flow. Between the battery and the DC/DC converter a series inductor is considered, $L_{ST,n}$, in order to operate the DC/DC converter also in step-up configuration. The ST equivalent circuit is depicted in Fig. 13.

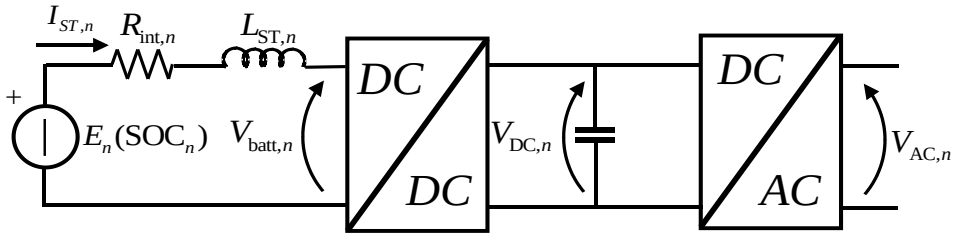

Fig. 13. Schematic circuital representation of the generic *n-th* ST unit.

The battery is represented by a Thevenin equivalent where the value of the voltage generator, namely E_n, is dependent on its state of charge (SOC_n). This dependency could be expressed by means of a 6th order polynomial in the form:

$$E_n\left(SOC_n\right) = \sum_{i=0}^{6} a_i \cdot SOC_n^{\,i} \tag{20}$$

The values of a_i coefficients vary in accordance to the specific battery technology (details on the ST modelling are available in [45]). Neglecting the dependence of the state of charge on the temperature (which is reasonable for the SPM battery technologies as specified in [45]), the DC voltage provided at the battery terminals, $V_{batt,n}$, can be then written as:

$$V_{batt,n}\left(SOC_n, I_{ST,n}\right) = E_n\left(SOC_n\right) - I_{ST,n}R_{int,n} \tag{21}$$

where $R_{int,n}$ is the battery internal resistance. SOC_n is related to the ST current $I_{ST,n}$ by:

$$\frac{d\,SOC_n}{dt} = -\frac{I_{ST,n}}{NCC_n} \tag{22}$$

where NCC_n is the nominal current capacity of the *n-th* ST.

Furthermore, the ST device current dynamic equations are:

$$L_{ST,n}\frac{dI_{ST,n}}{dt} = E_n\left(SOC_n\right) - R_{\text{int},n}I_{ST,n} - \frac{V_{DC,n}}{K_{ST,n}} \tag{23}$$

where $K_{ST,n}$ is the DC/DC converter gain. The DC/DC controller has the aim of keeping constant the ST DC link voltage [43]. For the *n-th* ST unit, one can now define the DC power to be used in (19) as:

$$P_{DC,n} = \frac{V_{DC,n}I_{ST,n}}{K_{ST,n}} \tag{24}$$

Equations (14), (15), (18) - (24) represent the system behaviour and completely describe the DC dynamics of the MG. The modelling of the network with the extended admittance matrix allows accounting for the influence of the network topology on the AC side power flows. The inputs of the proposed SM can be divided into two categories: *i*) physical inputs that depend on the specific energy source (wind speed, solar irradiance, fuel, etc.) and *ii*) control inputs that are the inverters modulation index m_k, frequency ω_k and phase φ_k. Such inputs are provided by the MG controller according to the specific control strategy. Since the scope of the work is to propose a SM of the MG power system to be interfaced with any control logic *i*) and *ii*) are going to be the boarder signals of the proposed modelling.

In conclusion, a differential equations (ODE) system can be written as:

$$\dot{\mathbf{X}} = f(\mathbf{X}, \mathbf{U}) \tag{25}$$

where f collects (15), (19), (22) and (23), while the vectors **X** and **U** are given by:

$$\begin{aligned} \mathbf{X} &= \begin{bmatrix} V_{DC,k} & I_{ST,n} & SOC_n & \psi_k \end{bmatrix}^{\mathbf{T}} \\ \mathbf{U} &= \begin{bmatrix} m_k & \omega_k & \varphi_k \end{bmatrix}^{\mathbf{T}} \end{aligned} \tag{26}$$

The initial equilibrium point can be obtained by solving the non-linear algebraic system, obtained by zeroing all the time derivatives in (25).

Starting from an assigned equilibrium point, a structure perturbation (encoded in a variation in one or more elements of the extended admittance matrix) causes the dynamics. It is useful to underline that, in order to exclude a source from the analysed

grid, it is sufficient to cancel the related admittances, highlighting the flexibility of the proposed approach to be applied at different MG structures.

In summary, a step by step synopsis could be useful to summarize the whole procedure:

- Define the MG topology, parameters (rated data of cables, transformers, sources etc.) and admittance matrix;
- Define the sources and their characteristic (power- irradiance for PV, power-wind velocity for wind generator, *V-SOC* for chemical storage etc.);
- Define the all the state variables and write the resulting ODEs;
- Define an equilibrium point of the system zeroing all the time derivatives;
- Define a contingency;
- Solve the resulting ODE system and get the involved variables dynamics.

The proposed model differs from the well-known Dynamic Phasor modelling [46, 47] in terms of considering the relationships among AC quantities as steady-state ones. On the other hand, DC dynamics are considered, so that any DC inductor or capacitor gives origin to one differential equation. AC variations are consequent to the variation of the DC quantities by means of the interfacing converters.

3.5 The PSCAD Model

Beside the validation on the SPM experimental test bed, the proposed SM has also been compared against an implementation of the islanded portion of the SPM on PSCAD-EMTDC, a commercial software for electromagnetic simulation. This comparison is done in order to have a simulative reference for the proposed SM accounting for a more accurate dynamic of electrical quantities. Implementation on an electromagnetic simulator allows accounting for higher order dynamics of the system in order to evaluate the impact of the SM hypotheses on the final result.

The main differences between the PSCAD model and the proposed SM are: *i*) all electronic devices (DC/DC and DC/AC) consist of controlled not ideal IGBT with PWM modulation and *ii*) each inverter has an AC filter composed with a series and a shunt section in order to suppress the PWM harmonics, as depicted in Fig. 14.

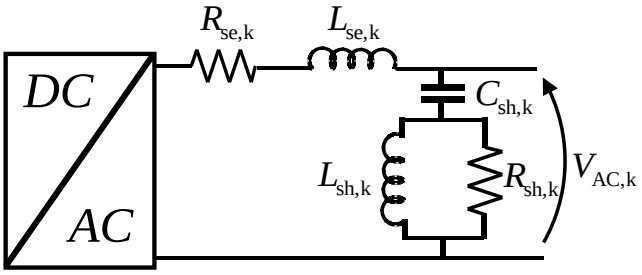

Fig. 14. Inverter AC filter implemented in PSCAD

Under these assumptions, the whole harmonic spectrum is accounted both on the DC and AC side in the PSCAD environment. As far as the PV systems and the ST unit are concerned, they have been implemented by the authors as a DC bipole connected to

the DC side of the corresponding converter section. The PV one accounts for (1) while the ST one includes (20), (21) and (22).

3.6 Test Case Definition

Before starting with the experimental validation of the proposed SM, it is necessary to characterize all the parameters needed to set up the SM in a suitable environment. For the following simulations the SM has been implemented in MATLAB. With reference to the SM general formulation of Section II, for the specific case of the islanded portion of the SPM N is equal to three, N_{ST} is one and N_{PV} is equal to two. Using the same structure depicted in Fig. 12, it is possible to include in the extended admittance matrix all the loads and the elements of the AC side of each power generating unit. Fig. 15 depicts the considered system one-line diagram.

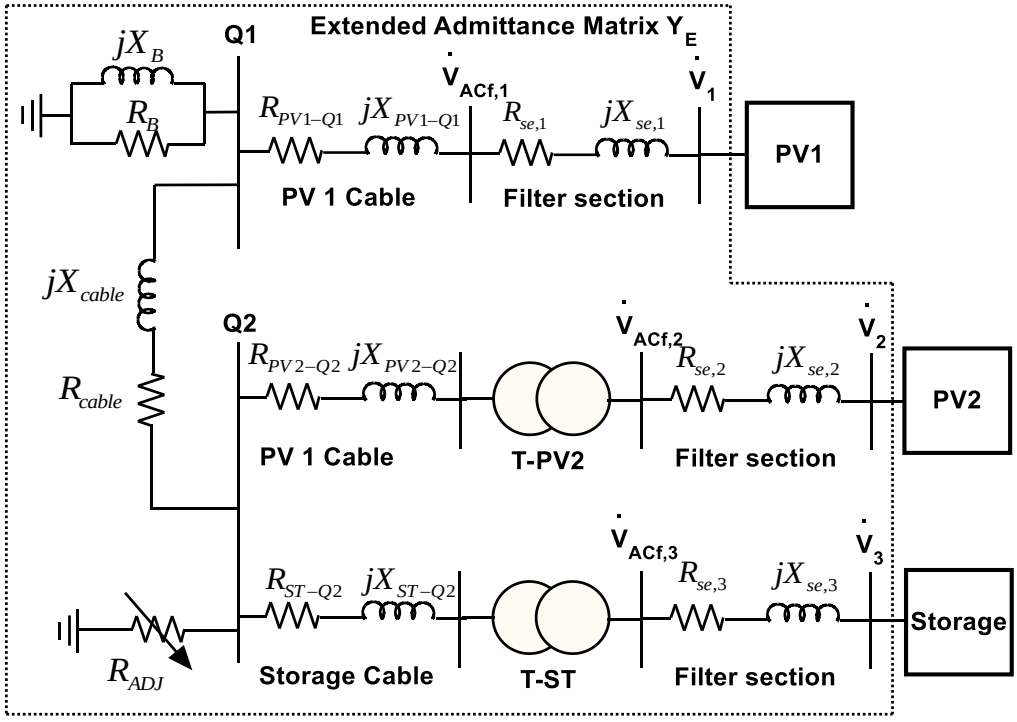

Fig. 15. SPM islanded section one-line diagram.

As one can see, both PV2 and the ST system are equipped with a dedicated transformer and a cable connection is present for every generating unit to connect busses Q1 and Q2. In the proposed implementation, cables are modelled by means of a simple resistive-inductive series impedance, suitable at the light of the reduced length of the cables, and transformers are represented with the only leakage reactance. All the parameters of the test bed AC network are reported in Table 6.

Table 6 Test bed facility AC section parameters

$R_{se,1}$	0.314mΩ	$R_{PV2\text{-}Q2}$	0.0208 Ω
$X_{se,1}$	0.314 Ω	$X_{PV2\text{-}Q2}$	0.0044 Ω
$R_{PV1\text{-}Q1}$	0.057 Ω	$R_{se,3}$	0.314 mΩ
$X_{PV1\text{-}Q1}$	1.027 Ω	$X_{se,3}$	0.314 Ω
$R_{se,2}$	0.314 mΩ	$X_{T\text{-}ST}$	0.0088 Ω

$X_{se,2}$	0.314 Ω	$R_{ST\text{-}Q2}$	0.0435 Ω
$X_{T\text{-}PV2}$	0.137 Ω	$X_{ST\text{-}Q2}$	0.0039 Ω

The PV parameters necessary to implement (1) are the same for the two PV plants and are detailed in Table 3.

Finally, attention must be paid to the load characterization, especially to the building one. As stated in §3.4, in the SM, the load is represented by an algebraic voltage/current law. Since the building load is characterized by a stochastic behaviour, the first problem to be faced is to find out a possible closed-form law that fits with the real behaviour. As a first comment, no motors or large under converter loads are present in the building, since it only hosts classes and offices (heating and cooling are provided by a central station which is not electrically connected to the islanded SPM). This suggests the possibility of considering a linear law (i.e. to suppose that the building load can be represented by a resistance and a reactance posed in parallel). Of course, a specific validation of this assumption is not possible, but the agreement between simulation results and measurements will give a justification of this choice. In order to calculate the suitable value of the building equivalent resistance and reactance, the following procedure has been derived. If one neglects distribution losses, the active and reactive power absorbed by the building load (P_{LOAD} and Q_{LOAD}) can be estimated from the active and reactive power delivered at the ST AC terminals, $P_{AC,3}$ and $Q_{AC,3}$ in addition to the active and reactive power injected by each PV unit, $P_{AC,2(1)}$ and $Q_{AC,2(1)}$:

$$\begin{cases} P_{LOAD} = P_{AC,1} + P_{AC,2} + P_{AC,3} \\ Q_{LOAD} = Q_{AC,1} + Q_{AC,2} + Q_{AC,3} \end{cases} \tag{27}$$

Assuming that the system voltage drop is negligible, due to the limited length of all connecting cables, the voltage at bus 2 can be assumed equal to the ST one ($V_{AC,3}$). It is then possible to calculate the equivalent building load phase resistance and reactance R_B and X_B as:

$$R_B = \frac{3V_{AC,3}^2}{P_{LOAD}} \qquad X_B = \frac{3V_{AC,3}^2}{Q_{LOAD}} \tag{28}$$

In the considered case, the numerical values of the equivalent building load phase resistance (R_B) and reactance (X_B) are 13.2 Ω and 33 Ω respectively (corresponding to an active and reactive power absorption of about 12 kW and 4.8 kVAr). In addition to the parameter list up to here, the PSCAD model needs a wider set of data, since it also includes the shunt section of the inverter AC filters; those are listen in Table 7 (identical for the three units).

Table 7 PSCAD additional parameters

$R_{sh,1}=R_{sh,2}=R_{sh,3}$	$L_{sh,1}=L_{sh,2}=L_{sh,3}$	$C_{sh,1}=C_{sh,2}=C_{sh,3}$
2.615 kΩ	0.0166 mH	1 μF

As pointed out in §3.4, the specific control logic is out of the scope of the present article; nevertheless, in order to compare the results obtained by the experimental validation and the simulation ones, the islanded SPM control strategy needs to be implemented in both the models. The islanded SPM accounts for a master/slave control where the ST is the master unit providing the frequency reference to the system and regulating its terminal voltage. The slave units, PV1 and PV2, are regulated based on an active and reactive power independent reference and they are locked to the measured system frequency. Consequently, the master unit guarantees the electric power balance. The PVs active power reference is provided by a minimum logic selection between the signal of the MPP and the eventual active power external limitation. As outputs, the master/slave control logic provides the frequency and modulation index for the master unit and the modulation index and the phase shift for the slave ones.

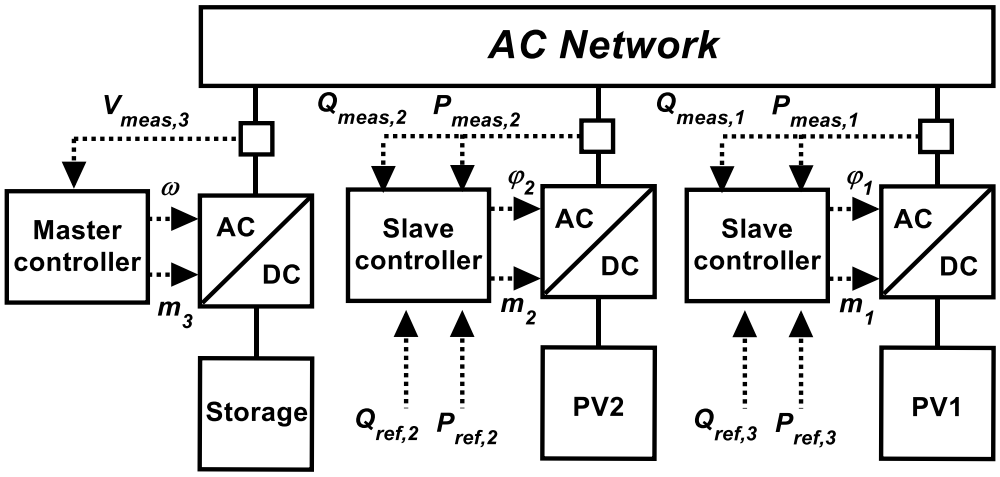

Fig. 16. SPM island control logic

The master/slave control logic of the islanded portion of the SPM is sketched in Fig. 16. This philosophy has been implemented in both models in order to achieve consistent results. The Master controller aims at keeping the ST AC voltage after the filtering section $V_{ACf,3}$ at its rated value acting on the modulation index m_3 by means of a Proportional Integral (PI) controller, as depicted in Fig. 17 while the modulation function phase is fixed at zero. The master controller also imposes the system frequency ω.

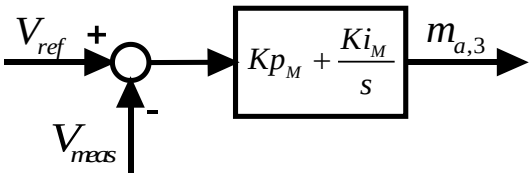

Fig. 17. Master unit control scheme

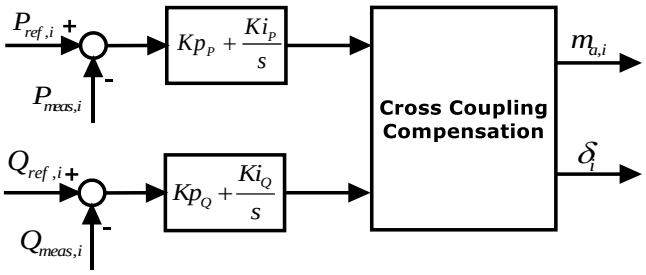

Fig. 18. Slave unit control scheme

The slave controllers provide active and reactive power control in accordance to specific reference signals (e.g. for the PV systems the MPP signal and the reactive power external reference). The controller accounts for two PI controllers and a cross coupling compensation as depicted in Fig. 18 for the generic *i-th* slave unit (see [48] for details).

3.7 Experimental Validation

The aim of this section is to provide a validation of the proposed MG model. As previously highlighted, the validation has been performed comparing the results obtained by the proposed SM with the ones of a detailed time domain simulation implemented in PSCAD environment and against on-field measurement acquired at the University of Genoa SPM test bed facility. To achieve the target of acquiring a complete set of meaningful data, two different measurement instruments were used, both posed downstream of the ST inverter and transformer. The first one is a Jupiter Power Quality Analyser [49] (Fig. 19a), while the second is a Fluke 190-104 ScopeMeter [50] (Fig. 19b). The Jupiter Power Quality is used to acquire the measurement of the values of current, voltage and power on a wider horizon due to its capability to sample one value per second. The Fluke 190-104 ScopeMeter, on the other hand, can show voltages and currents waveforms in a precise way and was used to record phase currents and voltages waveforms in a narrow temporal window thanks to its 16 μs sampling time.

Fig. 19 a) Jupiter Power Quality Analyser; b) Fluke 190-104 ScopeMeter

The comparison is made considering the ST active power, the AC line to ground voltage and the AC phase current. However, since the Jupiter Power Quality Analyzer sampling time is in the order of one point per second, it is not capable of providing a suitable measurement for an accurate comparison. For this reason, active and reactive power have been calculated on the basis of the ST current and voltage waveforms recorded by the Fluke oscilloscope applying the well-known instantaneous power theory in the Park domain [48]. The comparison is performed accounting for three different scenarios representative of possible occurrences in the MG operation, corresponding to a load variation (Scenario A), a reactive power reference variation (Scenario B) and a PV unit disconnection (Scenario C). For the three scenarios, PV units were limited in power production in order to avoid errors introduced by possible power variation due to unpredicted irradiance changes during the measurement period. The SPM initial operational condition is summarized in Table 8.

Table 8 Initial MG steady-state condition

Component	Active power	Reactive power
PV1	9 kW	0 kVAr
PV2	20 kW	0 kVAr
ST	-16.8 kW	5.0 kVA
Load	about 12 kW	about 4.8 kVAr
Resistor load	0 kW	0 kVAr

3.7.1 Scenario A – Load variation

The first test case scenario aims at highlighting the performances of the SM after a load variation. The load variation is simulated in a deterministic way inserting the additional resistor bank after 1 s from the beginning of the data acquisition with an equivalent power request increase equal to 10 kW. As one can see from Fig. 20, the ST active power absorption decreases and this is confirmed by the reduction of its AC current (see first sub-plot of Fig. 21), where the current peak passes from about 35 A to 20 A. in particular, the active power variation recorded at the ST terminals is 10.4 kW, showing that this component satisfies the load increased demand together with losses compensation. The AC ST voltage (second sub-plot of Fig. 21) does not suffer the load variation keeping mainly constant its peak value. All the figures exhibit a good agreement among the curves both for steady-state and transient. The most relevant difference among the simplified and PSCAD models and the experimental results can be seen in Fig. 20, where both the models active powers reach the final steady-state before the measured one.

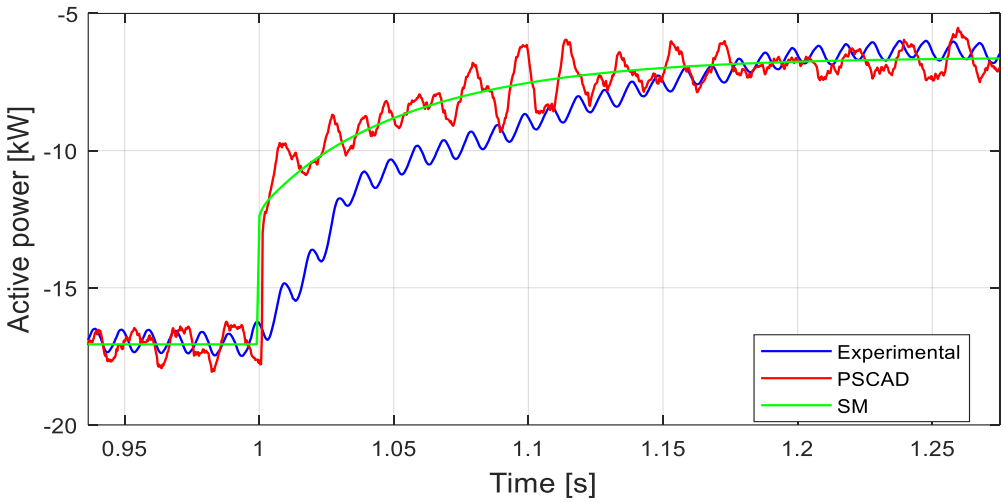

Fig. 20. Scenario A ST active power. Experimental data (blue line), PSCAD (red line) and SM (green line).

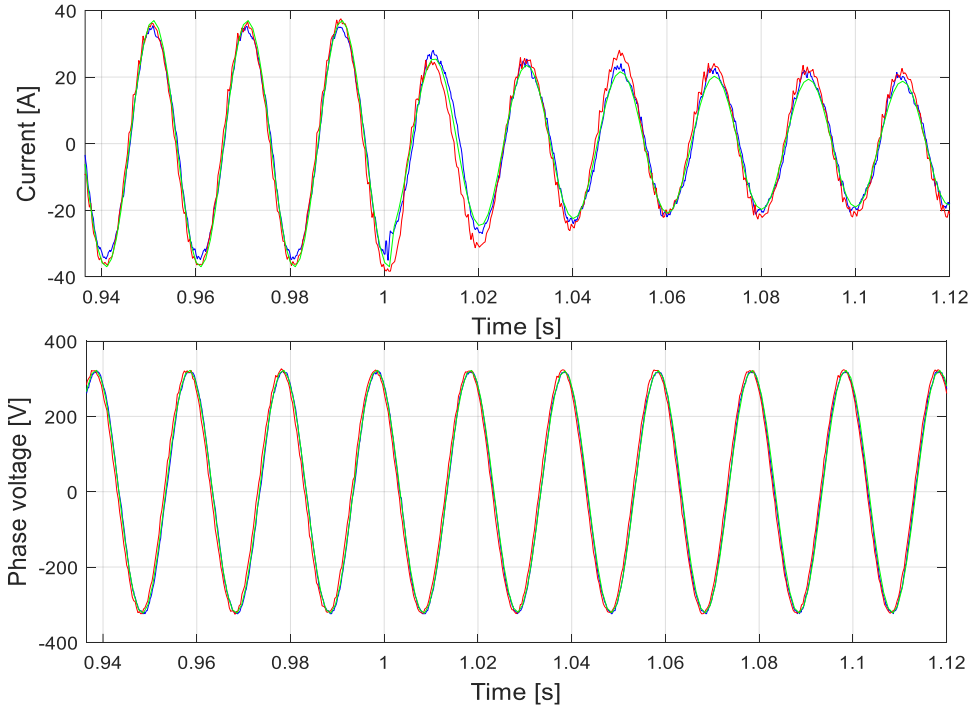

Fig. 21. Scenario A ST current and phase voltage. Experimental data (blue line), PSCAD (red line) and SM (green line).

This is because, as the inverter controller and filter details have not been shared by the manufacturer, typical topologies, parameters and control strategies have been assumed in the models in order to achieve the best possible fitting.

3.7.2 Scenario B - Reactive power variation

The second test case concerns a reactive power variation of PV2 unit. Starting from the initial condition of table 8, a step variation of the reactive power reference is provided to PV2 inverter, passing from 0 to -10 kVAr. The experimental recording of Fig. 22 (blue curve) highlights that the ST reactive power follows the step reference with a sensible delay. This is probably due to a rate limiter included in the PV internal controller, whose details have not been shared by the manufacturer. For this reason, in

order to mimic the experimental conditions for the two models, a rate limiter has been implemented in both models whose parameters have been guessed in order to reach a good fitting with experimental results. The comparison appears in in Fig. 22 highlighting an excellent agreement concerning steady-state values and some slight deviations during the transient. Finally, Fig. 23 shows the good agreement among the three curves in terms of current and phase voltage waveforms at the AC side of the inverter.

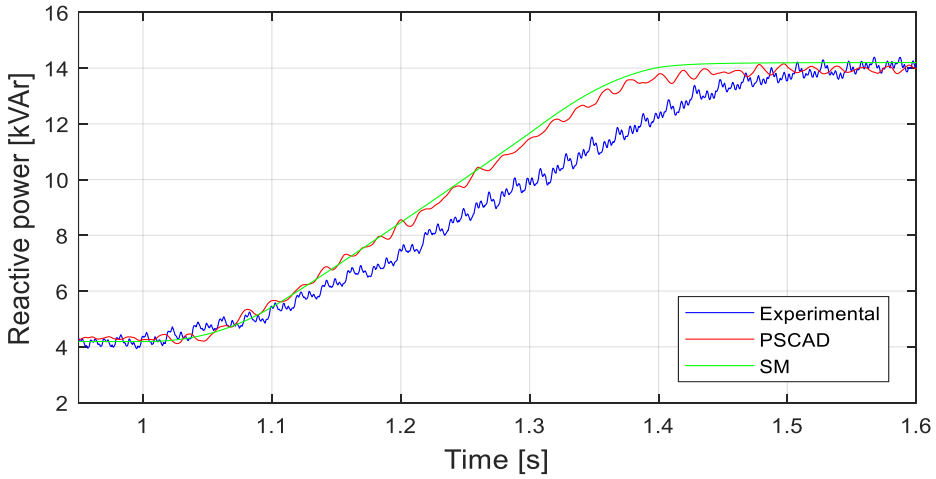

Fig. 22. Scenario B ST reactive power. Experimental data (blue line), PSCAD (red line) and SM (green line).

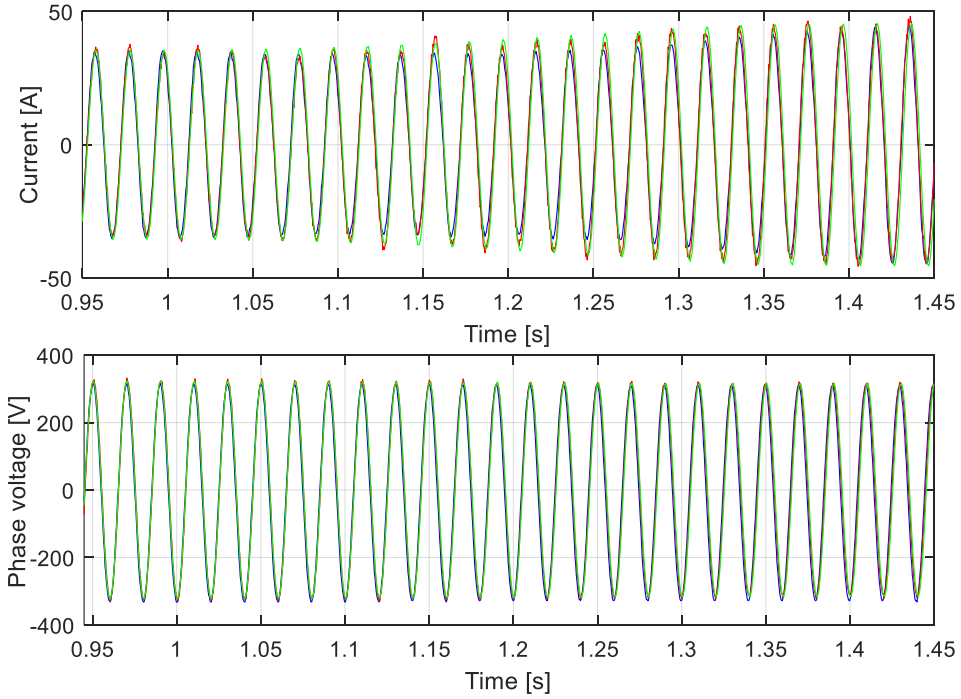

Fig. 23. Scenario B ST current and phase voltage. Experimental data (blue line), PSCAD (red line) and SM (green line).

3.7.3 Scenario C - PV2 disconnection

PV2 disconnection (after 1 s from the beginning of data acquisition) is representative of a clouding or a disconnection subsequent to a fault or an overloading of the PV system. In the SM the PV2 disconnection can be simulated zeroing the line and the

column of the admittance matrix corresponding to its bus. The initial steady-state for Scenario C is a little different from test cases A and B because the controllable resistive bank was fully inserted in the initial steady-state. This variation has been introduced to obtain a ST dynamic characterized by a power flow inversion in order to validate the model in both the ST operational conditions (power production and absorption) and during the transition between different assets. For this reason, the initial ST power production is equal to -6.8 kW. The first sub-plot of Fig. 24 describes the behaviour of the ST phase current when PV2 is detached. As one can see, the current increases its amplitude and has a phase shifting so that the active power request by the load is satisfied. Moreover, in Fig. 25 one can notice the active power inversion at the ST AC bus bar. The agreement among the two approaches is still good with some deviations with experimental data in the power sign inversion transient, partially due to the lack of information on the inverter and chopper controllers. The second sub-plot of Fig. 24 describes the voltage behaviour, which is again not affected by the contingency.

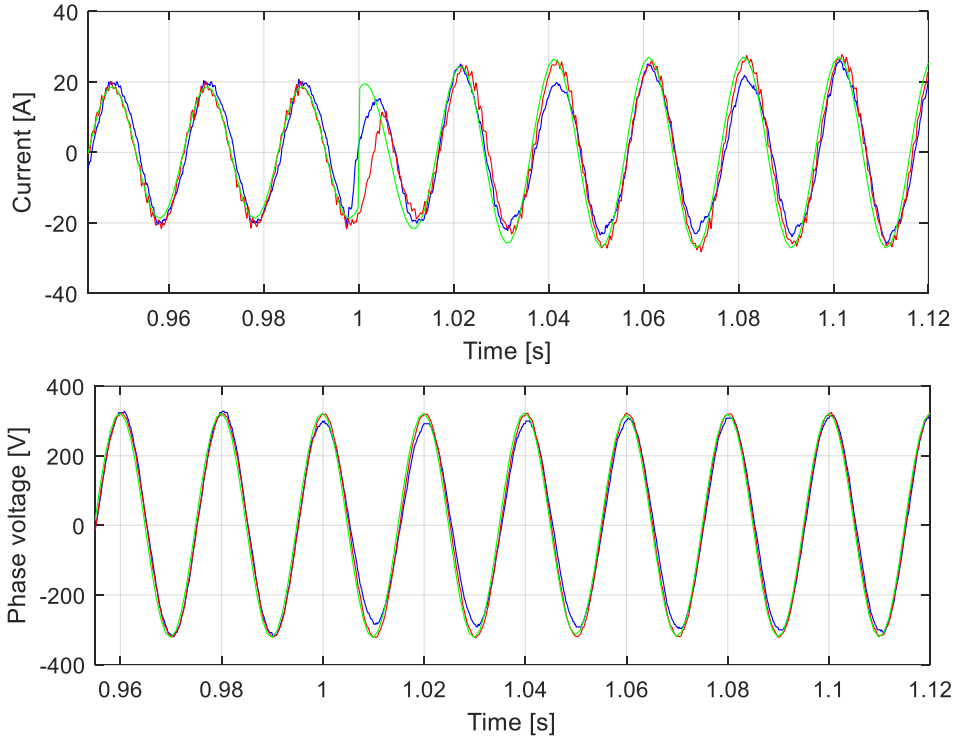

Fig. 24. Scenario C ST current and phase voltage. Experimental data (blue line), PSCAD (red line) and SM (green line).

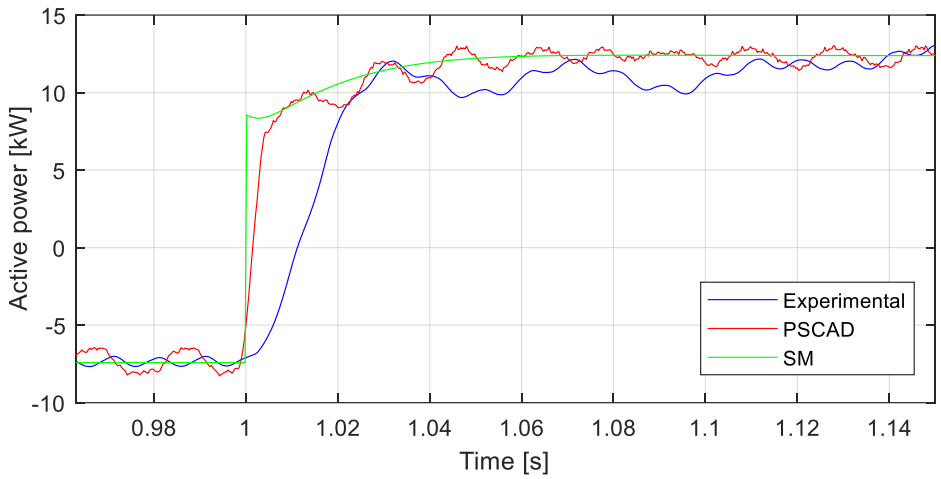

Fig. 25. Scenario C ST active power. Experimental data (blue line), PSCAD (red line) and SM (green line).

In conclusion, the experimental campaign shows that the proposed SM is in good agreement with the measurements and the PSCAD simulation, with some minor differences that can be mainly ascribed to the following reasons. Firstly, the load is unknown due to its stochastic behaviour and it cannot be directly measured due to SPM actual layout. Secondly, inverter and DC-DC converter internal controller details and computational delays are not precisely known (modulation strategy, carrier frequency, filters data and so on) since the producer did not share detailed information. Finally, the electrochemical dynamics in the ST system are not taken into account in the SM and PSCAD one. Nevertheless, the results allow considering the SM sufficiently reliable to be implemented for the validation and preliminary test of innovative control strategies and EMS for islanded no-inertia MGs. In particular, the SM ODE could constitute the set of constraints for a Model Predictive Controller (MPC) aimed at regulating the MG voltages and frequency. The flexibility of the structure of the SM allows extending it at different assets of MGs characterized by a heterogeneous generation mix.

3.8 Chapter 3 Conclusions

This chapter aimed at providing an experimental validation of a modelling approach to study the behaviour of no-inertia MGs in islanded configuration. Such model describes the MG with a system of ODEs representing a first harmonic dynamics of the power electronic devices and of all the components at the DC converters side. The coupling among the various MG components is achieved by means of a steady-state representation of the AC section of the MG using the extended admittance matrix. The main advantage of the SM is that it can be easily interfaced with many different control logics in order to provide a preliminary evaluation of the controller expected performances in an easy but effective way, reducing the commissioning cost. The proposed model has been validated against a detailed simulation in the PSCAD-EMTDC environment and with data acquired during a measurement campaign on a portion of the SPM islanded from the rest of the campus grid. Results highlighted a good trade-off between accuracy and computational effort, suitable for a first assessment of innovative control approaches.

4 Microgrid stability

The aim of this chapter is to present and to discuss a novel procedure, developed by the student, to study MG stability under some conditions.

4.1 Introduction

Islanded (or autonomous) MGs are the most challenging ones especially if no-inertia MGs are concerned (MGs where all the power generating units are connected to the MG by means of power electronic devices). With such MGs, stability issues claim for specific analysis methods as approaches developed for classical power system can seldom be applied due the presence of power electronic devices (highly nonlinear) and to the reduced or null inertia [51, 52]. The importance of such a topic is witnessed by the relevant number of studies performed by researchers under different configurations. Nevertheless, stability studies on MGs have been mainly performed using small signal stability theory. In particular, small signal models for inverters [53], synchronous generators [54], rectifiers [55] and induction motors [56] have been deeply investigated.

The major drawback of a small signal stability approach is related to the fact that the results validity is limited to a neighbourhood of a specific working point (whose magnitude is unknown) [57]. Therefore, it is not possible to provide an estimation of the amplitude of the disturbance that can be withstood without compromising the system stability. To overcome this problem, the system needs to be analysed accounting for its intrinsic nonlinearity and this can be done in two main ways: *i*) using numerical simulations and *ii*) applying the Lyapunov theory [58]. The first approach allows an accurate evaluation of the system stability but does not provide any analytical stability conditions. Therefore, a complete simulation of the system must be run for each configuration one needs to analyse. This results in a limited analysis of the system with a prohibitive computational effort [59]. On the other hand, Lyapunov based approaches have not been positively applied to assess the stability of traditional power systems due to their relevant extension and complexity. On the contrary, MGs are of limited extension by their nature, making Lyapunov stability approaches [59, 60] much more appealing. In this framework, researchers have focused their efforts on the definition of Lyapunov functions for the stability assessment for the whole MG system as well as on the stability assessment of individual sub-systems (synchronous generators, power converters and motor loads) [59].

While the overall MG stability has been analysed in a limited amount of works, which usually involve complex techniques such as the genetic algorithm [61] or Takagi-Sugeno multi-modeling approach [62], the number of studies involving the stability individual sub-systems is surely higher. In particular, droop controlled inverters have been investigated in [63-65]. More in detail, in [63, 64] an equivalence between the inverter DC side capacitance dynamics and the rotating machine rotor one is established, while the authors of [65] have developed a reduced order model for the system that allowed finding the energy function and the stability conditions.

Unfortunately, some of the assumptions on which it is based e.g. inductive infrastructure and voltage/reactive power droop controller disabled, make the configuration quite unrealistic for Low-Voltage (LV) and Medium-Voltage (MV) MGs applications.

To do so, it is also necessary to consider the control architecture implemented in the MG. On this topic, the most diffuse approach to manage islanded MGs is the droop logic [66], thanks to its capability to guarantee the load sharing without communication and to integrate both traditional and under converter generation units [67]. In accordance with the analysis provided before, the approaches to assess the stability of droop controlled islanded MGs are very limited and all of them relies on the small-signal stability theory [68].

In this framework, the goal of this chapter is to find a new and simple formulation, able to evaluate the MG stability with the classic droop control technique described in [24], without the necessity of numerically finding an equilibrium point as required in the small signal stability approach. This is the reason why it is not possible to compare them directly. Such method is firstly presented for an easy case of two sources with no reactive power droop and a mathematical proof of the obtained analytical stability conditions is given. Then, thanks to some reasonable approximations, the validity of such condition is extended to the general case of a MG with *N* generating units with both the droop control channels enabled. The proposed method is then validated comparing its results with the ones provided by numerical simulations performed in the PSCAD-EMTDC environment that represents all the MG components and controllers in deep details.

4.2 Problem Statement

4.2.1 Droop controlled MG mathematical model

Let us consider the generic no-inertia MG layout depicted in Fig. 26, with *N* droop-controlled sources.

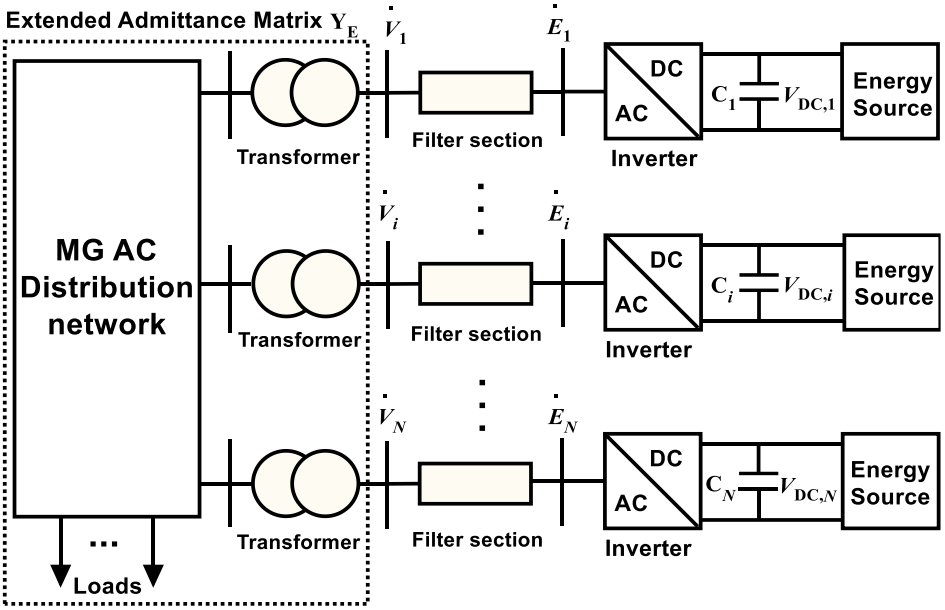

Fig. 26 General layout of a no-inertia, islanded MG

The *i*-th droop controlled energy source is managed according to the well-known control logic proposed in [69] and in Fig. 27, where the DC/AC converter controller is divided in droop controller, voltage controller and current controller.

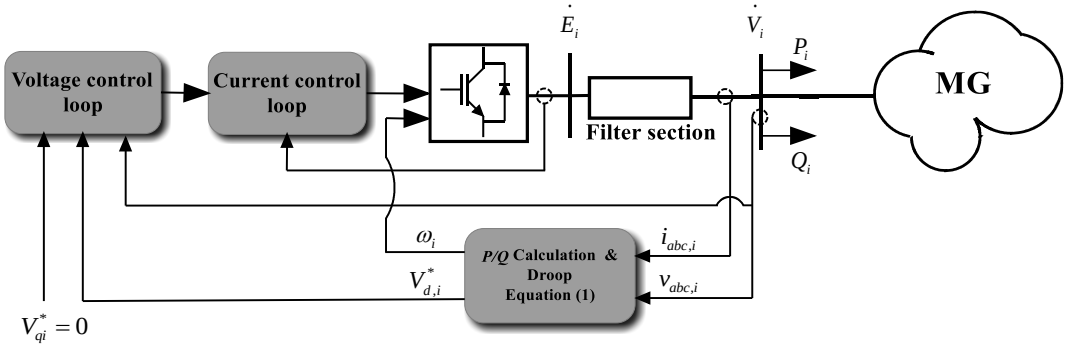

Fig. 27 DC/AC Converter Control Scheme

The droop controller provides the modulation frequency (ω_i) and the direct-axis voltage reference ($V^*_{d.i}$) of the DC/AC converter according to the well-known droop control scheme:

$$\begin{cases} \omega_i - \omega_n = m_i \left(P_{set,i} - P_i \right) \\ V^*_{d,i} - V_{ni} = n_i \left(Q_{set,i} - Q_i \right) \end{cases} \tag{29}$$

where $P_{set,i}$ and $Q_{set,i}$ are the active and reactive power set-points values, V_{ni} is the voltage set-point and ω_n is the system rated frequency [24]. Moreover, P_i, Q_i are the actual active power and reactive power while m_i and n_i are the active and reactive power droop coefficients.

The voltage control loop receives as input the d-q voltage references and provides the d-q current references to the current control loop.

The current control loop provides the modulating signals for the *i*-th DC/AC converter. For sake of completeness a detailed description of voltage and current control loops can be found in [69]. Finally, it is important to remind that the following relationship holds between the *i*-th converter frequency ω_i and corresponding angle δ_i:

$$\delta_i' \equiv \frac{d\delta_i}{dt} = \left(\omega_i - \omega_n\right)\omega_{base} \tag{30}$$

ω_{base} being the system rated angular frequency.

Under the hypothesis that *i*) the AC grid is at steady state and *ii*) the loads can be modeled as constant impedance [70], the AC network can be represented with the extended admittance matrix, $\boldsymbol{Y}_E=\boldsymbol{G}_E+j\boldsymbol{B}_E$ so that the active/reactive power injections at *i-th* bus can be computed as follows [71]:

$$P_i = \mathrm{Re}\left\{\overline{V_i}\left(\sum_{k=1}^{N} Y_{E,ik}\,\overline{V_k}\right)^*\right\} = V_i\sum_{k=1}^{N} V_k\left(G_{E,ik}\cos(\delta_i-\delta_k)+B_{E,ik}\sin(\delta_i-\delta_k)\right) \tag{31}$$

$$Q_i = \mathrm{Im}\left\{\overline{V_i}\left(\sum_{k=1}^{N} Y_{E,ik}\,\overline{V_k}\right)^*\right\} = V_i\sum_{k=1}^{N} V_k\left(G_{E,ik}\sin(\delta_i-\delta_k)-B_{E,ik}\cos(\delta_i-\delta_k)\right) \tag{32}$$

where the * operator represents the complex conjugate and $\overline{V_i} = V_i e^{j\delta_i}$, δ_i being the angle of the voltage of the *i*-th source and V_i the voltage amplitude. Extensive validation of the above-mentioned assumptions can be found in [70] together with the treatment of the more general case of a load described with a generic algebraic relationship in the voltage/current plane (such as constant power load).

Assuming the steady state of the voltage and current controllers one has that:

$$V_i = V_{d,i}^* \tag{33}$$

So, inserting (32) and (31) in(29), one has that, for any $i = 1,\ldots,N$

$$\begin{cases} \delta_i' = \omega_{base} m_i\left(P_{set,i} - V_i\sum_{k=1}^{N} V_k\left(G_{E,ik}\cos(\delta_i-\delta_k)+B_{E,ik}\sin(\delta_i-\delta_k)\right)\right) \\ n_i B_{E,ii} V_i^2 - V_i\left(n_i\sum_{\substack{k=1,\ldots,N\\ k\neq i}} V_k\left(G_{E,ik}\sin(\delta_i-\delta_k)-B_{E,ik}\cos(\delta_i-\delta_k)\right)+1\right)+V_{ni}+n_i Q_{set,i}=0 \end{cases} \tag{34}$$

System (34) is a Differential Algebraic Equation (DAE) system whose general form is:

$$\begin{cases} \mathbf{y}' = \mathbf{f}\left(\mathbf{y},\mathbf{x},\mathbf{k}\right) \\ \mathbf{0} = \mathbf{g}\left(\mathbf{y},\mathbf{x},\mathbf{k}\right) \end{cases} \tag{35}$$

$$\mathbf{y} = \left[\delta_1,\ldots,\delta_N\right]^T \quad \text{and} \quad \mathbf{x} = \left[V_1,\ldots,V_N\right]^T$$

while all other parameters (droop coefficients, network admittance matrix elements and so on) are collected in the multidimensional variable **k** for the sake of readability. Obviously, **f** and **g** are multidimensional functions that reproduce relations (34).

4.2.2 Equilibria of a droop-controlled MG

Let suppose that an equilibrium point $(\mathbf{y}_0, \mathbf{x}_0, \mathbf{k}_0)$ for the considered MG exists, i.e.:

$$\begin{cases} \mathbf{0} = \mathbf{f}(\mathbf{y}_0, \mathbf{x}_0, \mathbf{k}_0) \\ \mathbf{0} = \mathbf{g}(\mathbf{y}_0, \mathbf{x}_0, \mathbf{k}_0) \end{cases} \tag{36}$$

any perturbation in the network (e.g. a load change, a line opening or closing, etc.) can be coded in a change of **k** from $\mathbf{k_0}$ to $\mathbf{k}_1$. As a consequence, the dynamic of the MG is described by (35) setting $\mathbf{k}=\mathbf{k}_1$ and initial values $\mathbf{y}(0)= \mathbf{y}_0$.

Under this consideration, the "stability of the MG" corresponds to the existence of a new equilibrium point and the possibility to reach it after the contingency. The common approach adopted to face such a problem relies on the Lyapunov's linearization method [72]: if the system linearized around the new equilibrium point $\mathbf{y_1}$ is strictly stable (i.e. all eigenvalues of the Jacobian Matrix of the system are strictly in the left-half complex plane), then the equilibrium point is *locally* asymptotically stable. However, as shown in an easy example in the Appendix, this result does not guarantee that the new equilibrium point is reached starting from the initial point y_0. In other words, one should still verify that the initial condition belongs to the *domain of attraction* of the final equilibrium point [72].

4.3 Proposed Approach

In the present section, an alternative approach to assess a MG large-signal stability is proposed starting from a simple case in which a two sources MG is considered provided with active power droop law enabled (first of (29)) and reactive power droop law disabled (second of (34)). For this reason, voltages V_i are supposed to be constant. The results achieved in §4.3.1Subsection III-A are then generalized for any no-inertia, droop-controlled MG layout in §4.3.2.

4.3.1 Two sources MG configuration

Rewriting the first of (34) for N=2 and summing up the two differential equations, the following mono-dimensional Cauchy problem can be written:

$$\begin{cases} y' = f(y) \\ y(0) = y_0 \end{cases} \tag{37}$$

being

$$\begin{cases} f(y) = \mathrm{A}(y) + \mathrm{B}(y)\cos(y) + \mathrm{C}(y)\sin(y) \\ y = \delta_1 - \delta_2 \\ y_0 = \delta_{10} - \delta_{20} \end{cases} \tag{38}$$

having defined:

$$\begin{cases} \mathrm{A}(y) = \omega_{base}\left[m_1\left(P_{n1} - V_1^2(y)G_{E,11}\right) - m_2\left(P_{n2} - V_2^2(y)G_{E,22}\right)\right] \\ \mathrm{B}(y) = \omega_{base}V_1(y)V_2(y)G_{E,12}(m_2 - m_1) \\ \mathrm{C}(y) = -\omega_{base}V_1(y)V_2(y)B_{E,12}(m_2 + m_1) \end{cases} . \quad (39)$$

Notice the difference between B_E and B(y) (or simply B), where the first one stays for the imaginary part of the admittance, instead the latter represents the coefficient introduced in (38).

The stability analysis focuses on the research of a constant solution for (37) that implies constant active power flows.

Since $f \in C^{\infty}(\mathbb{R})$, i.e. is a continuous and differentiable function, (37) is a Cauchy problem with existence and uniqueness of the solution. So, if $f(y_0)=0$ then the solution is $y(t)=y_0$. Otherwise, if $f(y_0)\neq 0$, then, due to the continuity of f, one can assume that an interval I exists containing y_0 and where f is always not null; therefore the solution is easily obtained as:

$$y = H^{-1}(t) \quad (40)$$

with

$$H(z) = \int_{y_0}^{z} \frac{ds}{f(\mathrm{s})} \quad (41)$$

whose invertibility is a consequence of the continuity of the constant sign of f in I.

If the reactive control is disabled (setting all the reactive droop coefficients (29) to zero), then the voltages constant and A, B, C are no more dependant on y. With this assumption, f becomes just a trigonometric function.

Rewriting f as:

$$f(y) = \mathrm{A} + \sqrt{\mathrm{B}^2 + \mathrm{C}^2}\cos(\mathrm{y} - \phi) \quad (42)$$

with ϕ such that:

$$\begin{cases} \cos\phi = \dfrac{B}{\sqrt{B^2 + C^2}} \\ \sin\phi = \dfrac{C}{\sqrt{B^2 + C^2}} \end{cases} \quad (43)$$

Let us show that

$$\mathrm{A}^2 - \mathrm{B}^2 - \mathrm{C}^2 \leq 0\,. \quad (44)$$

is a sufficient condition that ensures that the limit for t approaching infinity of the solution y exists and it is bounded.

More precisely, if (44) is not verified, then (42) does not admit zeros, hence it is easy to obtain that H is unbounded and defined in $I=\mathbb{R}$; this implies that y diverges. Otherwise, if condition (44) is verified, the zeros of f belong to the following set:

$$Z=\left\{\pm\arccos\left(-\frac{\mathrm{A}}{\sqrt{\mathrm{B}^2+\mathrm{C}^2}}\right)-\phi+2k\pi\ ,k\in\mathbb{Z}\right\}. \tag{45}$$

The domain of H can be obtained evaluating the order of the zeros of f. To this aim, the value of the first and second derivative of f for any $\bar{y}\in Z$ is necessary:

$$f'(\bar{y})=\begin{cases}-\sqrt{\mathrm{B}^2+\mathrm{C}^2-\mathrm{A}^2} & 2k\pi\le\bar{y}+\phi<(2k+1)\pi\\ \sqrt{\mathrm{B}^2+\mathrm{C}^2-\mathrm{A}^2} & (2k+1)\le\bar{y}+\phi<2(k+1)\pi\end{cases} \tag{46}$$

and

$$f''(\bar{y})=-A\ . \tag{47}$$

This means that $\bar{y}$ is a zero of first order if A^2-B^2-C^2<0, otherwise, if A^2-B^2-C^2=0, $\bar{y}$ is a second order zero. In both the cases, the order of the zero is greater or equal than one so the integral function that defines H diverges in $\bar{y}$. Then, once (44) is verified, the domain of H is $I=(\bar{y}_1,\bar{y}_2)$, with $\bar{y}_1,\bar{y}_2\in Z$, such that $\bar{y}_1$ is the largest zero of f such that $\bar{y}_1<y_0$ and $\bar{y}_2$ is the smallest zero of f such that $y_0<\bar{y}_2$. Moreover, if f is positive (negative) in I, then $\lim_{y\to\bar{y}_1^+}H(y)=-\infty$ $(+\infty)$ and $\lim_{y\to\bar{y}_2^-}H(y)=+\infty$ $(-\infty)$, meaning that:

$$\lim_{t\to+\infty}y(t)=\lim_{t\to+\infty}H^{-1}(t)=\bar{y} \tag{48}$$

where

$$\bar{y}=\begin{cases}\bar{y}_1 & \text{if } f(y_0)<0\\ \bar{y}_2 & \text{if } f(y_0)>0\end{cases} \tag{49}$$

This proves that (44) is a sufficient condition to obtain a solution y that becomes constant for t large enough, i.e. for the existence of a final working point such that y_0 belongs to its domain of attraction.

4.3.2 Extension of the proposed approach to a generic MG layout

In order to extend the previous results to a more realistic configuration two main issues need to be addressed:

- the necessity to a consider MG layout with more than two droop-controlled power sources;
- the inclusion of the reactive power/voltage droop law (i.e. considering the second of (34)).

This is done making some simplifying assumptions on (34) that allow describing the MG dynamics in an approximate way with *N-1* decoupled differential equations of the

kind (37)-(38) and so to assess the MG stability with *N-1* conditions of the kind of (44).

With this goal in mind, it should be observed that the second of (34) can be seen as a system of N algebraic equations in the N unknowns voltage amplitudes V_i, for any $i=1,...,N$. Its solution can provide the correlation between voltage amplitudes and phases. However, as such system is seldom analytically solvable, a simplified approach is here proposed.

Let us reconsider the second of (34); supposing that the i-th converter voltage is weakly affected by the angular variations and the other converters voltages, one can assume that:

$$\begin{cases} \delta_i - \delta_k = \delta_{i0} - \delta_{k0} \\ V_k = V_{k0} \quad k \neq i \end{cases} \tag{50}$$

being δ_{i0}, δ_{k0} and V_{k0} the angular phases and voltages initial values. Thanks to this assumption, the second of (34) becomes a set of decoupled, second degree algebraic equations that can be solved in order to find the values of V_i. Simulations proposed in the next section will show, if the final working point exists, then assumptions (50) are reasonable. Otherwise, the solution of (34) is of no use as no final steady-state exists.

The assumption (50) has two main consequences: *i*) it allows solving in an approximate but analytical way the nonlinear algebraic system and *ii*) it provides a value for the bus voltages to be used in the first of (34).

This implies that the right-hand side of the differential equations in (34) is again as a linear combination of trigonometric functions. Such property is fundamental if one aims at extending the results obtained for the two sources case presented in the previous section.

The final step one needs to make in order to extend the results of the simplified test case is to consider the angular differences rather than the single angle dynamics. Let us rewrite the first of (34) in terms of angular differences as follows:

$$\begin{aligned} \delta_i' - \delta_j' = {} & \omega_{base} m_j V_j \sum_{\substack{k=1 \\ k \neq i}}^{N} V_k \left(G_{E,jk} \cos(\delta_j - \delta_k) + B_{E,jk} \sin(\delta_j - \delta_k) \right) + \\ & - \omega_{base} m_i V_i \sum_{\substack{k=1 \\ k \neq j}}^{N} V_k \left(G_{E,ik} \cos(\delta_i - \delta_k) + B_{E,ik} \sin(\delta_i - \delta_k) \right) + \omega_{base} m_i G_{E,ii} V_i^2 - \omega_{base} m_j G_{E,jj} V_j^2 \end{aligned} \tag{51}$$

for any $i,j=1,\ldots,N$ such that $i \neq j$.

In a MG with N sources there are $K=(N^2-N)/2$ possible angular differences. Among these, only $N-1$ are linearly independent. Following the criteria that led to the study of large power systems stability [73], let's suppose to divide the set of angular differences in two groups: the first set, from now on named Critical Sources (CS) set, contains $N-1$ differences that satisfy the following properties: *i*) they are linearly independent and *ii*) they are the ones that, in the initial instant, assume the $N-1$ highest amplitudes among all the possible differences. The remaining $K-N+1$ differences are indicated as Non-Critical Sources (NCS) set.

Now, reconsidering the right-hand side of (51) in the hypothesis that δ_i - $\delta_j \in CS$, the following approximation can be done:

$$\delta_{i(j)} - \delta_k = \begin{cases} \delta_{i(j)0} - \delta_{k0} & \text{if } \delta_{i(j)} - \delta_k \in NCS \\ \delta_{i(j)} - \delta_{j(i)} + \delta_{j(i)} - \delta_k \cong & \\ \delta_{i(j)} - \delta_{j(i)} + \delta_{j(i)0} - \delta_{k0} & \text{if } \delta_{i(j)} - \delta_k \in CS \end{cases} \tag{52}$$

The meaning of (52) is that angular differences belonging to the NCS can be frozen to their initial value while for angular differences belonging to the CS set there is the necessity to highlight the δ_i - δ_j term. This is done by adding and substituting δ_j to the angular difference itself. In this second case, a residual difference δ_j - δ_k appears. Since the CS set is defined by linearly independent differences δ_j - δ_k must belong to NCS set and thus it can be frozen.

The idea supporting assumption (52) is that machine angles that were close to each other at the beginning of the transient remain sufficiently close to each other during the whole transient, due to the fact that both the initial point and the eventual final one are determined by the same control laws.

According to (52) and exploiting trigonometric properties of sinusoidal and cosinusoidal functions, one has that (51) is reduced to the following set of *N-1* independent differential equations:

$$\begin{cases} \left(\delta_i - \delta_j\right)' = A_{ij} + B_{ij}\cos(\delta_i - \delta_j) + C_{ij}\sin(\delta_i - \delta_j) \\ \left(\delta_i - \delta_j\right)(0) = \delta_{i0} - \delta_{j0} \end{cases} \tag{53}$$

which have the same form as (38). So the MG dynamic converges to an equilibrium working point if N–1 conditions of the kind (44) are satisfied, e.g.:

$$A_{ij}^2 - B_{ij}^2 - C_{ij}^2 \le 0 \tag{54}$$

ij are subscripts corresponding to CS set sources.

4.4 Validation of the Proposed Approach

The aim of the present section is to validate the proposed procedure comparing the results obtained with the ones provided by an electromagnetic simulation performed using PSCAD-EMTDC [6] environment that allows representing all the MG components with a high level of details. It is worth pointing out that in the proposed PSCAD simulations all the MG control loops are represented in detail (e.g. voltage and current control loops as depicted in Fig. 27) differently from what has been done to define the proposed simplified approach.

Since MGs are usually of limited extension by definition, validation testbeds usually account for three sources configurations [56, 74]. For this reason, let us consider a LV MG with N=3 sources and the electric diagram of Fig. 28.

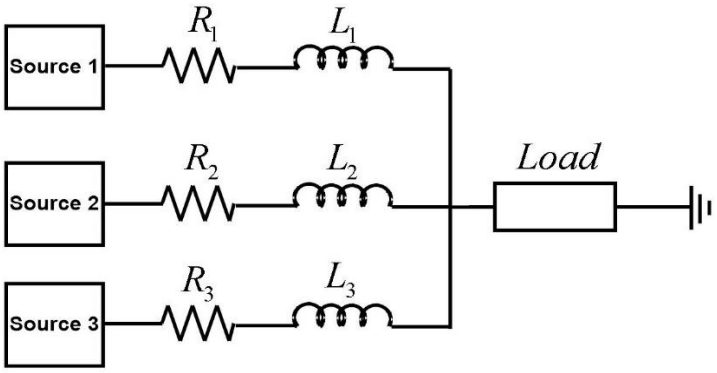

Fig. 28 Test case MG layout.

The MG AC rated voltage is equal to 0.4 kV. Network parameters have been chosen carefully to produce some unstable operational points in order to better highlight the results of the proposed approach. Table 9 reports the AC distribution system parameters while Table 10 collects the data of each droop-controlled unit. Per unit parameters of the droop controllers are defined on each source rated power A_n.

Table 9 AC grid parameters

R_1	L_1	R_2	L_2	R_3	L_3
0.36 Ω	0.45 mH	0.36 Ω	0.45 mH	0.44 Ω	4.5 mH

Table 10 – droop-controlled sources parameters

Source	A_n	P_{set}	Q_{set}	m	n
Source 1	7 kVA	5 kW	5 kVAr	-6 %	-0.5 %
Source 2	14 kVA	10 kW	10 kVAr	-6 %	-0.5 %
Source 3	140 kVA	100 kW	100 kVAr	-6 %	-0.5 %

Without any loss of generality, the MG load is represented as resistive-reactive parallel impedance [70]. The MG initial working point is characterized by a load absorption of 16 kW and 6.4 kVAr, corresponding to a load series impedance of $8.63+j\,3.44\ \Omega$ calculated at the MG rated voltage. Starting with this load conditions and equipping the sources with the active and reactive power droop laws, the solution of the load flow equations allows evaluating the power generations and the voltage phasors of the three sources (Table 11).

Starting from this working point, two load variations are analysed in detail. The first one (§4.4.1) corresponds to a "stable transient" while the second (§4.4.2) is an "unstable one". For each of the two test-cases, a first evaluation of the transient is performed by means of the PSCAD simulation. Following, the application of the proposed procedure is provided to assess its effectiveness.

Finally, §4.5 provides a practical application of the proposed approach: starting from a given initial point, a map of all the possible load variations is drawn that leads to a stable final steady-state condition.

Table 11 MG initial working point

Source	P_0	Q_0	δ_0	V_0
Source 1	0.72 kW	4.89 kVAr	0°	400.0 V
Source 2	1.44 kW	5.51 kVAr	0.042°	400.9 V
Source 3	14.36 kW	-2.20 kVAr	8.258°	402.0 V

4.4.1 Test-case 1

This case is representative of an increase of the load active and reactive power passing from 16 kW and 6.4 kVAr to 64 kW and 25 kVAr after 2s from the beginning of the simulation. The final working point corresponds to a load impedance of 2.17+*j* 0.85 Ω calculated at the MG rated voltage. As one can see from Fig. 29 the sources frequencies change according to the droop laws, until reaching the same steady-state value, corresponding to a stable equilibrium point for system (34). Stability can also be verified from Fig. 29 and Fig. 30 where both the angular differences and the voltage amplitudes converge to a steady-state solution.

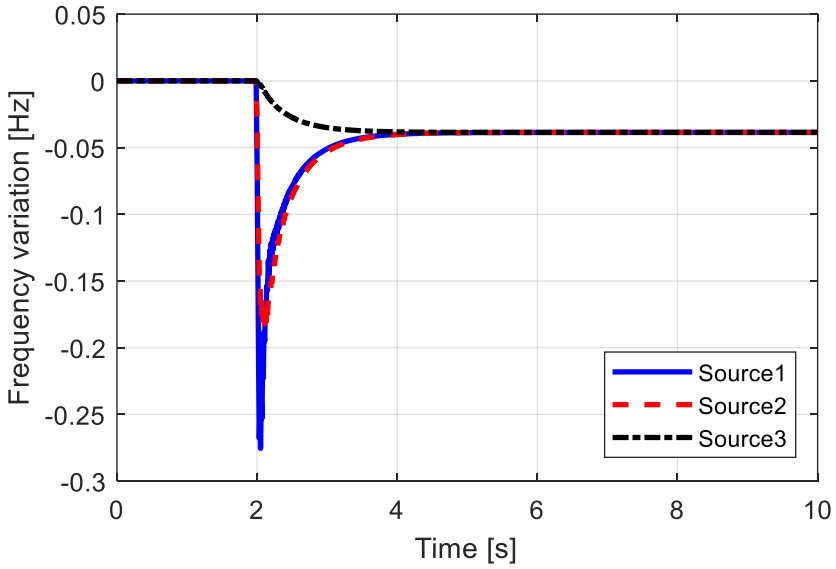

Fig. 29 Frequency variation time profile for test-case 1.

The initial angle differences, in accordance with the data reported in Table 11, are:

$$\begin{cases} \delta_{10} - \delta_{20} = -0.042° \\ \delta_{10} - \delta_{30} = -8.258° \\ \delta_{20} - \delta_{30} = -8.300° \end{cases} \tag{55}$$

According to (55), The CS set consists of δ_1- δ_3 and δ_2- δ_3, while the NCS set includes δ_1- δ_2. This fact is also confirmed by the PSCAD simulation, where in Fig. 30 one can see that δ_1- δ_2 is almost constant during the transient while the most meaningful variation occurs in the differences belonging to the CS set.

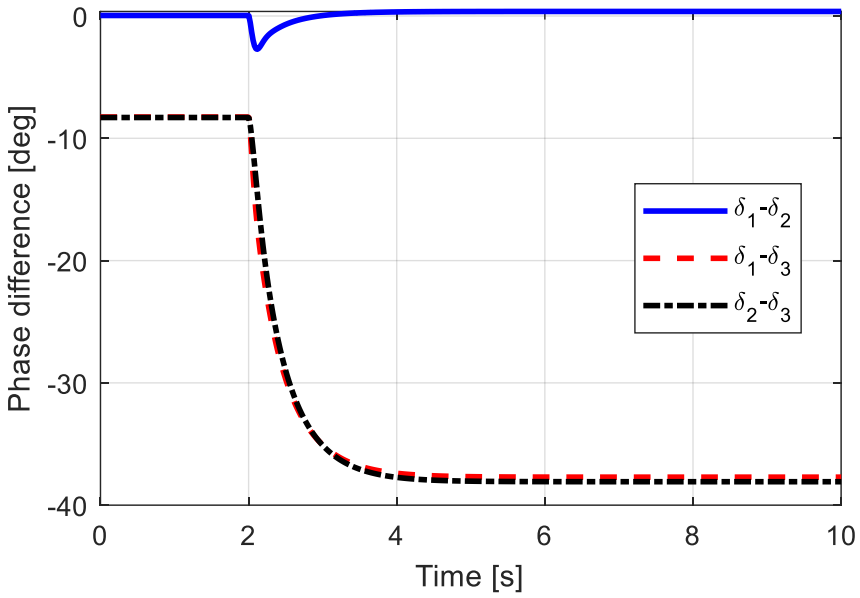

Fig. 30 Angular differences time profile for test-case 1.

In accordance with the proposed procedure, it is now necessary to get an estimation of the three sources voltages considering the second of (34) under assumption (50). For the considered test-case one obtains:

$$\begin{cases} V_1 = 399.6 \quad V \\ V_2 = 400.8 \quad V \\ V_3 = 401.9 \quad V \end{cases} \tag{56}$$

Please note that the exact initial values appearing in Fig. 31 are very close to the approximate ones reported in (56), which is, to a certain extent, a justification of assumption (50).

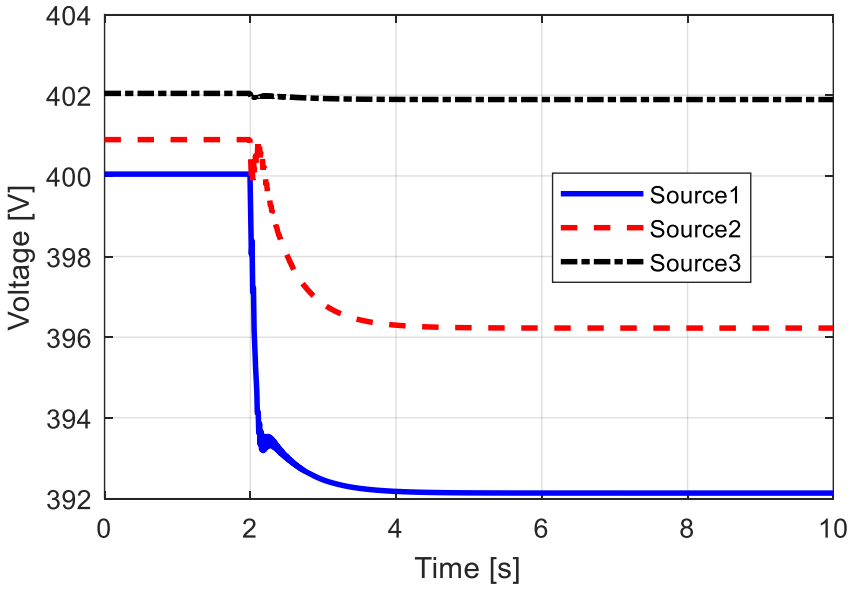

Fig. 31 Voltages time profile for test-case 1.

Using (56) it is possible to calculate the stability coefficients for the two angular differences of the CS set, as reported in Table 12.

Table 12 Test-case 1 stability coefficients

	$\delta_1-\delta_3$	$\delta_2-\delta_3$
A_{ij}	0.0851	0.0426
B_{ij}	-0.0315	-0.0141
C_{ij}	0.0941	0.0515
$A_{ij}^2 - B_{ij}^2 - C_{ij}^2$	-0.0026	-0.0010

As one can notice from the last row of Table 12, conditions (54) are verified for both the angular differences of the CS set, thus indicating the stability of the final working point. This consideration is in accordance with the results provided by the numerical simulation.

4.4.2 Test-case 2

This case is representative of a much higher power increase occurring at 2 s from the initial value defined in Table 11 to 91 kW and 36.4 kVAr, corresponding to an impedance of 1.51 + *j*0.60 Ω calculated at the MG rated voltage.

Simulation results for the sources frequencies are reported in Fig. 32. As one can see, frequencies diverge which means that no final equilibrium is reached.

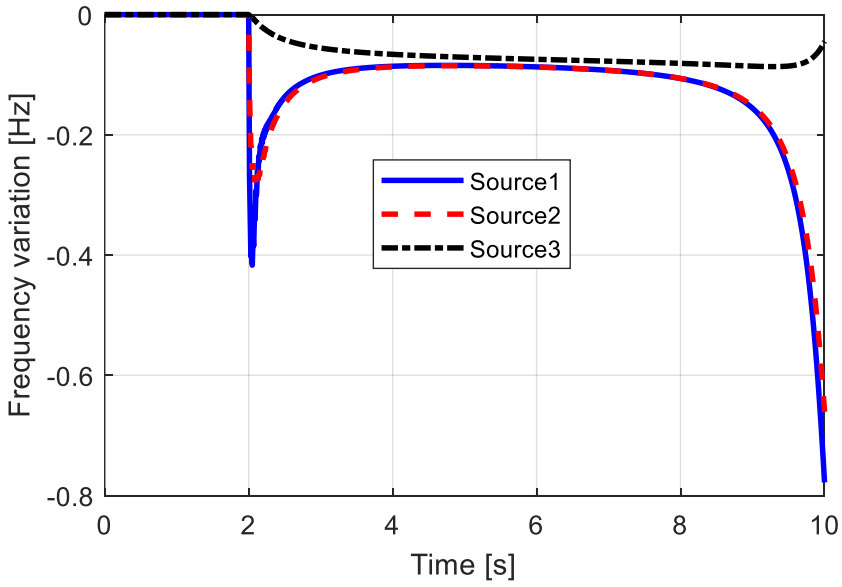

Fig. 32 Frequency variations time profile for test-case 2.

Instability can also be verified from Fig. 33 and Fig. 34 where both the voltage amplitudes and the angular differences of the CS are characterized by a divergent behaviour.

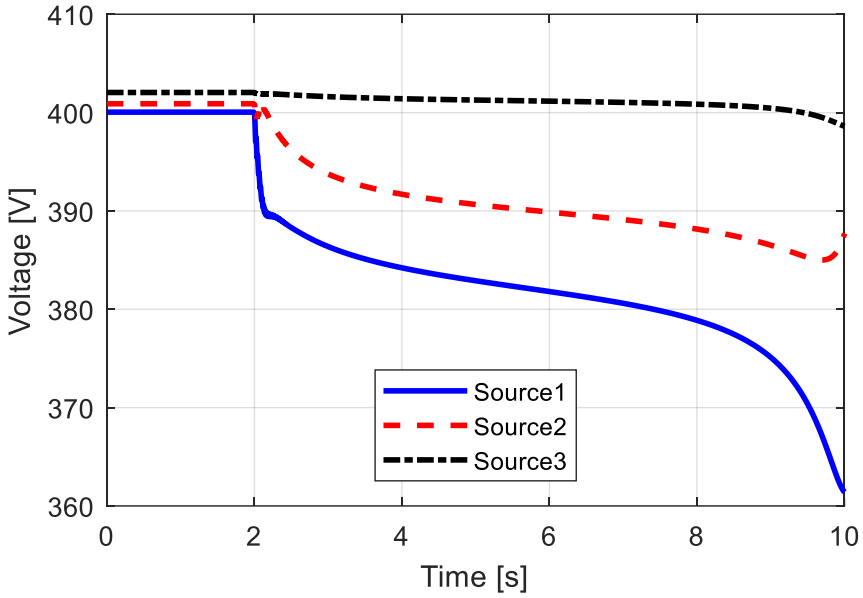

Fig. 33 Voltages time profile for test-case 2.

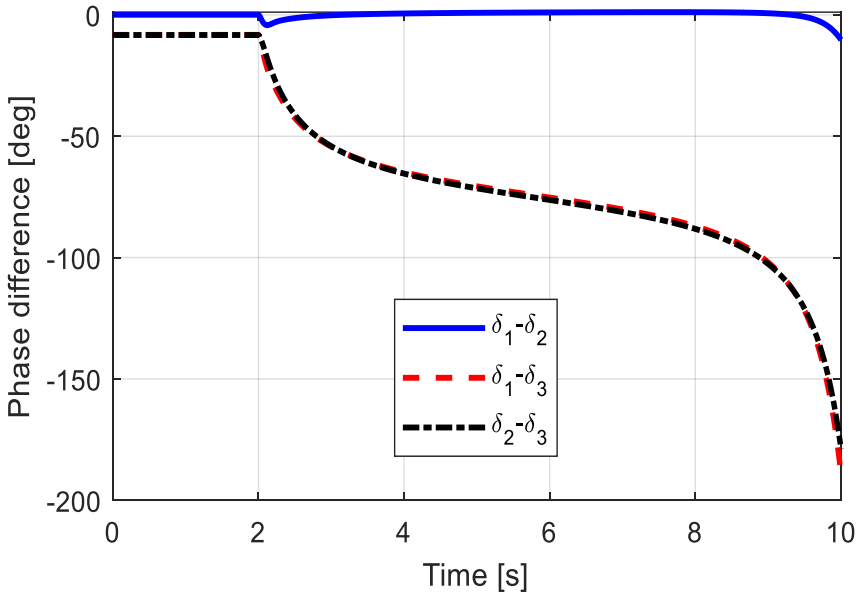

Fig. 34 Angular differences time profile for test-case 2.

Since the initial point of the transient is the same as for test-case 1, the initial differences are again given by (55) and the CS set and the NCS set are the same of §4.4.1. Eq. (34) with assumption (50) leads to:

$$\begin{cases} V_1 = 399.3 \quad V \\ V_2 = 400.2 \quad V \\ V_3 = 401.9 \quad V \end{cases} \tag{57}$$

Also in this second test-case, Fig. 34 confirms the hypothesis that the dynamic of the NSC set angular differences is negligible with respect to the one of the CS set that are the cause of the system instability. Once again, it is possible to calculate the stability coefficients for the two angular differences of the CS set for test-case 2, as reported in Table 13.

Table 13 – Test-case 2 stability coefficients

	$\delta_1-\delta_3$	$\delta_2-\delta_3$
A_{ij}	0.1047	0.0530
B_{ij}	-0.0303	-0.0136
C_{ij}	0.0910	0.0499
$A_{ij}^2 - B_{ij}^2 - C_{ij}^2$	0.00176	0.00014

From the last row of Table 13 one can see that conditions (54) are not verified for both the angular differences of the CS set. This implies that the proposed method is correctly pointing out the instability of the considered final working point, as verified by means of the numerical dynamic simulation.

4.5 Evaluation of the Overall Stability Region of the Considered MG Layout.

The developed approach allows performing with MGs what is typically done for traditional power systems in the so-called Dynamic Security Assessment (DSA) framework [73]. Given a MG layout and a specific working point, one can generate a set of reasonable contingencies or events and check whether the MG is able to withstand them or not.

More in details, let us reconsider the network of Fig. 28, the MG-DSA can be obtained as follows:

- Acquire the MG initial working point
- Define the angular differences CS and NCS sets;
- Define a contingency (e.g. an active and reactive power load variation);
- Check whether conditions (44) are satisfied or not;
- Conclude about the existence and the stability of the final working point.

As an example, the application of the proposed approach allows drawing the DSA map of Fig. 35 (continuous yellow and blue areas). Such a map is drawn in the load active power (P_L) vs. load reactive power (Q_L) plane representing the MG load request and it is calculated starting from the initial working point of Table (white dot in Fig. 35). The blue area represents the set of the P_L-Q_L couples leading to a final stable working point, while the yellow one is the set of load requests that do not allow to reach a final steady-state condition. Examining Fig. 35, it is possible pointing out that the existence of a final stable working point is mostly influenced by the load active power (beyond a load active power of 80 kW no stable working point can be found). In order to validate the results achieved by the DSA map provided by the application of the proposed approach the same DSA map has been obtained by means of detailed PSCAD simulations. For the sake of results readability, a set of 427 contingencies characterized by the load requests given by the red markers appearing in Fig. 35 has been simulated. Star markers indicate the load requests that allow to find out a final stable working point, while unstable ones are represented with a rhombus marker. The validation

shows a good agreement between the proposed approach and the complete simulation, with a slight overestimation of the unstable zone predicted by the simplified approach. However, number at hand, only 27 stable working points over 427 (i.e. 6.3%) are misclassified as unstable by the proposed procedure that is, by the way, a conservative result. This implies *i*) a 93.7 % agreement between the proposed approach results and the detailed PSCAD simulation and *ii*) the fact that no unstable working points are labelled as stable.

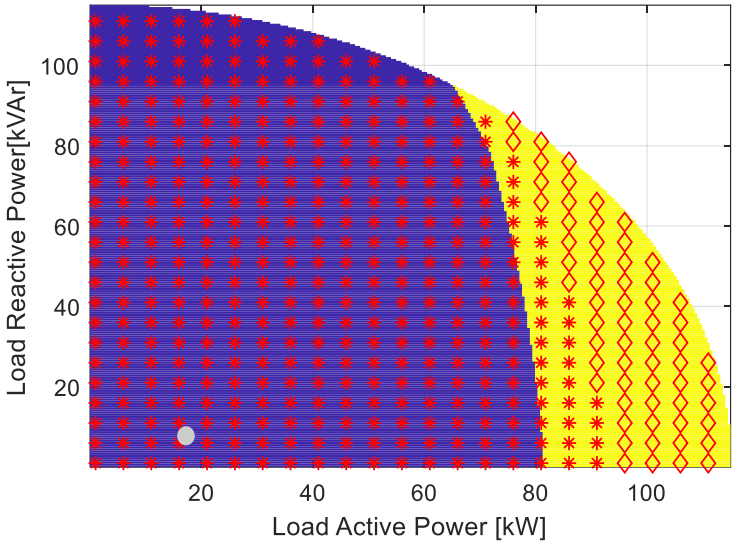

Fig. 35 DSA for the considered MG starting from an initial working point characterized by a load request of 16 kW and 6.4 kVAr.

As a final remark, it is worth noticing that this result cannot be achieved with a linearized, eigenvalues-based approach and that the proposed approach allows reducing the CPU effort in the evaluation of the DSA map. The computational time requested for the proposed approach is 45s, while the exact approach needs 1 hour and 26 minutes (both on an 8Gb RAM, Intel Core i7-6700 CPU at 4.00 GHz machine). Finally, the simplicity of the proposed approach allows its implementation in a MG Energy Management System that, for any operating condition (initial point), can draw the map in real-time. So, the system operator can know in advance whether a contingency can be withstood or not and, in the latter case, evaluate the effectiveness of the actions to be taken to prevent the system from instability.

4.6 Chapter 4 Conclusions

A new method for the evaluation of the stability of a droop-controlled MG was proposed. The approach started from the proof of a stability criterion to be applied to a simple MG configuration characterized by only two power sources. Then the criterion was extended to a general case by means of some simplifying hypothesis.

The validation of the proposed methodology was performed comparing the obtained results with the ones provided by complete simulations in the PSCAD-EMTDC environment. The proposed approach was also applied to perform a DSA of the MG under different working conditions.

In conclusion, the proposed approach has two main advantages with respect to previously developed methods: *i*) it overcomes the problem that, from a theoretical point of view, the existence of a final equilibrium point with all left half-plane eigenvalues does not imply that, for a given initial condition, such final working point will be reached; *ii*) from a numerical point of view, the eigenvalues analysis requires the numerical solution of an algebraic nonlinear system to evaluate all the possible system final working points and the numerical evaluation of the Jacobian matrix system eigenvalues for each of them. On the other hand, the developed stability conditions do not require any numerical solver as they consist of a set of *N-1* inequalities to be verified.

5 MPC Controller for Microgrid

This chapter proposes a novel decentralized and communication-less control strategy for frequency and voltage regulation in PV-Storage islanded MGs. The proposed approach aims at achieving a suitable management of the different operational assets of the PV-Storage islanded MGs providing suitable transition among them in order to achieve a continuous and effective power supply to the system loads. Local inverter controllers are designed exploiting the capabilities of the Model Predictive Control (MPC) achieving an architecture that relying only on local measurements, is able to nullify both frequency and voltage errors. This way, the proposed approach can combine the advantages of the classic droop and master/slave controllers as it does not need neither communication among devices nor a secondary centralized control loop. Moreover, it is able to account for the Storage characteristics imposing a power curtailment of the PV units whenever either the power absorption or the State of Charge (SOC) limit is reached.

Finally, a simple experimental test is presented in order to show an actual implementation of this control algorithm.

5.1 Introduction

Primary microgrids frequency and voltage control strategies can be divided into two main categories depending on the need of an ICT infrastructure or not [75]. ICT based MG control techniques e.g. the so called master/slave control [76, 77] and distributed control [78]. On the other side, among the communication-less primary regulation approaches it is worth citing the droop control [79] and its numerous variants [80]. The main problems of ICT based primary controllers are related to the need for high-bandwidth communication channels, which can be impractical, vulnerable and expensive in MGs with long connection distances among generating units. On the other hand, the droop approach for primary regulation implies two main drawbacks: *i*) frequency and voltage deviations from their rated values, resulting in the need of secondary regulation, and *ii*) the inability to satisfy multiple control objectives [75]. Among the various MGs set-ups, the one that is collecting some relevant interest from producers, customers and researchers is the so called autonomous Photovoltaic-Storage (PV-Storage) configuration [81]. The reason of this interest lays in the large amount of PV installations all over the world and the idea that efficiently shifting the production capability of PV plants significantly improves their exploitability. Moreover, a PV-Storage MG can also be self-sustainable if properly designed [82] providing an important contribution to the electrification of rural areas and to the flexibility and resiliency of existing electric networks.

Beside the simplicity of the idea to integrate PV and Storage devices, many are the problems to be faced to efficiently do it, especially if an autonomous PV-Storage MG is considered [83]. In this latter case, the system needs to be capable to satisfy the load demand, providing frequency and voltage regulation, but also to suitably manage the Storage SOC in order to guarantee the continuity of supply to the MG loads.

For these reasons, the control of islanded PV-Storage configurations was deeply investigated in literature. Previous works focused their attention on solutions where the PV unit and the battery share the same converter [84, 85]. Such a configuration is quite limiting since it cannot be applied for the retrofit of existing PV plants or for configurations where the PV and the Storage are not installed close to each other. Alternative solutions to provide a suitable system regulation without ICT infrastructure were gathered by the installation of diesel generators [86] or by implementing the so called "Virtual Synchronous Generator" [87] in order to create a real or artificial inertial frequency response allowing the application of control solutions based on inertial frequency dynamics. The main drawback of these solutions is the necessity of a dedicated device (a diesel generator or a power converter) to achieve the inertial frequency response, increasing the topological complexity and the cost of the system. Beside these solutions, recent works tried to solve this issue with smart control approaches using the system frequency as a communication signal but without the necessity to install additional devices. In particular, [88] shows a PV-Storage management where each generation unit is provided with a dedicated local primary controller and the frequency produced by each inverter is used to give and receive information about the operational status of the system. The main drawback of [88] is that it needs a secondary controller to restore the MG frequency at its rated value; moreover, it does not take into account the bounds on the system frequency and on the rating of the inverter, limitation that could strongly affect the proper operation of the system. In a recent paper, a MPC approach is proposed to replace traditional PID based ones for the control of inverters fed by renewable power generation [89]. It must be underlined that [89] is one of the very few cases where MPC is proposed for component control rather than for secondary and tertiary control [90, 91]. However, in [89] the MPC controller is only used to merely substitute the classical PID ones but is inserted in a traditional droop-based scheme. Consequently, the method does not nullify frequency and voltage errors; moreover, no hint is provided on the management of different operational assets of the PV-Storage MG (e.g. SOC saturation, Storage power limitations, PV production curtailment, etc.).

So, the aim of the present article is to start from the idea developed in [89] to design local inverter controllers that better exploit the features of the MPC (i.e. predicting the future behaviour of the system and inserting constraints on the variables) providing a plug-and-play control architecture for the islanded PV-Storage system. Such architecture meets both the primary and secondary controller goals (sharing the load request among the sources and zeroing the voltage and frequency errors) without the need of an ICT infrastructure (i.e. based only on local measurements). This combines the advantages of the droop and master/slave controllers recalled at the beginning of this introduction. Moreover, the developed approach can account for the Storage and PV characteristics in order to *i*) manage the storage SOC and power limits *ii*) constrain the PVs to work at their Maximum Power Point (MPP) when possible and curtail their power when necessary and *iii*) guarantee an automatic and seamless transition among the different MG operation assets providing a suitable adjustment of the MPC goals.

5.2 General Overview and Structure of the Proposed Control

The considered MG configuration consists of a Storage unit and N_{PV} PV systems, each interfaced with the AC MG distribution system via power electronics converter. The assumption of considering many PV units is related to the fact that large PV plants are organized in sub-fields each provided with a dedicated converter in order to suitably manage a fixed number of PV strings [92]. Each PV and Storage converter is equipped with a local controller (please note that the structure of the Storage controller is different from the PV ones, as will be clarified later on). In this layout (see Fig. 36) three main MG configurations can be defined for the unit controllers, namely the Normal Operation (NO), Storage Power Priority (PP) and Storage SOC Priority (SP) [93].

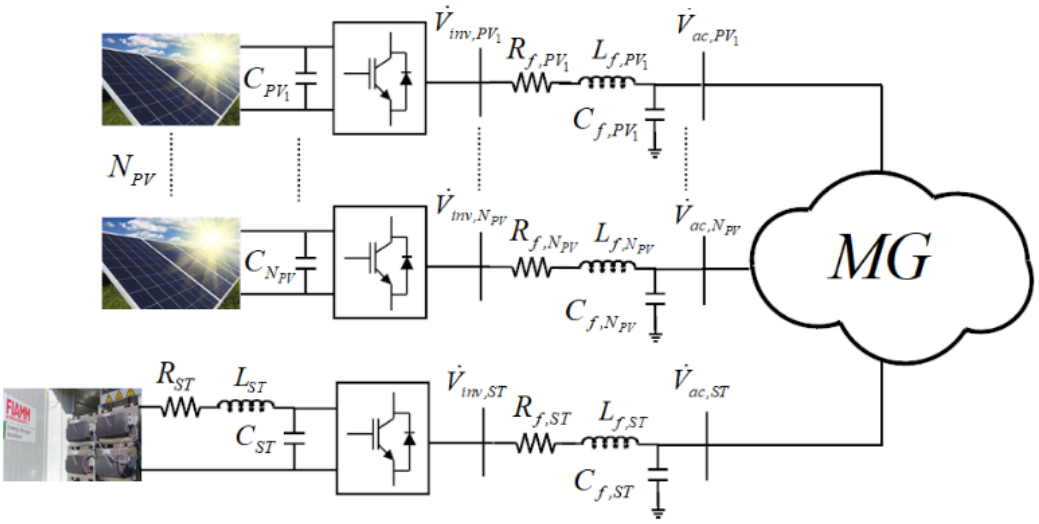

Fig. 36. General PV-Storage MG layout.

The MG NO is when the load request and the PV Maximum Power Point production are not causing any violation of the Storage power and SOC limits. In this configuration, the PV units local controllers make them work at their MPP, while the Storage controller makes it act as an independent voltage source in order to achieve the active and reactive power balance. The PP operation mode corresponds to a condition when the Storage should absorb a power greater than its rating and thus it is necessary to limit its power at the maximum absorption threshold while the PV controllers must curtail their production to satisfy the power balance. Finally, the SP mode is activated when the Storage reaches its maximum SOC; in this case the Storage controller needs to nullify the Storage power absorption and, once again, the PVs must curtail their production to balance the load demand. As a result, the Storage controller accounts for three different operational modes, while the PV controller accounts for only two operational modes since the PV behaviour in PP and SP modes is exactly the same (for this reason in the following this will be labelled as PP_SP for the PV MPC controllers). For the sake of completeness two other scenarios can happen when the load request is greater than the overall PV MPP production and *i*) the Storage is providing its maximum power injection and *ii*) the Storage is totally discharged i.e. the SOC is at its lower limit value. Nevertheless, these two cases can only be managed via Demand Response strategies; for this reason, they are disregarded in the present chapter.

5.3 The MPC Approach

Consider the following time-invariant-affine discrete time system:

$$\boldsymbol{x}_{k+1} = A\boldsymbol{x}_k + B\boldsymbol{u}_k + f \tag{58}$$

where $\boldsymbol{x}_k \in \mathbb{R}^n$ and $\boldsymbol{u}_k \in \mathbb{R}^m$ represent the states and inputs, respectively, at time kT_s, being T_s the sampling time. The MPC regulator acts to control the states of the system to a reference value $\boldsymbol{x}_{ref}$ by computing the solution of the following constrained quadratic-programming problem:

$$\min_{\boldsymbol{U}} \quad \boldsymbol{e}_{k+N}^T Q \boldsymbol{e}_{k+N} + \sum_{i=0}^{N-1} \left\{ \boldsymbol{e}_{k+i|k}^T Q \boldsymbol{e}_{k+i|k} + \boldsymbol{u}_{k+i}^T R \boldsymbol{u}_{k+i} \right\} \tag{59}$$

$$s.t. \quad \boldsymbol{x}_{k+i+1|k} = A\boldsymbol{x}_{k+i|k} + B\boldsymbol{u}_{k+i|k} + f \tag{60}$$

$$H_u \boldsymbol{u}_{k+i} \le K_u, \quad i = 0, \ldots, N-1 \tag{61}$$

$$H_x \boldsymbol{x}_{k+i} \le K_x, \quad i = 0, \ldots, N-1 \tag{62}$$

where $\boldsymbol{e}_k$ is the state vector error, $\boldsymbol{x}_{k+1|k}$ refers to the prediction of the state at time $(k+1)T_s$ calculated at time kT_s and N is the prediction horizon, i.e. the number of samples taken into account in forecast. $\boldsymbol{U}=[\boldsymbol{u}_k^T \ldots \boldsymbol{u}_{k+N-1}^T]^T$ is the vector containing the optimal input vector $\boldsymbol{u}_k$, while $Q=Q^T$, $R=R^T$ are symmetric and positive semi-definite weighting matrices. H_u, K_u, H_x, K_x are the matrices that define the constraints for the controlled system. The MPC controller generates the control action using this strategy: at each step the control solves the optimization problem (59), predicts the evolution of the state variables based on their current values and calculates the optimal input for the system within the control horizon. Then, only the first step $\boldsymbol{u}_k$ is applied to the system while the rest of the solution is just discarded. The process is then repeated: a new prediction of the evolution of the states is calculated based on the measurements of their current value, and another set of optimal control action is produced (Fig. 37).

If the considered model is not linear, at any sampling step kT_s a linearization procedure around x_k is required in order to obtain the system described in (58). More details can be found in [94].

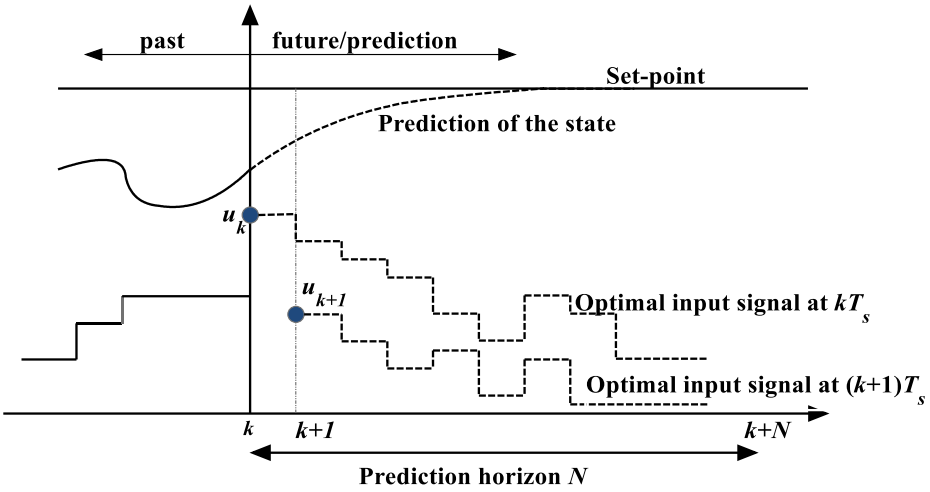

Fig. 37 Receding horizon technique.

For the interested reader more details on the MPC can be found in [94]. Considering the layout of Fig. 36 two types of MPC controllers need to be defined, one for the PV inverters and the other for the Storage inverter. The first step necessary to design the controllers is to define a so-called "auxiliary model", i.e. the one used for the solution of the optimization problem on the prediction horizon. In accordance to the experimental validation of [95] the model used for the controllers design relies on the following assumptions (as described also in chapter 3.4):

- the MG AC section is supposed to be at steady-state;
- inverters are supposed to work in their linear range;
- inverters efficiency is assumed to be unitary;
- higher order harmonics are neglected;
- shunt and resistive component of harmonic filters are neglected.

For the sake of clarity, it is worth pointing out that these assumptions are only made for the controllers design. Simulations provided in Section IV account for a detailed representation of the MG components and infrastructure allowing to test the robustness of the proposed architecture

5.3.1 PV Inverters Controller Design

Considering one of the N_{PV} units connected to the MG as in Fig. 36, the line-to-ground RMS inverter output voltage is:

$$\dot{V}_{inv,PV}(t) = \frac{m_{a,PV}(t)V_{dc,PV}(t)}{2\sqrt{2}} e^{j\theta_{PV}(t)} \tag{63}$$

where $m_{a,PV}$ is the inverter modulation index, $V_{dc,PV}$ is the DC-link voltage and $\theta_{PV}(t)$ is given by:

$$\theta_{PV}(t) = \int_0^t \omega_{PV}(\tau)d\tau + \theta_{PV0} \tag{64}$$

where ω_{PV} is the angular frequency of the PV inverter modulation signals and θ_{PV0} is the PV system initial phase.

The PV voltage at the harmonic-filter output can be written as:

$$\dot{V}_{ac,PV}(t) = V_{ac,PV}(t) e^{j\theta_{f,PV}(t)} \tag{65}$$

where $V_{ac,PV}$ is the line-to-ground voltage at the harmonic-filter output and $\theta_{f,PV}(t)$ is given by:

$$\theta_{f,PV}(t) = \int_0^t \omega_{f,PV}(\tau) d\tau + \varphi_{f,PV}(t) \tag{66}$$

$\omega_{f,PV}$ being the AC-bus angular frequency measured via PLL and $\varphi_{f,PV}(t)$ the phase angle of $V_{ac,PV}$. For the sake of readability, from now on the explicit time dependence will be omitted. Under the active sign convention, the active power flow injected by the PV unit into the MG is given by:

$$P_{ac,PV} = 3\frac{m_{a,PV} V_{dc,PV} V_{ac,PV}}{2\sqrt{2} x_{f,PV}} sin\left(\theta_{PV} - \theta_{f,PV}\right) \tag{67}$$

where $x_{f,PV}$ is the longitudinal reactance of the harmonic-filter calculated at the MG rated angular frequency. Substituting (64) and (66) in (67) one can easily obtain:

$$P_{ac,PV} = \frac{3 m_{a,PV} V_{dc,PV} V_{ac,PV}}{2\sqrt{2} x_{f,PV}} sin\left(\theta_{PV0} - \varphi_{f,PV} + \int_0^t (\omega_{PV} - \omega_{f,PV}) d\tau\right). \tag{68}$$

Let us now define:

$$\sigma_{PV} = \theta_{PV0} - \varphi_{f,PV} \tag{69}$$

and

$$\delta_{PV} = \int_0^t \left(\omega_{PV}(\tau) - \omega_{f,PV}(\tau)\right) d\tau, \tag{70}$$

inserting (69) and (70) into (68) one obtains:

$$P_{ac,PV} = 3\frac{m_{a,PV} V_{dc,PV} V_{ac,PV}}{2\sqrt{2} x_{f,PV}} sin\left(\sigma_{PV} + \delta_{PV}\right). \tag{71}$$

Moreover, the DC-link voltage dynamic is:

$$P_{dc,PV} - P_{ac,PV} = V_{dc,PV} C_{PV} \frac{dV_{dc,PV}}{dt} \tag{72}$$

C_{PV} being the DC-link capacitor and $P_{dc,PV}$ the power coming from the PV unit that depends on the DC voltage $V_{dc,PV}$, the solar irradiance α and the PV cells temperature T, as follows (see [96] for its explicit expression):

$$P_{dc,PV} = I_{dc,PV}\left(V_{dc,PV}, \alpha, T\right) V_{dc,PV}. \tag{73}$$

Substituting (71) and (73) in (72), one has:

$$\begin{cases} \dfrac{dV_{dc,PV}}{dt} = \dfrac{1}{C_{PV}}\left[I_{dc,PV}\left(V_{dc,PV},\alpha,T\right) - \dfrac{3m_{a,PV}V_{ac,PV}}{2\sqrt{2}x_{f,PV}} sin\left(\sigma_{PV}+\delta_{PV}\right) \right] \\ \dfrac{d\delta_{PV}}{dt} = \omega_{PV} - \omega_{f,PV} \end{cases}. \quad (74)$$

System (74) is a non-linear continuous-time system in the form:

$$\dot{\boldsymbol{x}}_{PV} = f(\boldsymbol{x}_{PV}, \boldsymbol{u}_{PV}, \boldsymbol{g}_{PV}) \quad (75)$$

where $\boldsymbol{u}_{PV} = [m_{a,PV} \;\; \omega_{PV}]^T$ is the input vector, $\boldsymbol{x}_{PV} = [V_{dc,PV} \;\; \delta_{PV}]^T$ is the state vector and $\boldsymbol{g}_{PV} = [V_{ac,PV} \; \sigma_{PV} \; \alpha \; T \; \omega_{f,PV}]^T$ is a vector that collects measurements and estimated variables. In particular, $V_{ac,PV}$, α, T and $\omega_{f,PV}$ can be easily measured, while σ_{PV} can be estimated measuring the PV AC side active power and inverting (71) as follows:

$$\sigma_{PV} = sin^{-1}\left(\frac{2\sqrt{2}P_{ac,PV}x_{f,PV}}{3m_{a,PV}V_{dc,PV}V_{ac,PV}} \right) - \int_0^t \left(\omega_{PV}(\tau) - \omega_{f,PV}(\tau) \right) d\tau \;\; . \quad (76)$$

The mathematical model used for prediction by the MPC controller can be put in the classical linear representation as in [94] by linearizing and discretizing (74). From now on, $\boldsymbol{x}_k$, $\boldsymbol{g}_k$ and $\boldsymbol{u}_k$ will indicate states, measurements and inputs, respectively, at time kT_s, being T_s the sampling time. Since the time evolution of measurements is unknown during the prediction, they are supposed to remain constant overall a single prediction horizon and then updated at the following sampling instant, which corresponds to set:

$$\boldsymbol{g}_{PV,k+1} = \boldsymbol{g}_{PV,k} \;\; . \quad (77)$$

Finally, as it is important that the modulation index is constant at steady-state no matter the value it assumes in its operational range, the following state equation can be added:

$$m_{a,PV,k+1} = m_{a,PV,k} + T_s J_{PV,k} \quad (78)$$

that transforms the modulation index in a state considering its derivative J_{PV} as an input, to be regulated to zero. The other input is the PV unit frequency that is regulated to restore the inverter angular frequency (e.g. 314 rad/s in Europe). The resulting PV unit model is:

$$\tilde{\boldsymbol{x}}_{PV,k+1} = A_{PV}\tilde{\boldsymbol{x}}_{PV,k} + B_{PV}\tilde{\boldsymbol{u}}_{PV,k} + h_{PV} \quad (79)$$

where:

$$\tilde{\boldsymbol{x}}_{PV,k} = \begin{bmatrix} \boldsymbol{x}_{PV,k} & \boldsymbol{g}_{PV,k} & m_{a,PV,k} \end{bmatrix}^T \quad (80)$$

$$\tilde{\boldsymbol{u}}_{PV,k} = \begin{bmatrix} \omega_{PV,k} & J_{PV,k} \end{bmatrix}^T \quad (81)$$

A_{PV}, B_{PV} and h_{PV} being suitable matrices coming out from the linearization/discretization processes. Additional constraints included in the PV MPC controller are listed in the following. The PV unit frequency does not have to exceed the minimum limit f_{min} and the maximum limit f_{max}, so:

$$2\pi f_{min} \leq \omega_{PV,k} \leq 2\pi f_{max}\,. \tag{82}$$

The modulation index is constrained in order to guarantee the inverter working in its operational range [97]:

$$m_{a,min} \leq m_{a,PV,k} \leq m_{a,max}\,. \tag{83}$$

Furthermore, regulation of the PV unit reactive power exchange can be performed the reactive power Q_{PV} injected by the PV unit, calculated as:

$$Q_{PV} = 3\left[\frac{m_{a,PV}^2 V_{dc,PV}^2}{8x_{f,PV}} - \frac{m_{a,PV} V_{dc,PV} V_{ac,PV}}{2\sqrt{2}\,x_{f,PV}} cos(\sigma_{PV} + \delta_{PV})\right] \tag{84}$$

can be linearized and discretized to impose the following constraint:

$$-\varepsilon_Q + Q_{PV,ref} \leq Q_{PV,k} \leq Q_{PV,ref} + \varepsilon_Q \tag{85}$$

$Q_{PV,ref}$ being the reactive power reference and ε_Q half the amplitude of the admissible reactive power error. Finally, the inverter capability curve can be linearized and discretized in order to impose:

$$\sqrt{P_{ac,PV,k}^2 + Q_{PV,k}^2} \leq A_{PV} \tag{86}$$

A_{PV} being the inverter rating. The resulting configuration of the PV MPC controller is depicted in Fig. 38 where one can notice that only PV unit local measurements are necessary.

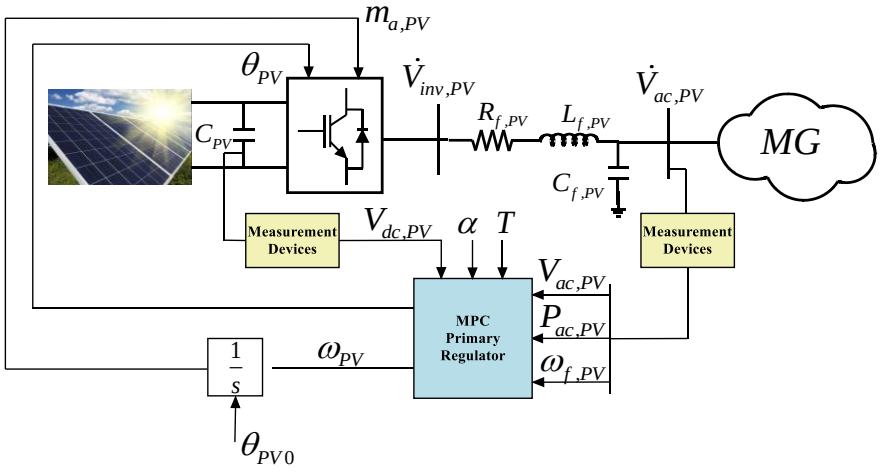

Fig. 38. PV control scheme.

5.3.2 PV Controller – Normal Operation

The goals of PV MPC controller in NO are to regulate the PV DC-link voltage $V_{dc,PV}$ to its MPP value $V_{mpp,PV}$, restoring ω_{PV} to its rated value and bringing J_{PV} to zero accounting for constraints (79), (82), (83), (85) and (86). $V_{mpp,PV}$ is obtained using the open voltage method (see [98]) in order to avoid iterative procedures. Under these considerations the definition of the weighting matrixes for the PV MPC controller in NO are the following:

$$\begin{cases} Q = Q_{PV-NO} = diag(q_{V_{dc}}^{PV}, 0_{1\times 7}) \\ R = R_{PV-NO} = diag(r_{\omega}^{PV}, r_{J}^{PV}) \end{cases} \tag{87}$$

5.3.3 PV Controller – Power Priority and SOC Priority

In PP_SP operation modes the PV unit controller needs to stop following its DC $V_{mpp,PV}$ providing a curtailment of the active power production in order to guarantee the MG power balance. This is done imposing that each PV unit regulates J_{PV} to zero and ω_{PV} to its rated value, accounting for constraints (79), (82), (83), (85) and (86). This leads to the definition of the following control matrixes for the PP_SP operation mode:

$$\begin{cases} Q = Q_{PV-PP\_SP} = diag(0_{1\times 8}) \\ R = R_{PV-PP\_SP} = diag(r_{\omega}^{PV}, r_{J}^{PV}) \end{cases} \tag{88}$$

5.3.4 Storage Inverter MPC Controller Design

The mathematical model used for the design procedure of the Storage MPC controller is the following:

$$\begin{cases} \dfrac{dV_{dc,ST}}{dt} = \dfrac{1}{C_{ST}}\left[I_{dc,ST} - \dfrac{3m_{a,ST}V_{ac,ST}}{2\sqrt{2}x_{f,ST}} sin(\sigma_{ST} + \delta_{ST}) \right] \\ \dfrac{d\delta_{ST}}{dt} = \omega_{ST} - \omega_{f,ST} \\ \dfrac{dI_{dc,ST}}{dt} = \dfrac{E(SOC) - R_{ST}I_{dc,ST} - V_{dc,ST}}{L_{ST}} \\ \dfrac{dSOC}{dt} = -\dfrac{I_{dc,ST}}{NCC} \end{cases} \tag{89}$$

where $I_{dc,ST}$ is the Storage DC-current, E is the Storage internal voltage depending on its *SOC*, R_{ST} and L_{ST} are the Storage internal resistance and inductance respectively and *NCC* is the Nominal Current Capacity. The first two equations of (89) have the same meaning as for the PV MPC controller, the third is the DC R-L circuit dynamics (see Fig. 36) and the fourth is the relationship between the Storage DC current and the SOC (see [71] for details). Following the same procedure used for the definition of the PV MPC controller, linearization and discretization of system (89) produces:

$$\tilde{\boldsymbol{x}}_{ST,k+1} = A_{ST}\tilde{\boldsymbol{x}}_{ST,k} + B_{ST}\tilde{\boldsymbol{u}}_{ST,k} + h_{ST} \tag{90}$$

being:

$$\tilde{\boldsymbol{x}}_{ST,k} = \begin{bmatrix} V_{dc,ST,k} & \delta_{ST,k} & I_{dc,ST,k} & SOC_k & V_{ac,ST,k} & \sigma_{ST,k} & \omega_{f,ST,k} & m_{a,ST,k} \end{bmatrix}^{\mathrm{T}} \tag{91}$$

$$\tilde{\boldsymbol{u}}_{ST,k} = \begin{bmatrix} \omega_{ST,k} & J_{ST,k} \end{bmatrix}^{\mathrm{T}} . \tag{92}$$

The system matrices can be easily obtained as described for the PV unit. The resulting control scheme is reported in Fig. 39 showing that the regulator relies only on local measurements.

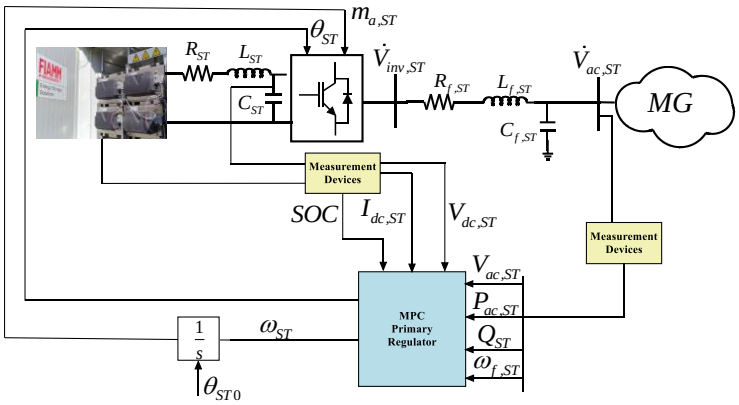

Fig. 39. Storage control scheme.

5.3.5 Storage Controller – Normal Operation

In NO conditions the Storage must act as an independent voltage source. Thus, regulation of the Storage AC side voltage $V_{ac,ST}$ is mandatory. As such voltage is not a state, it is necessary to express it as a function of the Storage states and inputs in order to obtain a linear constraint among them. Using the simplified voltage drop expression, one has:

$$V_{ac,ST} = \frac{m_{a,ST} V_{dc,ST}}{2\sqrt{2}} - \Delta v \tag{93}$$

$$\Delta v = \frac{1}{3V_{ac,ST}} (R_{f,ST} P_{ac,ST} + X_{f,ST} Q_{ST}) \ . \tag{94}$$

So, the constraint for $V_{ac,ST}$ at time sample kT_s is:

$$-\varepsilon_V + V^*_{ac,ST} + \Delta v \le \frac{m_{a,ST,k} V_{DC,ST,k}}{2\sqrt{2}} \le \Delta v + V^*_{ac,ST} + \varepsilon_V \tag{95}$$

where ε_V is half the amplitude of a boundary layer centred in $V^*_{ac,ST}$ where the Storage AC voltage must lay in. As for the other constraints, (95) has to be linearized. Please note that Δv is calculated as in (94) starting from the measurements of voltage and active and reactive power at the beginning of the prediction horizon and then supposed to be constant until the following sampling instant. The capability of the Storage inverter is accounted imposing a constraint as the one in (86). Summarizing, in NO the Storage MPC controller regulates J_{ST} to zero and ω_{ST} to its rated value, accounting for constraints (90) and (95) together with the inverter capability and the limits on the frequency (of the kind (82)) and on the modulation index (of the kind (83)). The NO Storage MPC controller matrixes can be defined as:

$$\begin{cases} Q = Q_{ST-NO} = diag(0_{1\times 8}) \\ R = R_{ST-NO} = diag(r_\omega^{ST}, r_J^{ST}) \end{cases} \tag{96}$$

5.3.6 Storage Controller – Power Priority

In PP mode the Storage MPC controller forces the unit to exchange a fixed power to the grid, namely $P_{ab,lim}$. This is achieved as follows: consider the third of (89) at steady-state and multiply both members by $I_{dc,ST}$. It follows that:

$$E(SOC)I_{dc,ST} - R_{ST}I_{dc,ST}^2 = V_{dc,ST}I_{dc,ST} = P_{ac,ST} = P_{ab,lim} \tag{97}$$

which gives:

$$V_{dc,ST}^2 - E(SOC)V_{dc,ST} - R_{ST}P_{ab,lim} = 0\,. \tag{98}$$

The positive solution $V_{dc,ST}^*$ of (98) is the reference value to which the Storage PP MPC controller regulates the DC link voltage. So, the PP-Storage controller regulates $V_{dc,ST}$ to $V_{dc,ST}^*$, J_{ST} to zero and ω_{ST} to its rated value, accounting for constraints (90) and (95) together with the inverter capability and the limits on the frequency (of the kind (82)) and on the modulation index (of the kind (83)). The Storage control matrixes in PP operational mode can be written as:

$$\begin{cases} Q = Q_{ST-PP} = diag(q_{V_{dc}}^{ST}, 0_{1\times 7}) \\ R = R_{ST-PP} = diag(r_{\omega}^{ST}, r_J^{ST}) \end{cases} \tag{99}$$

5.3.7 Storage Controller – SOC Priority

In case the Storage is absorbing power but its *SOC* becomes greater than a threshold SOC_{lim}, it enters the SP mode in which the MPC controller forces it to nullify its power injection. This is done as in the PP mode with the only difference that in SP model $P_{ab,lim}$ is set to 0. So, the SP mode Storage controller regulates $V_{dc,ST}$ to $V_{dc,ST}^*$, J_{ST} to zero and ω_{ST} to its rated value, accounting for constraints (90) and (95) together with the capability and the limits on the frequency (of the kind (82)) and on the modulation index (of the kind (83)). The Storage control matrixes in SP operational mode can be written as:

$$\begin{cases} Q = Q_{ST-SP} = diag(q_{V_{dc}}^{ST}, 0_{1\times 7}) \\ R = R_{ST-SP} = diag(r_{\omega}^{ST}, r_J^{ST}) \end{cases}. \tag{100}$$

5.3.8 Automatic transition among operating modes

The transition of local unit controllers in accordance to the MG operational modes is easily performed by changing the MPC controllers weighting matrixes *Q* and *R*. The aim of this subsection is to define the conditions for such transition. The Storage MPC controller transition from NO to PP occurs when the Storage is required to absorb a DC power $|P_{dc,ST}|$ greater than a specified threshold $|P_{ab,lim}|$, sufficiently close to its maximum power absorption limit. So, with the adopted sign conventions, the condition for the transition of the Storage controller from the NO to PP is:

$$P_{dc,ST} < P_{ab,lim}\,. \tag{101}$$

Similarly, the Storage MPC controller switches from NO to SP when:

$$SOC > SOC_{lim} \tag{102}$$

SOC_{lim} being a specified threshold lower than 100%.

In both cases, the power injected by the PV units into the MG $P_{ac,PV}$ must decrease to satisfy the active power balance. As a consequence, since the PV controllers haven't produced any variation in the PV power yet, the DC link voltages increase (in accordance to (72)). At this point, each PV controllers try to reduce its local DC link voltage by increasing δ_{PV} (acting on ω_{PV}). The result is an increase of the angular frequency $\omega_{f,PV}$ sensed by the PLL. So, the condition for the PV controller transition from NO to PP_SP is:

$$\omega_{f,PV} > 2\pi f_{curt} \tag{103}$$

$2\pi f_{curt}$ being a specified threshold. The inverse transition (from PP or SP to NO) occurs when the load request increases. In this case, since the PV units must guarantee the active power balance, they need to increase their real power injection. So, the condition for the PV controller transition from PP_SP to NO is:

$$P_{ac,PV} > kP_{PV,MPPT} \quad k \in (0,1) \tag{104}$$

where k is a suitable coefficient to improve the effectiveness of the controller transition.

At the same time, one can observe a decrease in the Storage AC-bus angular frequency $\omega_{f,ST}$ because the PP (or SP) Storage control acts to maintain the voltage set-point calculated from (98), decreasing the modulation angular frequency ω_{ST}. So, the condition for the Storage controller transition back to NO is:

$$\omega_{f,ST} < 2\pi f_{min,NO} \tag{105}$$

$f_{min,NO}$ being another specified threshold.

As a result, one can notice that the proposed controller provides an intrinsic frequency dynamic that allow managing the local unit controller in all the relevant MG operational asset without the need of ICT infrastructure of dedicated element to emulate an inertial frequency response of the system. The logic described can be easily translated into the logic circuits depicted in Fig. 40 and Fig. 41 (one for each type of controller).

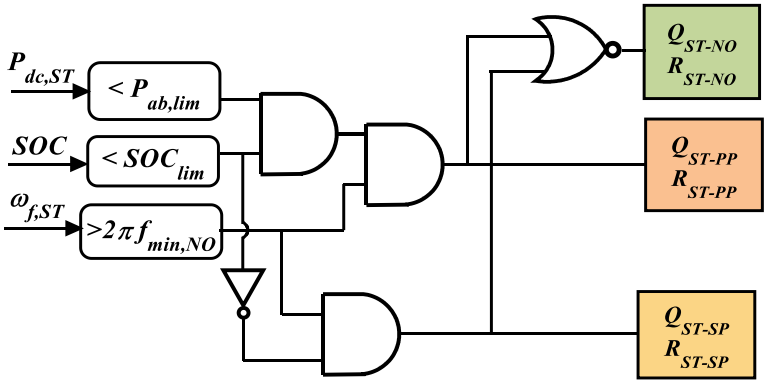

Fig. 40. Storage MPC controller logics transition circuit.

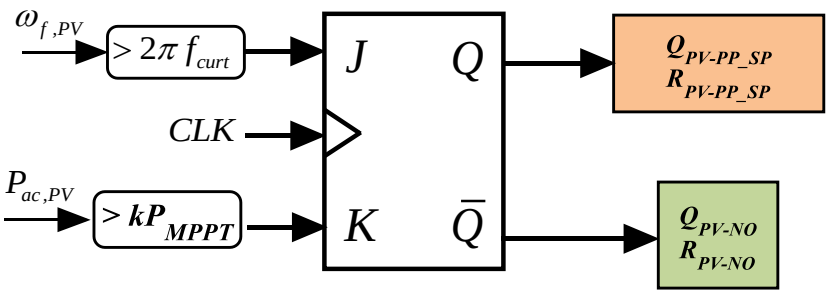

Fig. 41. PV MPC controller logics transition circuit.

5.4 Simulations

The proposed control system has been applied to the microgrid described in [95] and depicted in Fig. 42, consisting of two PV units and one Storage.

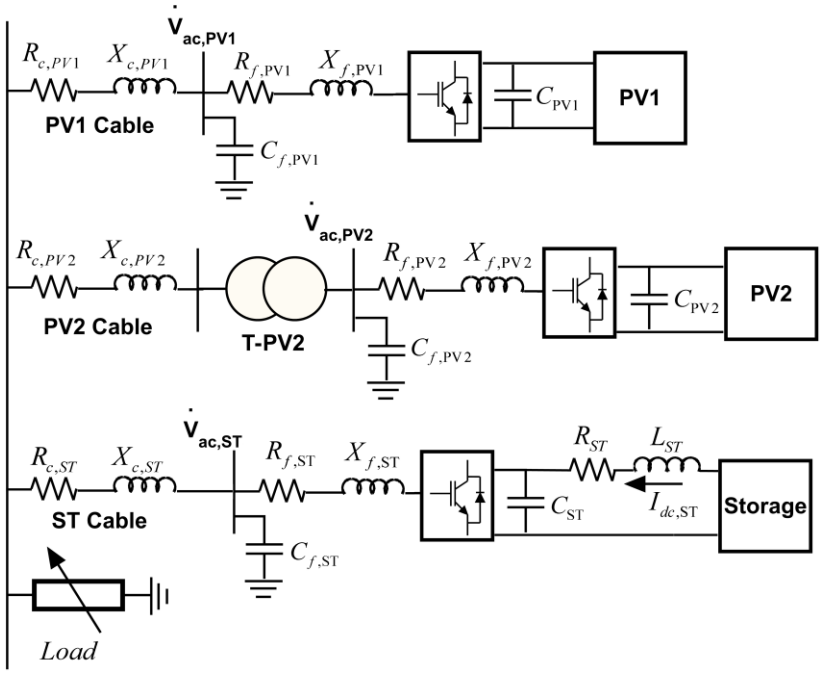

Fig. 42 One line diagram of the test case MG

The peak powers of units PV1 and PV2 are respectively 16 kW and 80 kW while the corresponding inverter ratings are 17 kVA and 85 kVA. Transformer T-PV2 is at unitary transformation ratio. For the Storage the NCC is 228 Ah while power limits are 25 kW (when the Storage is charging) and 60 kW (when the Storage is discharging) and the inverter rating is 62 kVA. A load is connected at the MG main bus.

Simulation are performed in Simulink/Simscape® environment that represents all the MG components and infrastructure with a high level of detail. Inverters are two-level IGBT converters whose models are available in the Simscape library. Moreover, modulation is performed using a PWM technique with a 10 kHz carrier signal. PV units are modelled as suggested in [95], while details on the adopted Storage model can be found in [71]. Cables are modelled by means of resistive-inductive series impedances, while transformers are represented with the only leakage reactance.

Numerical values of the sources and grid parameters appear in Table 22 and Table 23 respectively.

Table 14 – Sources parameters

Parameter	***Value***	***Parameter***	***Value***	***Parameter***	***Value***
C_{PV}	3.3 mF	R_{ST}	1.12 Ω	C_{PV2}	6.0 mF
$R_{f,PV1}$	3.14 mΩ	L_{ST}	1 mH	$R_{f,PV2}$	1.05 mΩ
$L_{f,PV1}$	1 mH	$R_{f,ST}$	3.14 mΩ	$L_{f,PV2}$	0.3 mH
$C_{f,PV1}$	10 μF	$L_{f,ST}$	1 mH	$C_{f,PV2}$	5 μF
C_{ST}	3.5 mF	$C_{f,ST}$	10 μF	-	-

Table 15 – Grid Parameters

Parameter	***Value***	***Parameter***	***Value***
T-PV2 $v_{cc\%}$	8 %	T-PV2 A_n	85 kVA
$R_{c,PV1}$	0.15 Ω	$X_{c,PV1}$	1.03 Ω
$R_{c,PV2}$	0.04 Ω	$X_{c,PV2}$	0.16 Ω
$R_{c,ST}$	0.04 Ω	$X_{c,ST}$	0.01 Ω

In the following, three different simulations are proposed, all starting from the initial working point specified by the load flow assignments reported in Table 16. Finally, all regulators parameters are reported in Table 17 and Table 18.

The performances of the proposed MPC approach are compared with the ones of a traditional control architecture for an islanded PV-Storage MG [79]. In this traditional architecture the Storage inverter is controlled in the so-called grid forming configuration, i.e. controlling its AC terminal voltage and frequency with two voltage and current axis nested loops (see Fig. 2 of [79] for more details) while PV inverters are controlled in grid feeding configuration providing active power according to the MPPT and reactive power in accordance to the specific external reference (see Fig. 3 of [79] for details).

Table 16 – Load flow assignments

	PV1 (PQ bus)	***PV2 (PQ bus)***	***Storage (Slack bus)***	***Load (PQ bus)***
Active power	16 kW	80 kW	-	80 kV
Reactive power	0 kVAr	0 kVAr	-	15 kVAr
Voltage	-	-	230 V	-

Table 17– PV controller parameters

f_{min}/f_{max}	49.5/50.5 Hz	ε_Q	1 kVAr	r_{ω}^{PV}	700
$\boldsymbol{m_{a,min}}$	0.5	f_{curt}	50.3 Hz	r_J^{PV}	200
$\boldsymbol{m_{a,max}}$	1.05	k	0.9	$q_{V_{dc}}^{PV}$	60

Table 18– Storage controller parameters

f_{min}/f_{max}	49.5/50.5 Hz	ε_V	11.5 V (5%)	$q^{ST}_{V_{dc}}$	10
$m_{a,min}$	0.5	$P_{ab,lim}$	-20 kW (PP)	r^{ST}_J	30
$m_{a,max}$	1.05		0 kW (SP)	r^{ST}_ω	10
$f_{min,NO}$	49.8 Hz	SOC_{lim}	90.0%	-	-

5.4.1 Simulation A – Load and irradiance variation in NO

The aim of this simulation is to show the performances of the NO controllers in case of two contingencies: *i)* a load decreases at 0.2 s from 80 kW to 70 kW and *ii)* a solar irradiance decreasing ramp starting at 0.6 s from its initial value of 1 kW/m^2 and reaching 0.7 kW/m^2 at 0.8 s. Fig. 43 shows the sources and load active power flows while Fig. 44 presents the three sources AC voltages (the proposed MPC control profiles are represented in solid lines while traditional control ones in dashed lines).

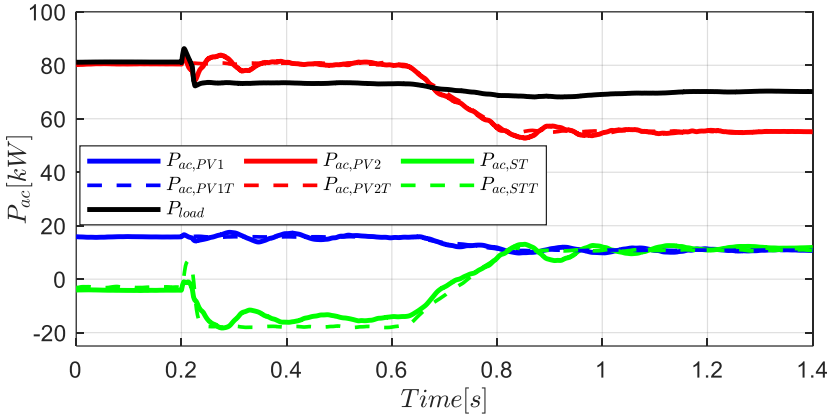

Fig. 43. Active powers time profiles.

As one can see, there is no remarkable differences between the two methods: in both cases, the Storage keeps the voltage within the admissible range (230±5% V, dash-dotted black lines) and maintains the power balance after both contingencies. Fig. 45 represents the frequencies that are restored to the desired value of 50 Hz at the end of the transient.

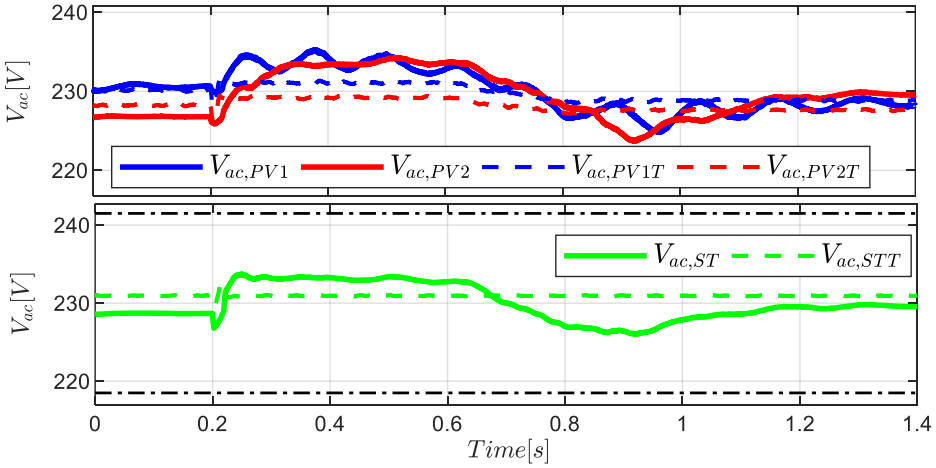

Fig. 44. RMS phase-to-ground voltage time profiles.

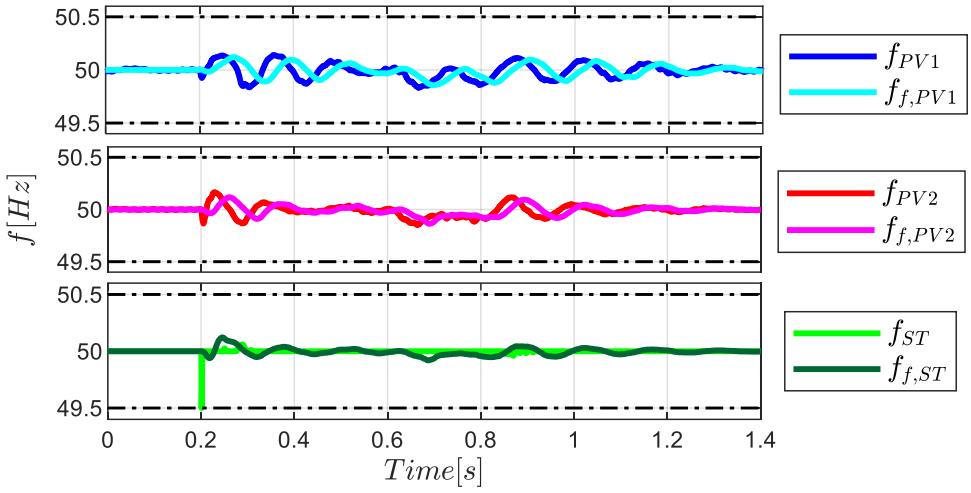

Fig. 45. Frequency time profiles.

5.4.2 Simulation B – Load decrease causing PP operation

The aim of this simulation is to test the performances of the controllers in the PP mode. This is done by imposing a load decreases to 25 kW at 0.2 s which causes the Storage absorption to exceed the 20 kW limit and thus requiring operating in PP mode. Following, at 0.6 s the load is increased in order to restore a NO condition and allowing to verify a proper transition both in and out PP mode.

The MPC control transition between NO and PP modes logic is triggered for the Storage when active power hits his limit. As far as the PV units are concerned, when their frequencies $\omega_{f,PV1}$ and $\omega_{f,PV2}$ exceed the value $2\pi f_{curt}$ (see Fig. 46), the control transition between NO and PP modes logic is triggered and the PV units are forced to curtail their production.

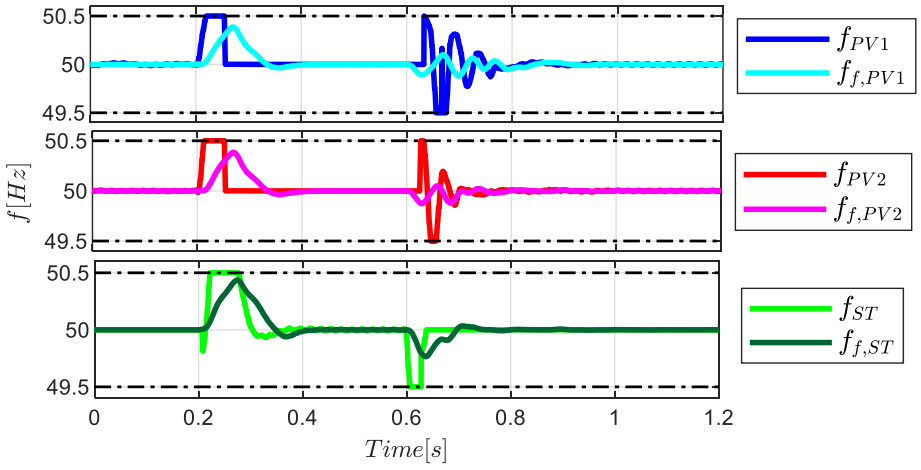

Fig. 46. Frequency time profiles.

Fig. 47 highlights that the Storage MPC controller can regulate the voltage at its terminals even in the transition to and during the PP mode. On the other hand, in Fig. 48 one can see what happens if the traditional approach is not equipped with a suitable communication system. The two PV units are not curtailed, resulting in a sudden increase of the AC bus voltages that cause the overvoltage protection tripping, according to the main standards [99].

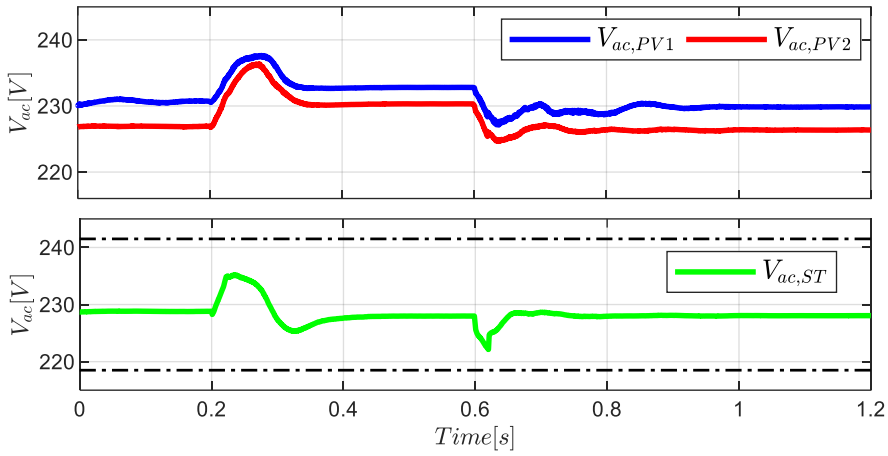

Fig. 47. RMS values of phase to ground voltages.

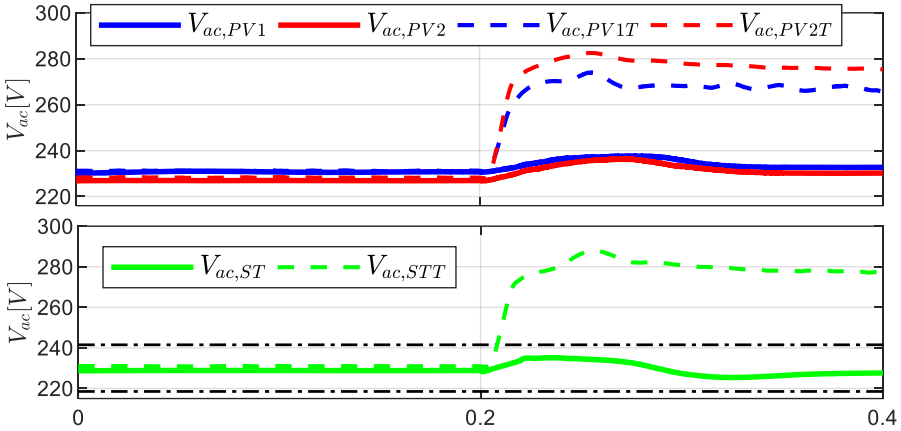

Fig. 48. RMS values of phase to ground voltages: comparison with the traditional approach

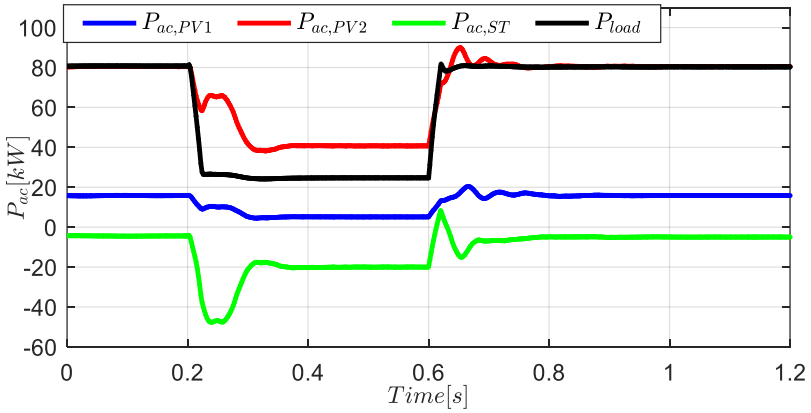

Fig. 49. Active powers time profiles.

When the load increases one can see that the MPC controllers restores the NO mode according to the rules defined in §5.4; i.e. for the PV units when their active power become greater than the value $kP_{PV,MPPT}$, (see Fig. 49) and for the Storage when $\omega_{f,ST}$ becomes lower than $2\pi f_{min,NO}$ (see Fig. 46). Fig. 50 shows the DC link voltages of the three sources highlighting that that the first transition needs about 0.1 seconds, while the NO restoration occurs in about 0.2 seconds.

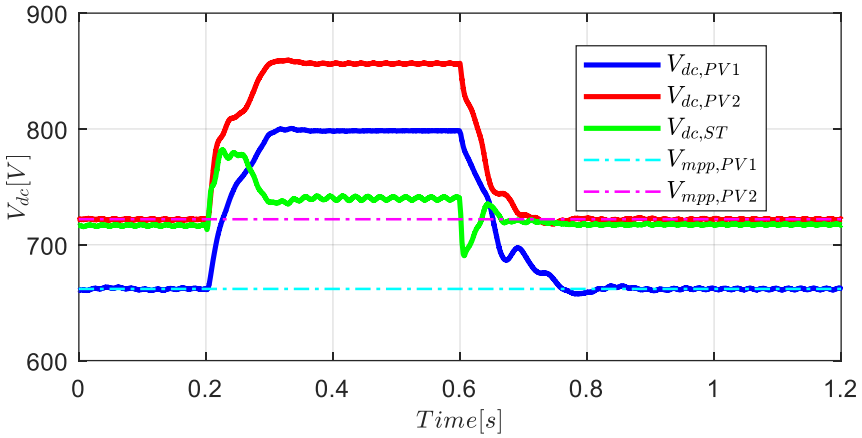

Fig. 50. DC-link voltage time profiles.

5.4.3 Simulation C – Load decrease causing SP operation

The aim of this third simulation is to show the performance of the proposed control strategy in the SP mode. To better highlight this, the *SOC* is initialized very close to SOC_{lim}. Moreover, the load power request decreases from 80 to 40 kW at 0.2 s as shown in Fig. 51. This first variation implies the transition to the PP mode since SP mode occurrence probability increases if the Storage absorbs its maximum power (see Fig. 52 for the PV transition and Fig. 51 for the Storage one).

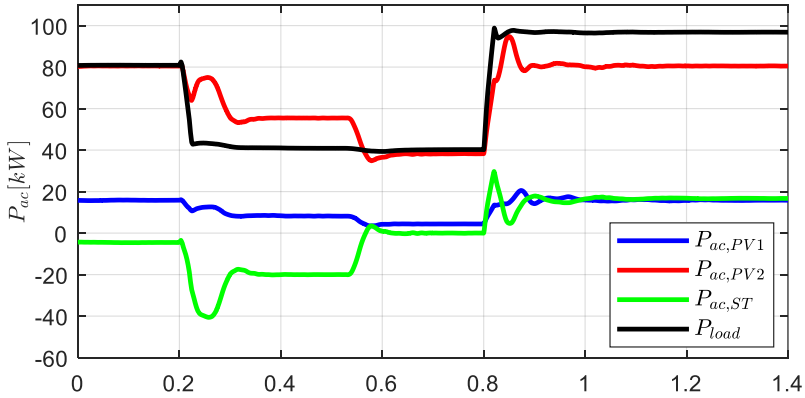

Fig. 51. Active powers time profiles.

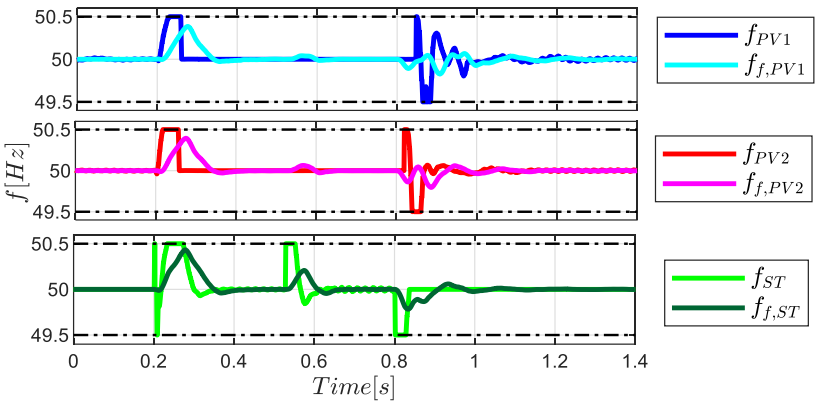

Fig. 52. Frequency time profiles.

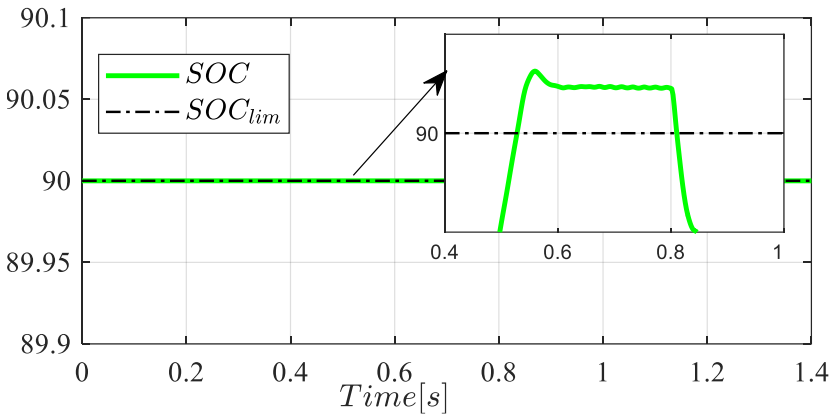

Fig. 53. Storage SOC time profile.

At about 0.55 s the Storage reaches its SOC_{lim} (see the detail in Fig. 53), which triggers the transition to SP mode. At 0.8 s the load request increases to 100 kW, which determines the restoration of the NO mode in which the PV units are set back to their MPP (Fig. 54) while the Storage injects about 18 kW in order to guarantee the MG active power balance (Fig. 51). Finally, Fig. 55 shows again the effectiveness of the Storage controller in regulating the voltage and Fig. 52 highlights that frequencies are restored in less than 0.2 seconds. In this case, no comparison is presented with the traditional approach for the sake of readability since this would result in the same overvoltage behaviour seen in the previous case.

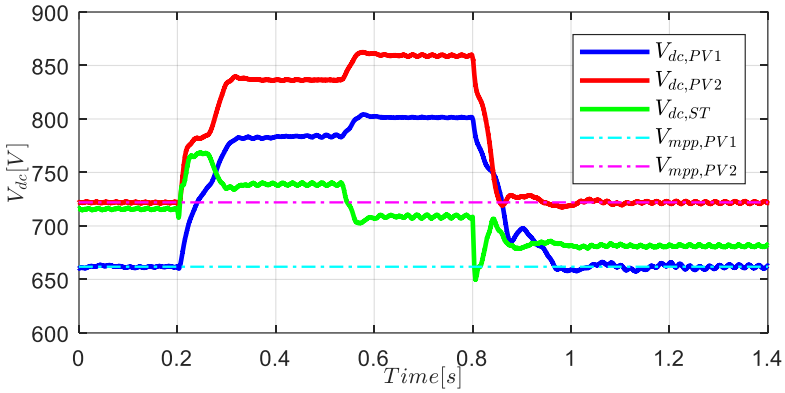

Fig. 54. DC-link voltage time profiles.

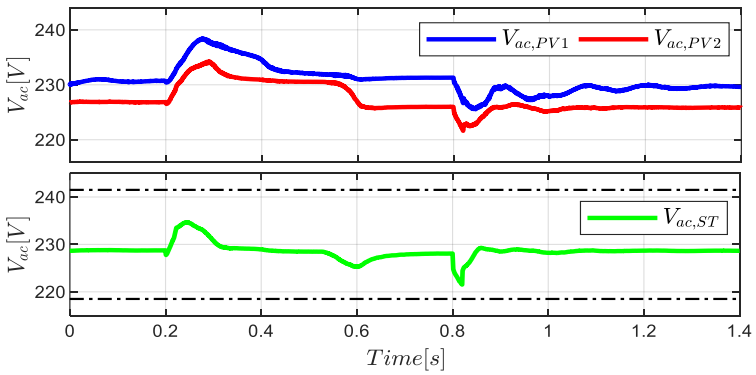

Fig. 55. RMS values of phase to ground voltages.

5.5 MPC Experimental Test

This section investigates the feasibility of this control for grid forming inverter in a MG environment. The MPC strategy allows to open new scenarios in grid-forming research, due to the possibility to address in very explicit way the goal. MPC strategy is deeply described and strongly addressed to the actual implementation. In test configuration, realizing a fast prototyping approach, dSPACE software and hardware were used to perform the experimental validation of the proposed method.

According [100-102] inverters that connect Distributed Energy Resources (DERs) to MGs can be classified according one of the three following operation way: Grid-feeding, Grid-forming and Grid-supporting power converters [100, 101].

The grid-feeding power converters are designed to supply a specified value of active and reactive power, nothing more. This operation mode brings to assimilate the controlled source as an ideal current source connected to the grid in parallel with high impedance. The grid-forming converters can be represented as an ideal ac voltage source with a low impedance in series, defining the frequency of the MG and the voltage amplitude at its bar.

Finally, grid-supporting converters can be seen either as current or voltage sources in which the current (voltage) is selected according specified control laws (e.g. droop characteristic [23], V/Q control curves [103, 104], P/Q characteristic [103, 104] and so on). In Fig. 56 these operation modes are represented.

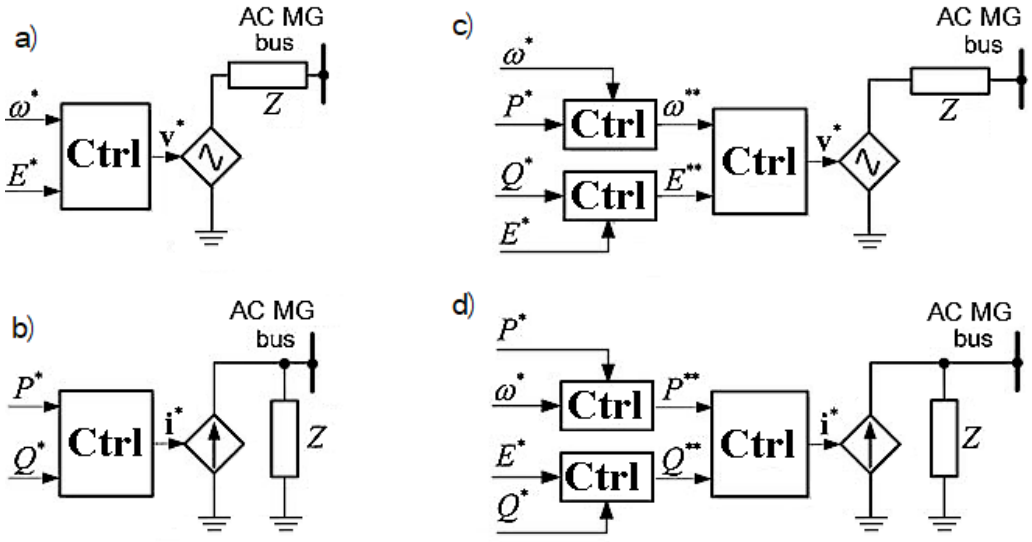

Fig. 56 Elementary scheme for a) grid forming; b) grid feeding; c) grid supporting acting as voltage source; d) grid supporting acting as current source.

The basic control scheme for grid-forming converter can be found in Fig. 57. It is composed by two very common internal loops) regulated by proportional-integrator controllers [105]. In the proposed control scheme, the amplitude of the voltage at the PCC and current are measured and transformed to dc values in the dq frame by

applying the Park transformation and compared to reference values as shown in Fig. 57. All the nomenclature is available in [105].

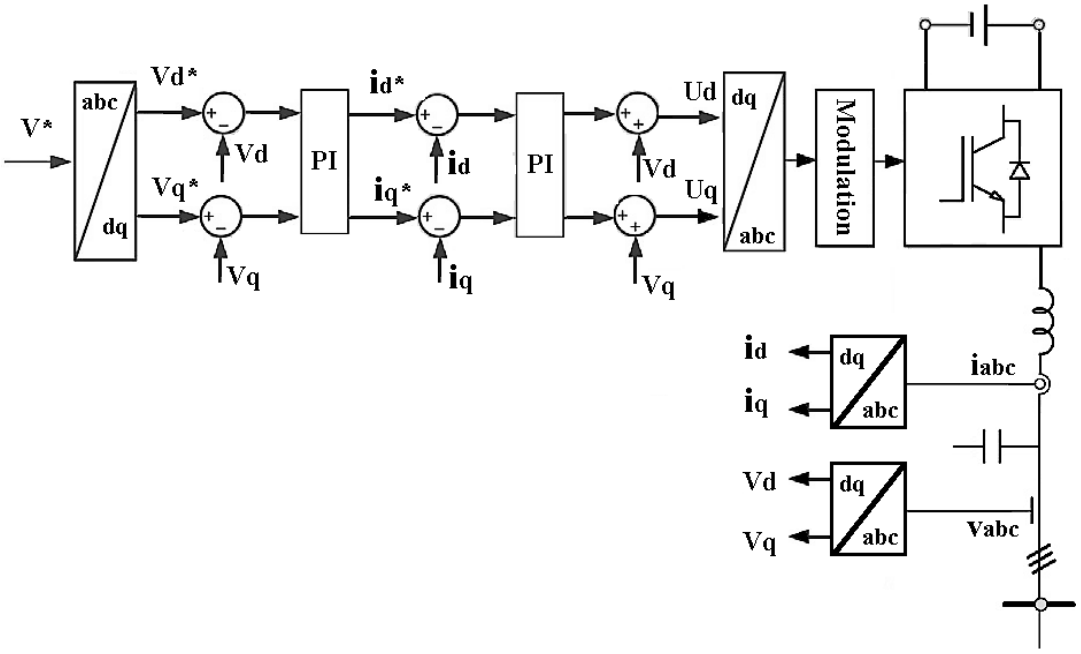

Fig. 57 Grid-forming base control scheme [105]

5.5.1 The grid forming control

Let's consider a generic DG as depicted in Fig. 58. It consists of a DC source, a DC link, a full IGBT bridge, an AC filter and finally PCC.

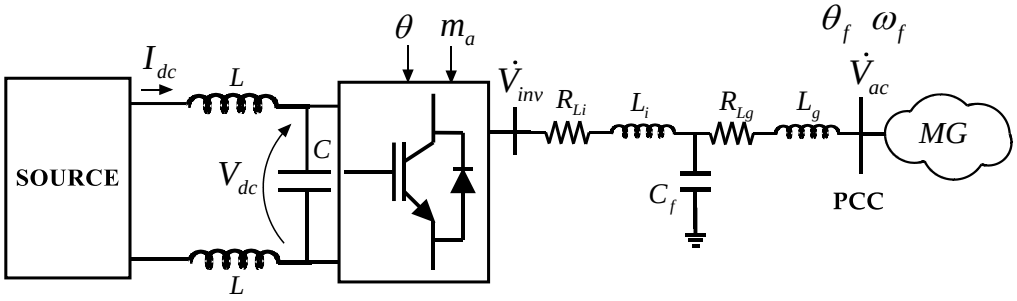

Fig. 58 General layout of a DG.

In order to perform the design procedure for the MPC for grid forming, it is necessary to derive a mathematical model for the controlled system. Such model is here proposed according to the assumptions [71, 95] described in §3.4 and §5.3.

The resulting model, represented in Fig. 59, has been extensively validated with experimental measurements, as detailed in [95].

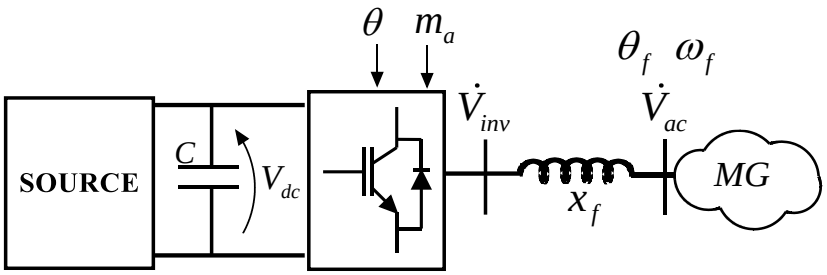

Fig. 59 System model for the MPC controller design

Moreover, it is important to highlight that the proposed MPC controllers do not require information about MG topology and parameters, just because they are proposed in a decentralized formulation. This makes this strategy not sensitive to MG topology variations.

The phasor of the line-to-ground voltages at the inverter output and at the harmonic-filter output can be respectively written as:

$$\dot{V}_{inv}(t) = \frac{m_a(t)V_{dc}(t)}{2\sqrt{2}} e^{j\theta(t)} \tag{106}$$

$$\dot{V}_{ac}(t) = V_{ac}(t) e^{j\theta_f(t)} \tag{107}$$

where m_a is the inverter modulation index, V_{dc} is the DC-link voltage and V_{ac} is the line-to-ground voltage at the harmonic-filter output. The phase angles can be written as follows:

$$\theta(t) = \int_0^t \omega(\tau)\, d\tau + \theta_0 \tag{108}$$

$$\theta_f(t) = \int_0^t \omega_f(\tau)\, d\tau + \varphi_f(t) \tag{109}$$

where ω is the angular frequency of the inverter modulation signals and ω_f is the AC bus frequency measured via PLL (in the following equations the explicit time dependence will be omitted for notation simplification). The active power flow P_{ac} injected by the unit into the MG is given by:

$$P_{ac} = 3\frac{m_a V_{dc} V_{ac}}{2\sqrt{2}\, x_f} \sin(\theta - \theta_f) \tag{110}$$

where x_f is the longitudinal reactance of the harmonic-filter. Obviously if the ac filter is composed by a LCL configuration, x_f represents the sum of the two reactances in series according to the former hypotesis.

Substituting (108) and (109) in (110) one gets:

$$P_{ac} = \frac{3m_a V_{dc} V_{ac}}{2\sqrt{2}\, x_f} \sin\left(\theta_0 - \varphi_f + \int_0^t (\omega(\tau) - \omega_f(\tau))\, d\tau\right) \tag{111}$$

Defining:

$$\sigma = \theta_0 - \varphi_f \tag{112}$$

and

$$\delta = \int_0^t \left(\omega(\tau) - \omega_f(\tau)\right) d\tau \tag{113}$$

equation (111) can be rewritten as:

$$P_{ac} = 3\frac{m_a V_{dc} V_{ac}}{2\sqrt{2}\, x_f} sin\left(\sigma + \delta\right) \tag{114}$$

Considering now the differential equation that describes the DC-link voltage dynamics, it follows that:

$$P_{dc} - P_{ac} = V_{dc} C \frac{dV_{dc}}{dt} \tag{115}$$

where C is the dc-link capacitor and P_{dc} is the power coming from the DC source that can be written as:

$$P_{dc} = I_{dc}\left(V_{dc}\right) V_{dc} \tag{116}$$

where I_{dc} is a given function of V_{dc} depending on the specific nature of the source.

Substituting (114) and (115) in (116) it is possible to write the dynamic system of the DG:

$$\begin{cases} \dfrac{dV_{dc}}{dt} = \dfrac{1}{C}\left[I_{dc}(V_{dc}) - \dfrac{3 m_a V_{ac}}{2\sqrt{2}\, x_f} sin(\sigma + \delta) \right] \\ \dfrac{d\delta}{dt} = \omega - \omega_f \end{cases} \tag{117}$$

System(117) is a non-linear continuous -time system in the form:

$$\dot{\boldsymbol{x}} = f(\boldsymbol{x}, \boldsymbol{u}, \boldsymbol{g}) \tag{118}$$

where $\boldsymbol{u}=[m_a \ \omega]^T$ is the input vector that has to be provided by the controller, $\boldsymbol{x}=[V_{dc} \ \delta]^T$ is the state vector and $\boldsymbol{g}=[V_{ac} \ \sigma \ \omega_f]^T$ is a vector that collects measurements and estimated variables. In particular, V_{ac} and ω_f can be easily measured, while σ can be estimated as follows:

$$\sigma = sin^{-1}\left(\frac{2\sqrt{2} P_{ac} x_f}{3 m_a V_{dc} V_{ac}} \right) - \int_0^t \left(\omega(\tau) - \omega_f(\tau)\right) d\tau \tag{119}$$

As specified before, the mathematical model for the prediction in MPC controllers (58) can be obtained at any time t^* linearizing (117) around $x(t^*)$. Performing the linearization procedure, (117) becomes:

$$\dot{\boldsymbol{x}} = A^* \boldsymbol{x} + B^* \boldsymbol{u} + G^* \boldsymbol{g} + D^* \tag{120}$$

where the system matrices are reported below.

$$A^* = \begin{bmatrix} \frac{1}{C}\frac{dI_{dc}}{dV_{dc}}\Big|_{V_{dc}(t^*)} & -\frac{3m_a V_{ac}}{2\sqrt{2}x_f C}\cos\left(\sigma(t^*)+\delta(t^*)\right) \\ 0 & 0 \end{bmatrix} \tag{121}$$

$$B^* = \begin{bmatrix} -\frac{3V_{ac}(t^*)}{2\sqrt{2}x_f C}\sin\left(\sigma(t^*)+\delta(t^*)\right) & 0 \\ 0 & 1 \end{bmatrix} \tag{122}$$

$$G^* = \begin{bmatrix} -\frac{3m_a(t^*)}{2\sqrt{2}x_f C}\sin\left(\sigma(t^*)+\delta(t^*)\right) & -\frac{3m_a(t^*)}{2\sqrt{2}x_f C}\cos\left(\sigma(t^*)+\delta(t^*)\right) & 0 \\ 0 & 0 & -1 \end{bmatrix} \tag{123}$$

$$D^* = \begin{bmatrix} \frac{3m_a(t^*)V_{ac}(t^*)}{2\sqrt{2}x_f C}\left(\sin\left(\sigma(t^*)+\delta(t^*)\right)+\left(\sigma(t^*)+\delta(t^*)\right)\cos\left(\sigma(t^*)+\delta(t^*)\right)\right)+\frac{1}{C}V_{dc}(t^*)\frac{dI_{dc}}{dV_{dc}}\Big|_{V_{dc}(t^*)} \\ 0 \end{bmatrix} \tag{124}$$

Then, due to the fact MPC control works in the discrete-time domain, (120) needs to be discretized as follows:

$$\boldsymbol{x}_{k+1} = \left(I + T_s A^*\right)\boldsymbol{x}_k + T_s B^* \boldsymbol{u}_k + T_s G^* \boldsymbol{g}_k + T_s D^* \tag{125}$$

where the subscript k denotes the system variables discretized at the sampling time kT_s. Since during the prediction the time evolution of the measurements is unknown, they are supposed to remain constant during the prediction horizon N, i.e. $\boldsymbol{g}_k$ is considered as a state with no dynamics as described by the following equation:

$$\boldsymbol{g}_{k+1} = \boldsymbol{g}_k \tag{126}$$

Furthermore, as what matters for the modulating index is that at steady state it becomes constant no matter its value in the linear range (0,1) instead of considering m_a as a control variable for the system, its derivative J is taken as an input. So, a new dynamic equation $m_{a,k+1} = m_{a,k} + T_s J_K$ is added to (125). The resulting general DG model of the kind (58) necessary for the prediction computed by the controller is:

$$\tilde{\boldsymbol{x}}_{k+1} = A^*_{dm}\tilde{\boldsymbol{x}}_k + B^*_{dm}\tilde{\boldsymbol{u}}_k + f^*_{dm} \tag{127}$$

where:

$$\tilde{\boldsymbol{x}}_k = \begin{bmatrix} \boldsymbol{x}_k & \boldsymbol{g}_k & m_{a,k} \end{bmatrix}^{\mathrm{T}} \tag{128}$$

$$\tilde{\boldsymbol{u}}_k = \begin{bmatrix} \omega_k & J_k \end{bmatrix}^T \tag{129}$$

$$A_{dm}^{*}=\begin{bmatrix} I_2+T_sA^{*} & T_sG^{*} & T_sB^{*}(1) \\ 0_{3\times2} & I_3 & 0_{3\times1} \\ 0_{1\times2} & 0_{1\times3} & 1 \end{bmatrix}=\begin{bmatrix} I_2+T_sA^{*} & T_sG^{*} & -\dfrac{T_s3V_{ac}(t^{*})}{2\sqrt{2}x_fC}sin\left(\sigma(t^{*})+\delta(t^{*})\right) \\ 0_{3\times2} & I_3 & 0_{4\times1} \\ 0_{1\times2} & 0_{1\times3} & 1 \end{bmatrix} \tag{130}$$

$$B_{dm}^{*}=\begin{bmatrix} T_sB^{*}(2) & 0_{5\times1} \\ 0_{4\times1} & T_s \end{bmatrix}=\begin{bmatrix} 0 & 0 \\ T_s & 0_{4\times1} \\ 0_{4\times1} & T_s \end{bmatrix} \qquad f_{dm}^{*}=\begin{bmatrix} T_sD^{*} \\ 0_{4\times1} \end{bmatrix} \tag{131}$$

in which $T_sB^{*}(1)$ and $T_sB^{*}(2)$ are the first and the second column of the matrix T_sB^{*} respectively.

Moreover, some relevant constraints (see (61) and (62)) are implemented. The angular frequency for the inverter modulation signals ω acts on the system to satisfy the control objectives within the operational limits to achieve MG power quality:

$$2\pi f_{min}\le\omega\le2\pi f_{max} \tag{132}$$

The modulation index is constrained as follows to guarantee the inverter working in its linear operational range:

$$m_{a,min}\le m_a\le m_{a,max} \tag{133}$$

To ensure that even during a transient the inverter capability curve is never exceeded the following constraint, after a linearization procedure, is implemented:

$$\sqrt{P_{ac}^2+Q_{ac}^2}\le A_{max} \tag{134}$$

where Q_{ac} can be expressed as combination of state and input as follows

$$Q_{ac}=3\left[\frac{m_a^2V_{dc}^2}{8x_f}-\frac{m_aV_{dc}V_{ac}}{2\sqrt{2}x_f}cos\left(\sigma+\delta\right)\right] \tag{135}$$

As specified before, grid-forming inverters must regulate their AC terminal voltage. In the proposed approach, the aforementioned goal is obtained expressing the desired voltage in terms of states and inputs of the controlled system and using the simplified voltage drop expression:

$$\begin{gathered} V_{ac}=\frac{m_aV_{dc}}{2\sqrt{2}}-\Delta v \\ \Delta v\approx\frac{1}{3V_{inv}}(R_fP_{ac}+x_fQ_{ac})\approx\frac{1}{3V_{ac}}(R_fP_{ac}+x_fQ_{ac})\approx\frac{1}{3\dfrac{m_aV_{dc}}{2\sqrt{2}}}(R_fP_{ac}+x_fQ_{ac}) \end{gathered} \tag{136}$$

One can combine (136), (135), (114) and (106) in order to obtain the V_{ac} formulation composed by just states, inputs and constants:

$$V_{ac} = \frac{m_a V_{dc}}{2\sqrt{2}} \left[-\frac{R_f}{x_f} \sin(\sigma + \delta) + \cos(\sigma + \delta) \right] \quad (137)$$

Let's define $e=V_{ac}-V_{ac,ref}$ and $\tilde{\boldsymbol{u}}_{\boldsymbol{ref}} = [\omega_n \; 0]^T$. These definitions are essential in order to make MPC act properly, indeed the minimization is expected to reduce the distance to some reference. ω_n is the rated frequency of the MG, $V_{ac,ref}$ is the reference for V_{ac} and the zero of $\tilde{\boldsymbol{u}}_{\boldsymbol{ref}}$ represents the desired J, i.e. null that means m_a is constant.

Now it is time to set the MPC goal, i.e. solving the following equation:

$$\min_{\breve{U}} \quad e_{k+N}^T Q_V e_{k+N} + \sum_{i=0}^{N-1} \left\{ e_{k+i|k}^T Q_V e_{k+i|k} + \breve{\boldsymbol{u}}_{k+i}^T R \breve{\boldsymbol{u}}_{k+i} \right\} \quad (138)$$

in which $\breve{\boldsymbol{U}}=[\breve{\boldsymbol{u}}_k^T \ldots \breve{\boldsymbol{u}}_{k+N-1}^T]^T$ is the vector containing the optimal input vector $\breve{\boldsymbol{u}} = \tilde{\boldsymbol{u}} - \tilde{\boldsymbol{u}}_{\boldsymbol{ref}}$. R=diag(R_ω; R_J), where R_ω and R_J represent the weight for the input, and Q_V is the weight for the voltage error.

Finally, the control scheme is reported in Fig. 60. MPC regulator needs the measurement of voltage, active power and the angular frequency at the inverter AC side and of the DC-link voltage from the inverter DC side. Then, the online optimization process is performed to generate the control signals for the inverter PWM modulation.

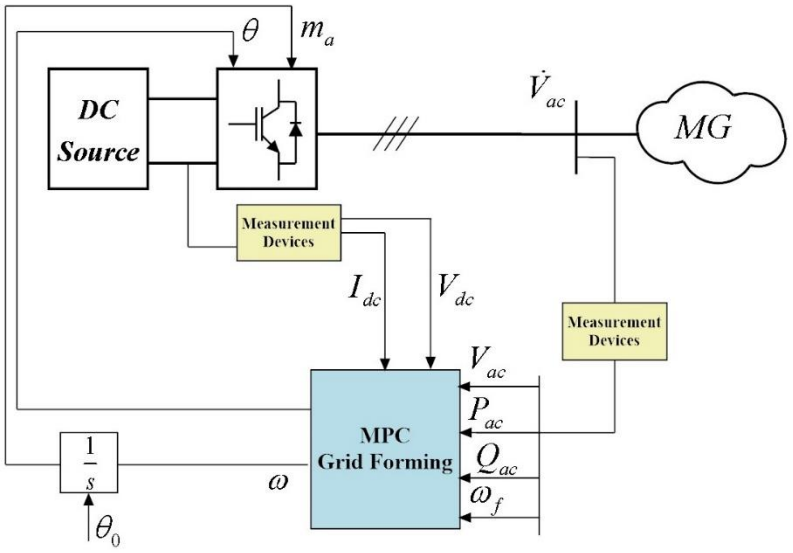

Fig. 60 Control scheme overview

5.5.2 Experimental Setup

The power system setup is depicted in Fig. 61.

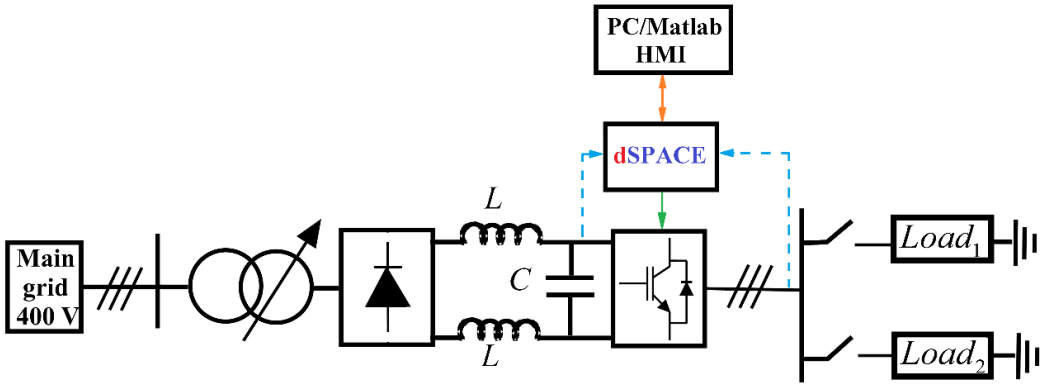

Fig. 61 Test system overview, (AC LCL filter is omitted for sake of compactness).

It consists of the main grid (400 V) that supplies a power train composed by variable-ratio autotransformer, diode bridge rectifier, DC link, inverter and passive loads. The main grid data and parameters as in Fig. 58 can be found in Table 19.

In Fig. 62 it is possible to see some details of the experimental setup.

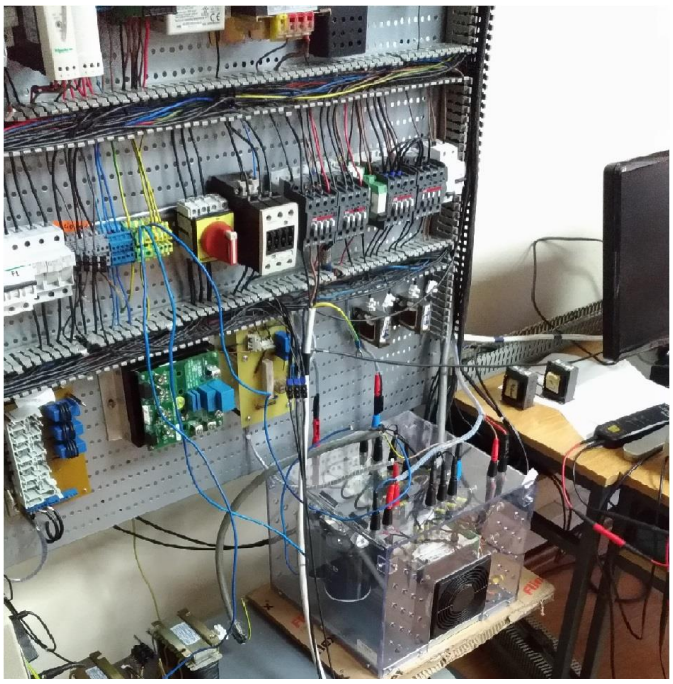

Fig. 62 Experimental set up detail at Niš University

Table 19. Power system variables.

DC link		**Autotransformer**		**AC filter**	
C	1.1 mF	Transf. size	7.6 kVA	L_i	28 mH
L	2.35 mH	Transf. ratio	400/223 V	R_{Li}	0.17 Ω
		$V_{cc\%}$	4.7%	L_g	1.3 mH
				R_{Lg}	11 mΩ
				C_f	3.3 µF

Two different constant resistive loads are at disposal: i.e. $Load_1$ and $Load_2$ with a resistance of 66 Ω and 160 Ω respectively. The inverter is a Danfoss FC 302, 8.2A, controlled by dSPACE 1103, whose board was used to collect the measuring signals and to drive the inverter. More details are available in [106]. The control algorithm is developed in MATLAB/Simulink. The QP was solved using qpOASES [107, 108], an open source library for C++ which proposes some simplified tools for this kind of interfaces in which more than one software is involved.

In Table 20 it is possible to find the control variables used in the experimental test described in the following section.

Table 20. Control variables.

MPC parameter				**Other numerical data**	
Q_V	3	f_{min}	49.5 Hz	A_{max}	4 kVA
R_ω	10	f_{max}	50.5 Hz	ω_n	314.159 rad/s
R_J	5	$m_{a,min}$	0.18		
N	3	$m_{a,max}$	1.156		

Examining (73), it is apparent that a relationship between voltage and current of the DC source is required. Thus, before proceeding with the MPC controller design and implementation, a simple experimental campaign is to be set up to define the V/I characteristic of the available source (main grid, autotransformer- diode bridge – DC link). More details about the procedure are available on the appendix.

For the specific powertrain, the obtained characteristic is shown in Fig. 63, in which the blue stars represent the discrete experimental characteristic and the red line represents the best 5th order polynomial interpolation.

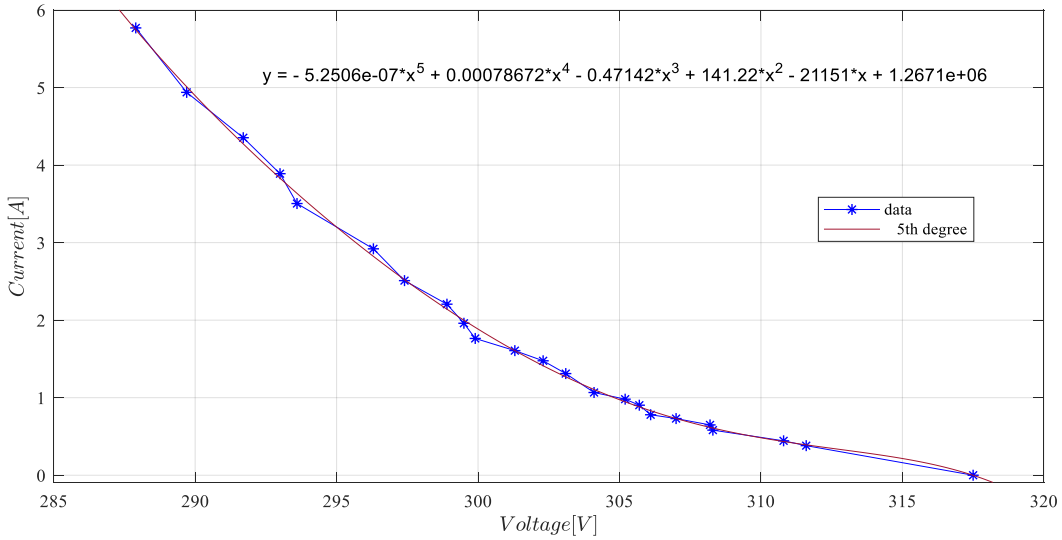

Fig. 63 Experimental setup V/I characteristic

For sake of completeness it is important to highlight that this procedure is useless if a DC/DC converter is inserted in the power train in between the source and the inverter, because the converter can be controlled in order to impose any desired V/I characteristic on the inverter DC side.

5.5.3 Experimental Results

The fast prototyping Approach represents the core and the added value of this chapter. The test consists of providing a ramp signal for the grid voltage, from 35 to 175 V rms phase to phase in 4 seconds, starting at 5 s. During this operation just $Load_1$ is supplied. At 16 s $Load_2$ is posed in parallel for 3.5 s and then it is disconnected. Finally, at 22.3 s $Load_1$ is detached too, and a no load condition is explored. In the following figures, it is possible to see the main variables in their time evolution. Fig. 64 represents the measured rms grid voltage; it can be considered very satisfactory since it does never exceed the range $V_{ac,ref}$ ±10%. Instead Fig. 65 shows the active power supplied to the loads.

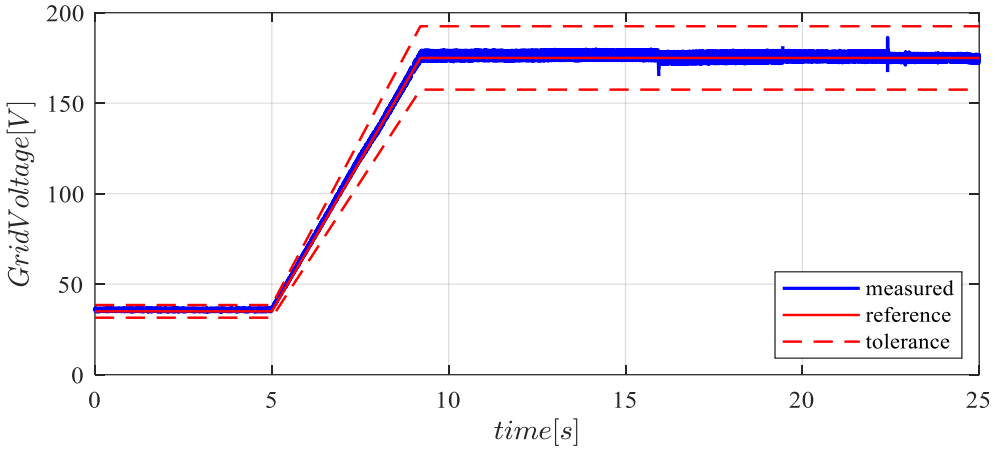

Fig. 64 Grid voltage (rms).

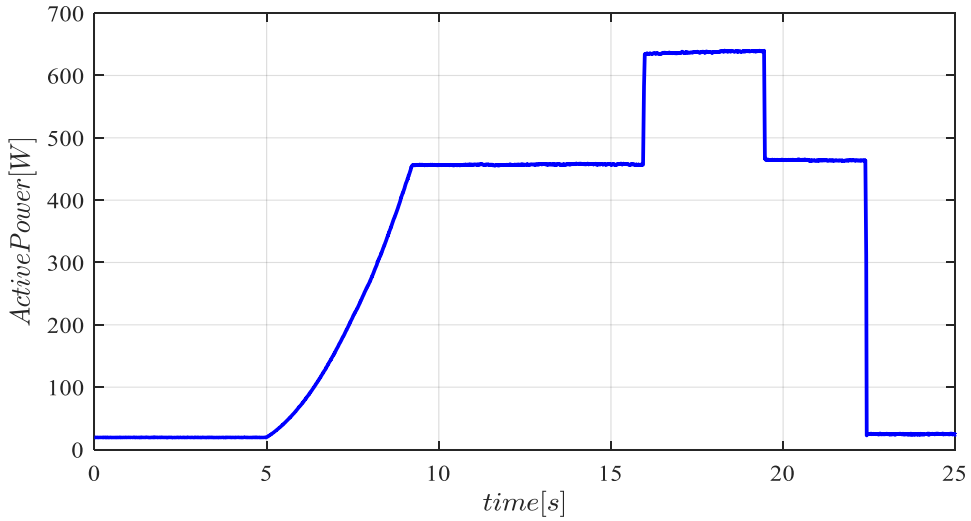

Fig. 65 Active power supplied by grid-forming inverter.

In the previous figure it is possible to see that active power injected at:

- about 12 s and then again at about 21s is exactly $175^2/Load_1$=464W;
- about 17 s is around $175^2/(Load_1 // Load_2)$=655W.

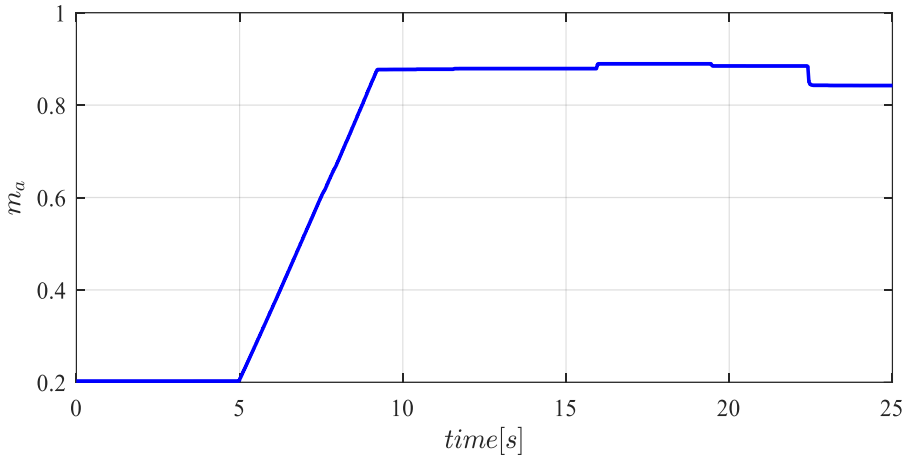

Fig. 66 MPC output - Modulation index

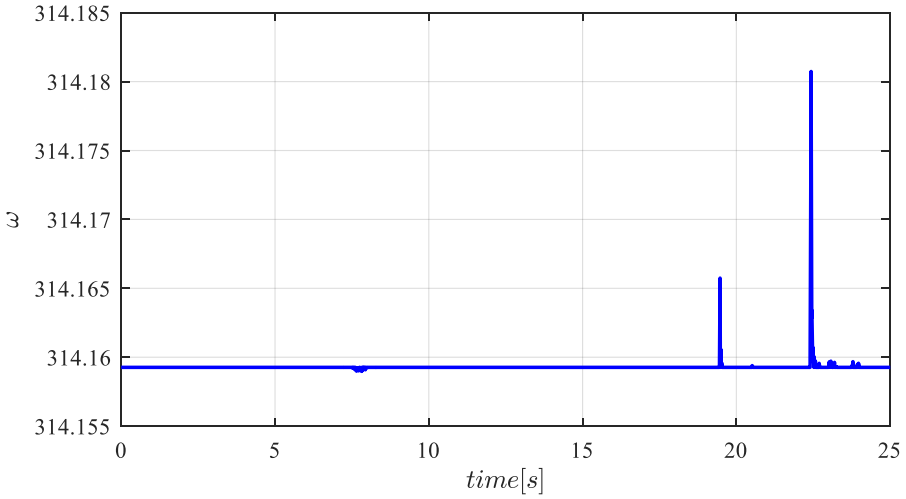

Fig. 67 MPC output – Angular frequency.

Dc voltage is shown in Fig. 68.

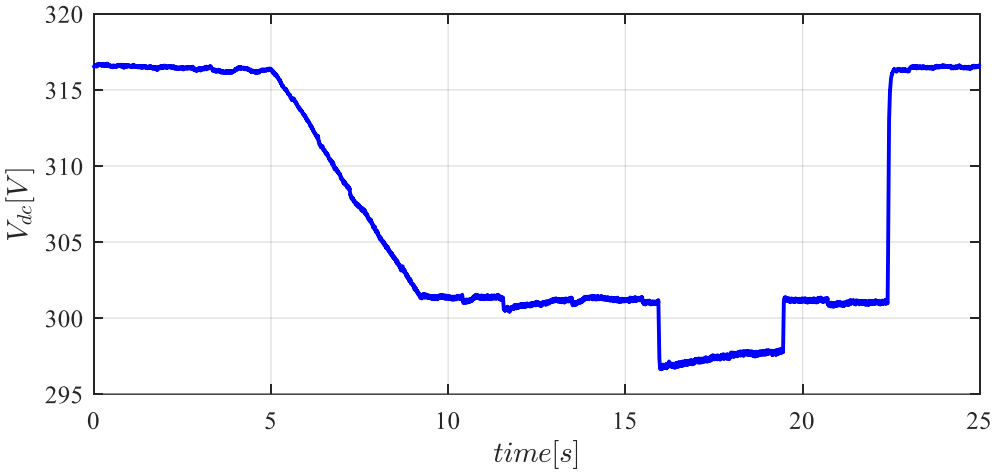

Fig. 68 Dc voltage across C.

During this test, the run time of the QP was recorded between 0.78 and 0.91 ms, i.e. shorter than the MPC sampling time (Ts) equal to 1 ms.

5.5.4 Appendix

The aim of this appendix is to explain how the V/I characterization of the specific powertrain was obtained. The setup is summarized in Fig. 69. It is worthy to remind that any characterization process is meaningful if the conditions in which the characterization takes place is the same used in the utilization. This means that in the characterization activity DC filter, diode bridge and autotransformer are the same used and described before. V/I characteristic was obtained by defining twenty-three different working points (V_{dc}; I_{dc}) by changing twenty-three different values of the resistor R_c. R_c is made changed from infinite (open circuit) to 50 Ω. Measuring points are highlighted in Fig. 69. After recording it is possible to use a fitting tool (e.g. Matlab Basic Fitting) and obtain an analytical relationship. In this work, it is used a 5th order polynomial $I_{dc}(V_{dc})$, whose coefficients are listed in Table 21, because in this specific case a 5th order polynomial is assumed the best trade-off between accuracy and easiness in using MPC process.

Table 21. Polynomial coefficients.

5th	4th	3rd	2nd	1st	zero
-5.25×10^{-7}	7.87×10^{-4}	-0.471	114	-2.12×10^{4}	1.27×10^{6}

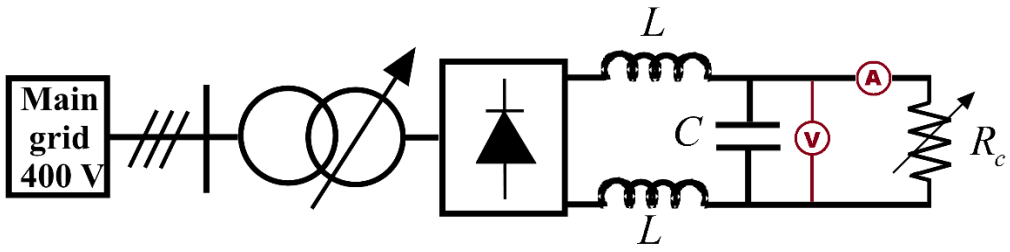

Fig. 69 Characterization experiment setup

5.6 Chapter 5 Conclusions

This chapter proposed a new control strategy for islanded PV-Storage MGs based on decentralized controllers acting without communication to properly manage the MG under all its operational assets. The main advantages of the proposed approach with respect to existing methods are the following: *i*) it can restore voltage and frequency without communication among devices and thus without the necessity of a secondary centralized control scheme; *ii*) it is able to account for the Storage battery power and SOC limits curtailing the consequent over-production of PV units. Three different operating conditions were defined for the controllers (NO, PP and SP) and conditions to automatically switch from one mode to the others were derived. Simulations to validate the performances and the robustness of the proposed control approach were performed in Simulink/Simscape® environment. Results highlighted the effectiveness of the proposed method to reach the above defined goals providing good dynamic performances and achieving a restoration of the system voltage and frequency.

The strategy is described in all the details and it is also proposed in actual implementation. This approach is easily replicable in other labs just adapting the present system to the new power train characteristic. The test results show the effectiveness of the proposed grid-forming control. Future development will focus on

enlarging the laboratory capability in hosting different sources, in that way will be possible to extend the algorithm to grid feeding and grid supporting units to develop further logics and features.

6 Wind Turbine Frequency Support

The increasing penetration of RES and, more in general, of converter connected power generation is progressively reducing the overall inertia of the electricity system introducing new challenges in the network Frequency Support (FS). Therefore, FS strategies for RES are becoming an important aspect to be developed in order to ensure the secure operation of the electricity power grid.

This chapter is composed by two steps: *i*) presenting a general basic outline of the ideas related to power system frequency response and *ii*) proposing a new control strategy for virtual inertia.

The aim of the first part of the chapter is to analyse the possible contributions provided by renewable power plants, with specific focus on wind power generation, on the problem of frequency support.

The aim of the second part of the chapter is to propose an innovative approach for the inertial emulation of Wind Turbine Generators (WTGs) in order to ensure a positive effect on the system frequency avoiding unstable operations of the WTG and reducing the negative impact of the rotor speed recovery on the secondary frequency drop. Moreover, this thesis provides a detailed definition of the triggering logics adopted to activate and deactivate the FS making it suitable for implementation in available industrial controllers. The proposed controller is firstly tested in a simplified configuration to show its enhanced performances with respect to previously developed approaches. Then, simulations are carried out in a more realistic network to assess the positive impact of the controller on the system frequency

6.1 Introduction

In recent years, renewable energies exponentially increased, and this trend has a beneficial effect on environment and on the other hand they introduce some problems in grids management. In this framework, wind power generation is playing and will incisively play the most important role in the migration towards an environmentally sustainable energy mix. Indeed, the total installed wind power at the end of 2016 was equal to almost 486 MW scoring a 11,8 % increase with respect to the amount installed at the end of 2015 (435 MW) and the trend is foreseen to be growing also for the upcoming years the upcoming years [109]. Therefore, their interest in modelling and simulation is increased. Indeed, they can open new possibilities in grid management and ancillary services. Along with the well-established advantages of RES the strong increasing of power generation interfaced to the Transmission and Distribution (T&D) grids by means of power electronic devices, is introducing new challenges related to the necessity of operating the electricity system in a secure and reliable way. Among them, one of the most important related to the secure operation of the T&D network is the reduction of the overall inertial of electricity system. This latter aspect is of great interest since the electric system inertia is the parameter that allows the grid to cope with load variations.

One of the most important drawbacks of the introduction of generation units connected to the network by means of power electronics converters is the reduction of the overall

inertia of the electricity system [110]. For this reason, many Transmission System Operators (TSOs) are conducting extensive studies aimed at implementing Frequency Support (FS) actions to face this inertia reduction [111, 112]. Among the various technologies committed for FS, RES are the most promising ones due to their flexibility and the possibility to define integrated solutions with energy storage units [113] (an exhaustive overview on FS techniques involving RES can be found in [114] where the summary in Fig. 70 is taken from.).

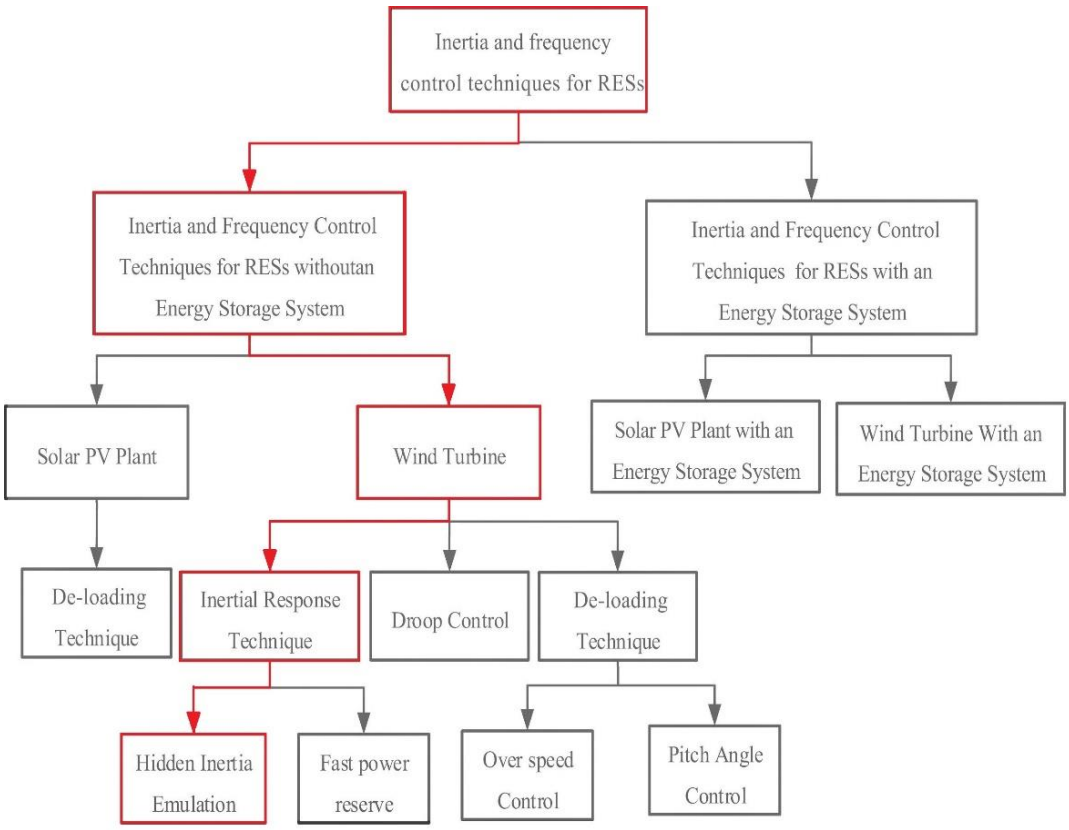

Fig. 70 General overview of FS techniques for various types of RES. The red path indicated the field of application of the thesis.

In particular, Wind Turbine Generators (WTGs) can play an important role in FS due to the relevant amount of kinetic energy stored in the generator rotors. Three are the most diffuse techniques to achieve FS from a WTG, namely inertial response [115], droop control [116] and de-loading [117]. Available strategies belonging to the first category can be further divided in two main families: Hidden Inertia Emulation (HIE) [118] and Fast Power Reserve [119]. The first one is characterized by an emulation of the inertial response of a traditional synchronous generator while the other provides a constant power contribution for a certain amount of time. The main drawback of Fast Power Emulation is the insensitivity to the system perturbation and the difficulty to define the overall contribution to the inertia at power system level [114]. On the other hand, HIE, at least in its classical implementation [118], provides a power contribution proportional to the frequency deviation. However, HIE main drawbacks are the secondary frequency drop with a consequent increase of the frequency nadir during the Rotor Speed Recovery (RSR) phase [120] (when the WTG recalls power from the

grid to restore its optimal speed) and potential unstable behaviours due to the WTG speed reduction that may lead to the disconnection of the WTG from the grid [121]. Attempts to mitigate the problem of the speed reduction have been faced in [122] providing a constant torque inertial contribution, but this makes the HIE controller again insensitive to the entity of the system perturbation (similarly to the Fast Power Reserve technique). In [123] a variable synthetic inertia coefficient is used to reduce the impact of the FS controller on the WTG rotor speed. Nevertheless, the synthetic inertia coefficient of [123] is inversely proportional to the rotor speed thus decreasing the FS contribution in the time frame in which it is more necessary i.e. in the first instants after the frequency transient when the Rate of Change of Frequency (RoCoF) is higher and when the FS would be more effective (i.e. the kinetic energy of the WTG is higher). The issue of the RSR phase is discussed in [124, 125] where a proportional-integral based approach is used to smooth the speed transient. However, the evaluation of the possibility of optimizing the secondary frequency drop is totally overlooked. Instead, a novel strategy to manage the speed recovery phase based on an extended state observer is presented in [126], but this method appears too complex to be installed on a real WTG. Another important issue concerns the definition of suitable FS activation and deactivation logics that should be effective but sufficiently simple to be implemented in available industrial controllers. Some preliminary evaluations about the activation logics of the FS phase are discussed in [127] but no reference is made to the deactivation one. Starting from this state of the art, the aim of the present article is to define a novel approach to design and implement a Variable Hidden Inertia Emulator (VHIE) for WTGs equipped with Permanent Magnet Synchronous Generators (PMSGs). Differently from [123], the proposed FS controller provides an extra power contribution directly proportional to the frequency deviation by means of a WTG speed dependent coefficient that allows: *i*) avoiding unstable conditions caused by a relevant rotor speed reduction and *ii*) providing the maximum contribution to FS in correspondence of the highest speed values at the beginning of the frequency transient. Moreover, the proposed control manages the RSR phase in order to minimize the secondary frequency drop if necessary. Finally, the control logics to be considered to activate and deactivate all the phases of the FS controller are presented and thoroughly discussed together with an effective criterion for the definition of the necessary amount of synthetic inertia needed to satisfy the TSO requests in terms of frequency stability. The effectiveness of the proposed FS control approach is tested by means of two sets of simulations performed with DIgSILENT PowerFactory®. The first one is a simplified test case, which aims at evaluating the controller effects on the WTG dynamics and at comparing its performances with respect to previously developed approaches. Then, a thorough analysis on a dedicated benchmark network is provided in order to assess the proposed controller impact on the FS in a more realistic operational condition.

6.2 The Proposed Strategy

A WTG equipped with PMSG is connected to the AC grid by means of two power electronic devices, namely the Machine Side Converter (MSC) and the Grid Side Converter (GSC) as depicted in Fig. 71. For the sake of brevity a detailed description

of the two converters control system is here omitted but it can be found in [136]. Our attention is focused on the interaction between the MSC control systems and the proposed FS controller.

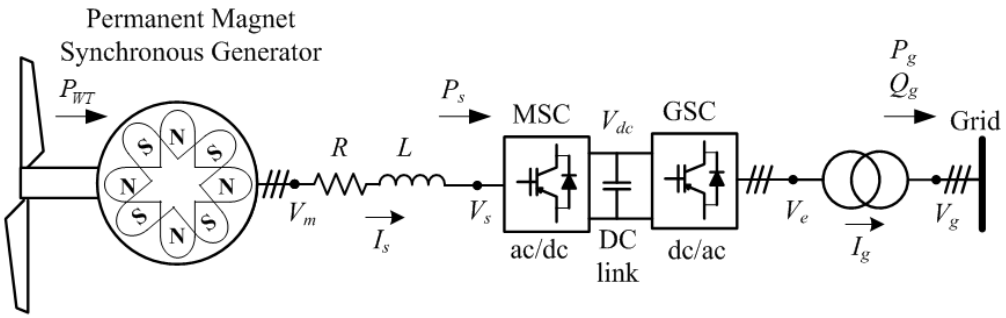

Fig. 71. General layout of a fully-rated WTG equipped with PMSG

The dynamic of the WTG rotor is described by:

$$P_w\left(v_w,\omega_r,\beta\right)-P_s=2H_{WTG}\omega_r\frac{d\omega_r}{dt} \tag{139}$$

being H_{WTG} the WTG inertia (in s on the WTG rated apparent power base), P_s the p.u. stator active power of the PMSG, P_w (p.u.) the power extracted by the WTG, v_w the wind speed in m/s, β the pitch angle in deg and ω_r the rotor speed in p.u. on the rotor rated speed. P_s is controlled acting on the MSC by means of a power control scheme that provides the reference for the stator current quadrature axis component ($i_{sq,ref}$) to the MSC inner current control loop, as shown in Fig. 72. The stator current direct axis reference $i_{sd,ref}$ is set to zero in order to minimize the amplitude of the stator current. Usually, the stator active power reference $P_{s,ref}$ is defined by the MPPT signal calculated on the basis of the rotor speed measurement ω_r in accordance to the well-known MPPT characteristic (see [136]). The FS control signal, P_{VHIE}, is usually added to the MPPT one as depicted in Fig. 72. Let us now analyze the dynamic evolution of the WTG when a FS action is needed and, to better understand the system dynamic evolution, let us refer to Fig. 73. In normal operation, the WTG power production is on the MPPT curve (blue line); in particular, for a fixed wind speed, the equilibrium point in normal operation (A) is the intersection between the MPPT curve and the wind power one (red dashed curve).

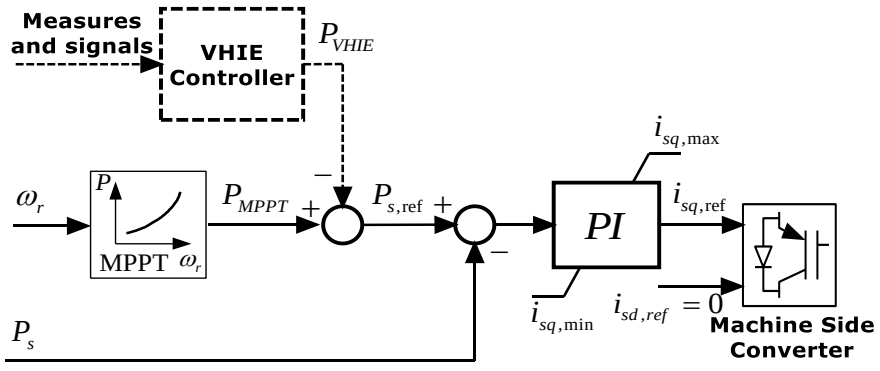

Fig. 72. Power control structure of the MSC.

If FS is required, the WTG controller provides an inertial response increasing the power production (point B). In accordance to (139), the power unbalance makes the WTG decelerate and the system evolves towards point C. The horizontal segment B-B' highlights the possibility of power limitation in order to avoid the converter overloading. When the FS phase terminates (point C) the system passes in the RSR phase (starting at point D). If no recovery strategy was implemented, point D would fall on the blue curve (point D') providing a quicker recovery but a higher power step-down (represented by segment C-D') and thus a higher secondary frequency drop. The proposed idea for the RSR phase is to provide the system with a power reference in between the blue and the red curve in order to get a good trade-off between a reasonably fast recovery and a reduced impact on the secondary frequency drop. Once the system is sufficiently close to the MPPT curve (point E) the RSR phase terminates, bringing the WTG back on the MPPT curve (point F) to return at the normal operation point (A).

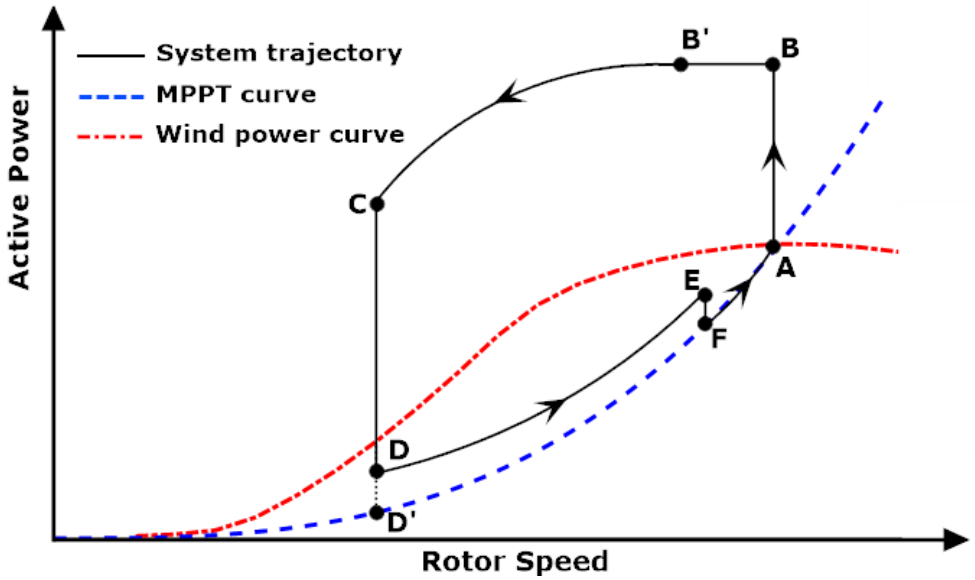

Fig. 73. Schematic description of a WTG dynamics during FS

6.2.1 Activation and deactivation logics for the VHIE controller

The aim of this subsection is to define suitable logics that allow starting and stopping the FS and the RSR phases. The FS phase is activated if the time derivative of the frequency f_e becomes smaller than a warning threshold $RoCoF_{act}$:

$$\frac{d\ f_e}{dt} \leq ROCOF_{act} < 0 \tag{140}$$

This is justified by the fact that, even if different networks in different countries may have different alert values for the RoCoF, the necessity of avoiding high absolute values of the RoCoF is a common element for the safe operation of an electricity grid [140].

In this condition, the FS controller logic switches the FS activation signal S_{FS} (equal to zero in normal operation) to one and keeps it so until a deactivation condition occurs. The deactivation of the FS phase occurs according to the following condition:

$$\frac{d\,f_e}{dt} > RoCoF_{deact} \vee P_{s,ref} < P_{MPPT0} \tag{141}$$

The first one means that the RoCoF has returned over a certain deactivation threshold, $RoCoF_{deact}$ (higher than $RoCoF_{act}$ and at least equal to zero). The second one occurs when, during the FS phase, the reduction of the WTG speed makes the power reference smaller than the power production before starting the FS phase (namely P_{MPPT0}). With reference to the conceptual scheme of Fig. 73, this means that the ordinate of point C is falling below the ordinate of point A, which makes the action of the FS controller useless.

The necessity to know P_{MPPT0} implies that the FS control logic has to store the WTG power reference at the beginning of the FS phase. When one of the two conditions of (141) occurs, S_{FS} switches back to zero while the RSR phase activation signal S_{SR} passes from zero to one and remains so until the RSR phase is over. The RSR phase terminates when the power reference $P_{s,ref}$ is sufficiently close to the P_{MPPT} signal. Defining a positive tolerance threshold $\Delta P_{SR,deact}$, signal S_{FS} returns to zero when:

$$P_{s,ref} \leq P_{MPPT} + \Delta P_{SR,deact} \tag{142}$$

The definition of the state of switching signals S_{FS} and S_{FS} can be easily translated into a circuit composed by logical operators, comparators and flip-flops as depicted in Fig. 74.

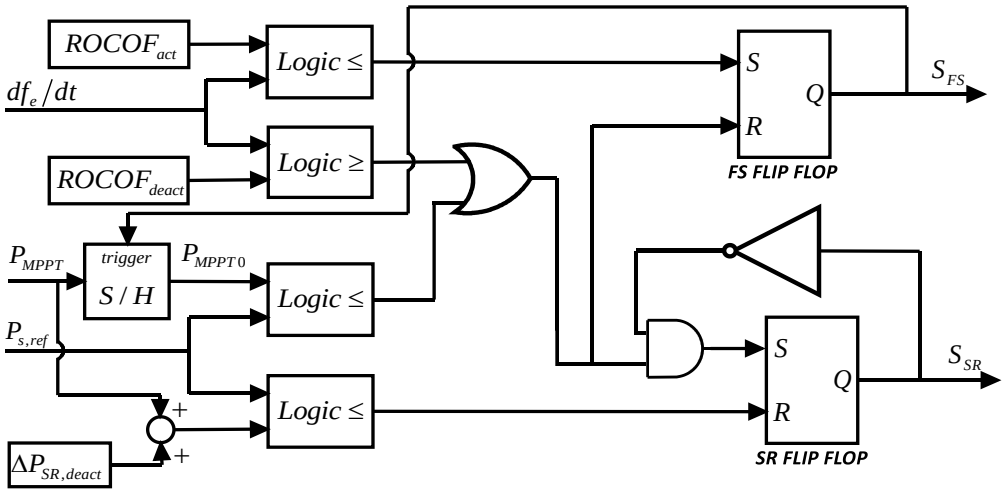

Fig. 74 Implementation logic for the management of the FS and RSR phases for the proposed VHIE controller.

This way, the VHIE controller contribution appearing in Fig. 72 can be written as:

$$P_{VHIE} = P_{FS} \cdot S_{FS} + P_{SR} \cdot S_{SR} \tag{143}$$

being P_{FS} and P_{SR} the power contributions in the FS and RSR phases, that are detailed in the next subsections.

6.2.2 Frequency support phase with variable hidden inertia emulation

The starting point for the proposed VHIE is the structure of the classical HIE (CHIE) controller [118] where the addition synthetic inertia contribution during the FS phase (P_{Synt}), in *p.u.* on WTG apparent power base, is defined as:

$$P_{synt} = 2H_{synt} f_e \frac{d f_e}{dt} \tag{144}$$

where H_{synt} is the synthetic inertia coefficient in s. As highlighted in [121], there are practical limits on H_{synt} with a consequent potential risk of instability and WTG shut down if such limits are overcome. Such limits are somehow related to the reduction of the WTG rotor speed [123]. Therefore, the basic idea of the proposed FS controller is that the FS action has to be more effective during the first part of the transient, when the RoCoF is more severe, and should reduce its contribution when the rotor speed decreases, in order to avoid the stall of the wind turbine. For this reason, H_{synt} coefficient is changed during the FS so that its maximum value is provided when the system enters the FS phase and becomes zero for a limit value of the WTG rotor speed $\omega_{r,min}$. This can be obtained defining the following linear decreasing function:

$$H_{synt}(\omega_r) = H_{\max}\left[1 + \frac{\omega_r - \omega_{r0}}{\omega_{r0} - \omega_{r,\min}}\right] \tag{145}$$

In order to implement (145), the controller needs to "remember" the rotor speed at the beginning of the FS phase ω_{r0}, which can be achieved using a simple Sample and Hold device triggered by the activation signal of the FS phase S_{FS}.

According to (144) and (145), it is possible to define the power contribution P_{FS} in the FS phase as:

$$P_{FS} = 2H_{synt}(\omega_r) f_e \frac{d f_e}{dt} \tag{146}$$

For the actual implementation of the FS scheme, it is also necessary to account for a filtering of the system frequency, in order to wash out disturbances introduced by the frequency measurement and by the numerical frequency derivation appearing in (146). The final scheme of the FS controller is reported in Fig. 75:

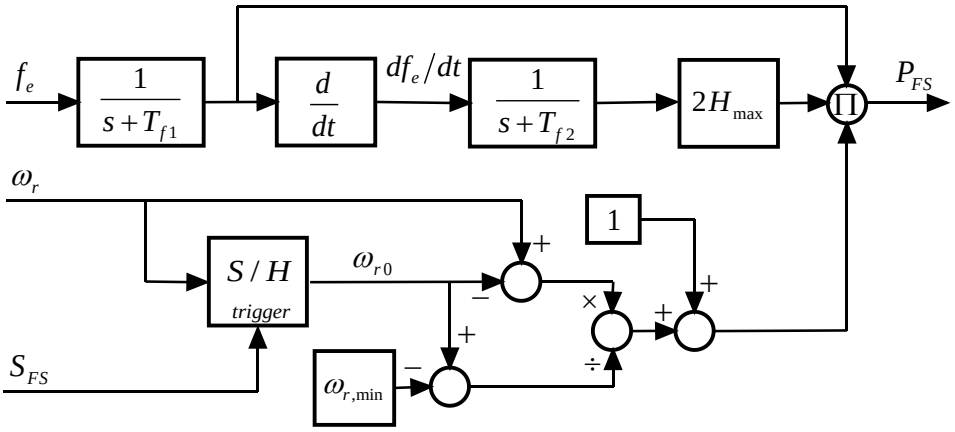

Fig. 75. Block diagram layout of the FS section of the proposed VHIE controller.

The filters time constants T_{f1} and T_{f2} have to be defined in order to remove the noise form the signal without interfering with the performances of the controller.

6.2.3 Rotor speed recovery phase

As discussed earlier, in the RSR phase it is important to control the WTG power reduction in order to avoid a secondary frequency drop and an aggravation of the

frequency nadir [120]. The proposed approach consists in providing a power reference lying in between the MPPT curve (which would produce a higher frequency drop) and the wind power one (which would not allow the WTG optimal speed recovery). Consequently, in the RSR phase, one has that the power reference must be a linear combination of these two extreme situations, that is to say:

$$P_{s,ref} = K_{SR} P_w\left(v_w, \omega_r, \beta\right) + \left(1 - K_{SR}\right) P_{MPPT}\left(\omega_r\right) \tag{147}$$

Being K_{SR} a suitable coefficient between 0 and 1. Now, examining the control scheme appearing in Fig. 72, it is evident that:

$$P_{s,ref} = P_{MPPT}\left(\omega_r\right) - P_{VHIE} \tag{148}$$

so, inserting (147) in (148), recalling (143) and observing that S_{FS}=0 and S_{SR}=1 in the RSR phase, one has that:

$$P_{SR} = K_{SR}\left[P_{MPPT}\left(\omega_r\right) - P_w\left(v_w, \omega_r, \beta\right)\right] \tag{149}$$

In order to implement (149), the control system needs to know an estimation of the wind power P_w, which is possible on the basis of the WTG rotor speed knowing the wind speed v_w (see [136] for the formula). If no wind speed measurement is available, it is enough to observe that in the equilibrium point before the FS phase one had that:

$$P_w\left(v_{w0}, \omega_{r0}, \beta_0\right) = P_{MPPT}\left(\omega_{r0}\right) \tag{150}$$

where the subscript 0 is used to indicate the initial steady-state conditions before the FS action. Now, since both ω_{r0} and β_0 can be measured, it is possible to numerically solve (150) with respect to v_{w0} in order to get an estimate of the initial value of the wind speed. Now, assuming that, during both the FS and the RSR phases the wind speed remains constant, (149) becomes:

$$P_{SR} = K_{SR}\left[P_{MPPT}\left(\omega_r\right) - P_w\left(v_{w0}, \omega_r, \beta\right)\right] \tag{151}$$

which can be easily calculated since both the rotor speed and the pitch angle can be measured. The schematic representation of the proposed configuration for the RSR phase is depicted in Fig. 76.

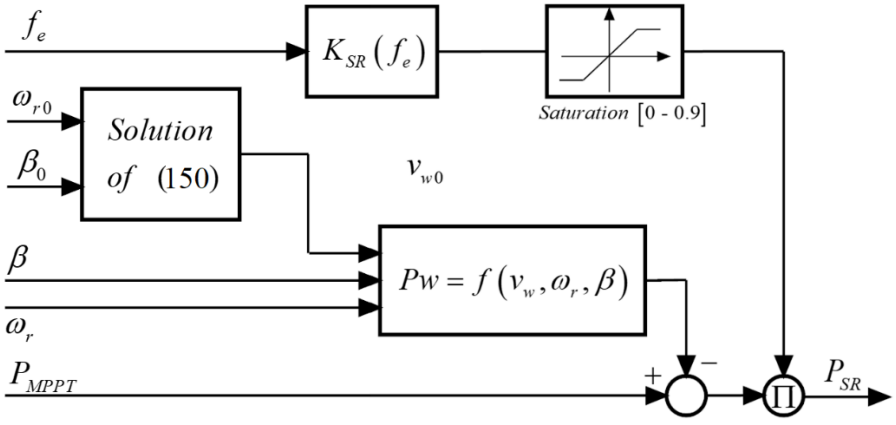

Fig. 76. Block diagram layout of the RSR section of the proposed VHIE controller.

The choice of K_{SR} can be done considering that, if the system frequency is low due to a severe power transient, a secondary frequency drop is highly avoidable; thus K_{SR}

should be the higher possible (e.g. 0.9). On the other hand, if the system frequency is far from critical values, the secondary frequency drop is not too compromising for the system and one could opt for a quicker but more demanding RSR choosing K_{SR} close to 0. For this reason, one can set:

$$K_{SR}(f_e) = 0.9\left(1 - \frac{f_e - f_{\min}}{f_{\max} - f_{\min}}\right) \tag{152}$$

Being f_{min} and f_{max} limits values of the system frequency to be defined in accordance to the specific grid requirements of the system where the WTG is installed. Out of the range defined by f_{min} and f_{max} K_{SR} is saturated to 0.9 and 0 respectively.

An overall representation of the proposed VHIE controller to be integrated in the MSC power controller is depicted in Fig. 77.

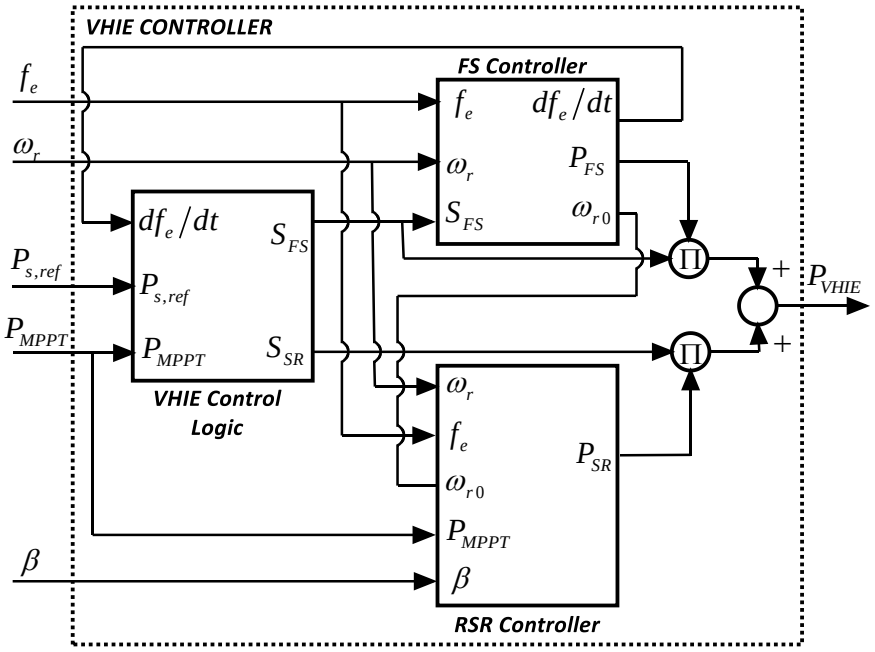

Fig. 77. Overall architecture of the proposed VHIE controller

6.2.4 A Criterion for the definition of the WTG synthetic inertia

As a final comment, it is worth providing an applicative criterion for the definition of the VHIE coefficient H_{max}. If one considers a power system with N_{SG} synchronous machines and no WTGs, the overall system inertia H_{tot} can be calculated as:

$$H_{tot} = \sum_{i=1}^{N_{SG}} H_{SG,i} S_{r,i} \Big/ \sum_{i=1}^{N_{SG}} S_{r,i} \tag{153}$$

where $H_{SG,i}$ is the inertia in s and $S_{r,i}$ is the rated apparent power in MVA of the *i-th* synchronous machine. According to [141] the maximum RoCoF is inversely proportional to H_{tot} and can be estimated as:

$$RoCoF_{\max} = \frac{\Delta P_L}{P_L} \frac{f_0}{2H_{tot}} \tag{154}$$

being ΔP_L and P_L the load variation and the total load of the system in MW and f_0 the initial frequency in Hz. If WTGs are included in the power system and no FS is provided, the overall installed power of the system increases but since no additional inertia is seen by the grid, the overall inertia coefficient H_{tot} decreases:

$$H_{tot} = \sum_{i=1}^{N_{SG}} H_{SG,i} S_{r,i} \Bigg/ \left(\sum_{i=1}^{N_{SG}} S_{r,i} + \sum_{j=1}^{N_{WTG}} S_{WTG,j} \right) \tag{155}$$

being N_{WTG} the number of WTGs and $S_{WTG,j}$ the rated apparent power of the *j-th* WTG. This implies that, at fixed ΔP_L, $RoCoF_{max}$ increases making the system frequency weaker.

A criterion for the definition of the synthetic inertia coefficient of the proposed VHIE controller could be the following: imposing a $RoCoF_{max}$ reference value for a certain load variation (e.g. the same the system had when only traditional power generation was present or one defined by the local TSO) and then calculating the necessary power system inertia H_{tot} using (154). Recalling that for the first instants of the FS transient the proposed VHIE controller (146) behaves like the traditional HEI (144) providing synthetic inertia equal to H_{max}, one can rewrite (155) introducing the contribution of the N_{FS} WTGs providing FS (with $N_{FS} \leq N_{WTG}$) obtaining:

$$H_{tot} = \frac{\sum_{i=1}^{N_{SG}} H_i S_{r,i} + \sum_{k=1}^{N_{FS}} H_{max,k} S_{WTG,k}}{\sum_{i=1}^{N_{SG}} S_{r,i} + \sum_{j=1}^{N_{WTG}} S_{WTG,j}} \tag{156}$$

Imposing H_{tot} in (156) it is possible to determine the overall inertia necessary from all the WTGs providing FS:

$$\sum_{k=1}^{N_{FS}} H_{max,k} S_{WTG,k} = H_{tot} \left(\sum_{i=1}^{N_{SG}} S_{r,i} + \sum_{i=1}^{N_{WTG}} S_{\mathrm{WTG},i} \right) - \sum_{i=1}^{N_{SG}} H_i S_{r,i} \ . \tag{157}$$

The repartition among the N_{FS} WTGs can be done according to various criteria; however, if one assumes that H_{max} is the same for all WTGs contributing to FS (and it is reasonable since $H_{max,k}$ are in p.u. on WTG base) one can simplify (157) as:

$$H_{max} = \frac{H_{tot} \left(\sum_{i=1}^{N_{SG}} S_{r,i} + \sum_{i=1}^{N_{WTG}} S_{\mathrm{WTG},i} \right) - \sum_{i=1}^{N_{SG}} H_i S_{r,i}}{\sum_{k=1}^{N_{FS}} S_{WTG,k}} \ . \tag{158}$$

This criterion can be easily applied to new WTG installations, imposing that their insertion will not affect the system RoCoF, or one can use it for the retrofit of existing WTGs in order to improve the RoCoF to more secure values.

6.3 Illustration of the Proposed Frequency Support

In this section, the proposed VHIE control strategy is tested on a simplified grid configuration in order to evaluate its expected impact on the system frequency and on

the WTG dynamics. The network and WTG models are implemented in DIgSILENT PowerFactory. The layout is the same proposed in Fig. 71 and PMSG WTG model includes all the control loops of the MSC and GSC together with inner current control loops of the two converters. As one could know, DIgSILENT does not include into its library a detailed model of the fully rated wind generating units or of the PMSG. For this reason, the WTG model has been developed by the authors as a user-defined one including: the wind model, a third order model for the PMSG, a first harmonic representation for the MSC and GSC and all the machine controllers such as the MPPT, the DC voltage and the reactive power controller together with the inner current controllers of the two converters. As a result, the WTG is described by a sixth order dynamic system. For the sake of brevity a detailed description of the WTG model is here omitted; nevertheless, details about the structure implemented in DIgSILENT and the parameters used for the following simulations are the same defined in [136]. In order to achieve a dynamic response of the system frequency, the external grid connected to the High Voltage (HV) side of the WTG transformer is considered as fixed in voltage (infinite short circuit power) but characterized by a finite inertia H_g and a droop b_p. The frequency dynamics is triggered by a step load variation on the grid side of the power system. The impact of the proposed FS strategy on the system frequency is compared with the case of no FS and of FS provided by the CHIE control scheme. In accordance to the criteria given by ENTSO-E technical documentation [142], a critical value of the system RoCoF is assumed equal to -0.5 Hz/s, thus all the parameters of the frequency controllers are defined in Table 22. The proposed simulations are relevant to two different scenarios: the first one (case A) is characterized by $H_{synt}=H_{max}=100$ s i.e. a value that provides a stable operation for the CHIE; the second (case B) by $H_{synt}=H_{max}=250$ s for which the CHIE causes a disconnection of the WTG as pointed out in [121]. The proposed frequency transient has been chosen to be very severe to stress the performances of the considered FS controllers and to better highlight the improved performances of the proposed approach with respect to classical one. For this reason, the final frequency falls to 47.5 Hz, the lower limit value provided by [143] for which the system has to ride through for a minimum of 30 minutes.

Table 22 Controllers parameters

Symbol	VHIE Controller	CHIE Controller
$RoCoF_{act}$	-0.25 Hz/s	-0.25 Hz/s
$RoCoF_{deact}$	0.00 Hz/s	0.00 Hz/s
$\Delta P_{SR,deact}$	0.01 p.u.	-
$\omega_{r,min}$	0.3 p.u.	-
f_{min} / f_{max}	47 / 49 Hz	-

6.3.1 Case A

The system frequency response in the proposed scenario is depicted in Fig. 78. As one can notice, in case of no FS (black dotted curve) the system frequency presents a

steeper frequency transient in the first instants after the load variation. This is confirmed from Fig. 79 where one can notice the RoCoF without FS falling below the critical value of -0.5 Hz/s.

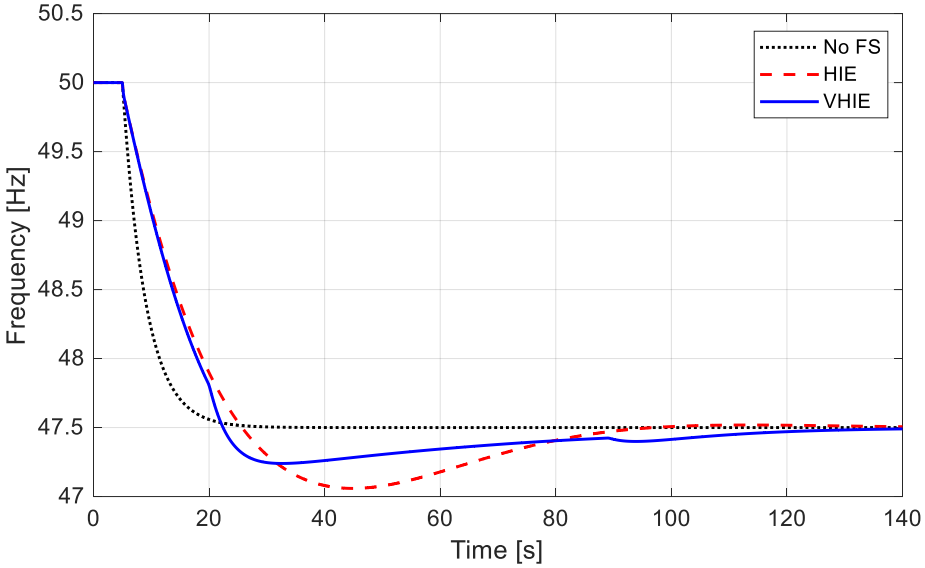

Fig. 78. Frequency time profile

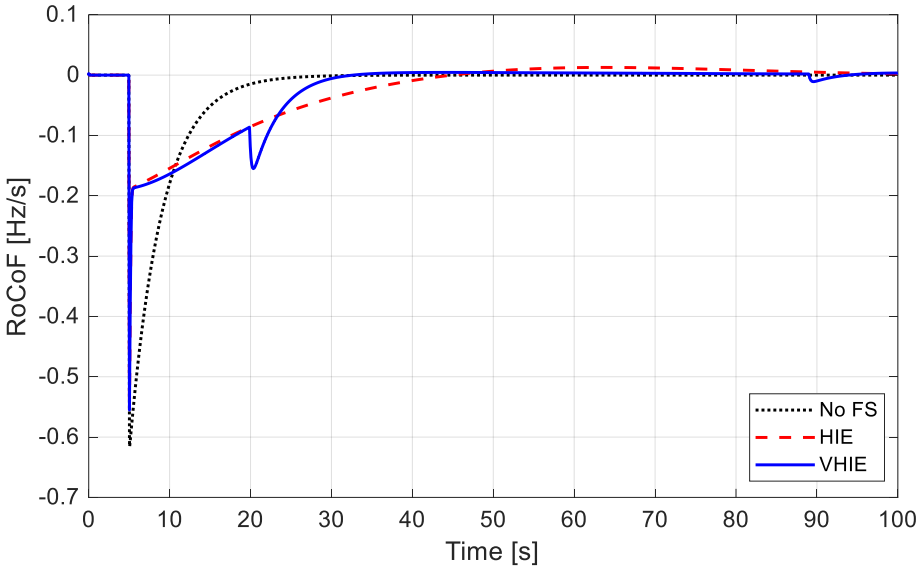

Fig. 79. System Rate of Change of Frequency time profile

The action of the VHIE and HIE are very similar in the FS phase providing a significant increasing of the system RoCoF that passes very rapidly from -0.5 Hz/s to almost -0.2 Hz/s. At about 20 s the VHIE control exits from the FS phase switching to the RSR one. In this transition, one can notice a minimal effect on the system RoCoF that is recovered very quickly but a sensible improvement of the frequency secondary drop, with a consequent improvement of the frequency nadir with respect to the HIE control. Fig. 80 reports the WTG rotor speed during the transient.

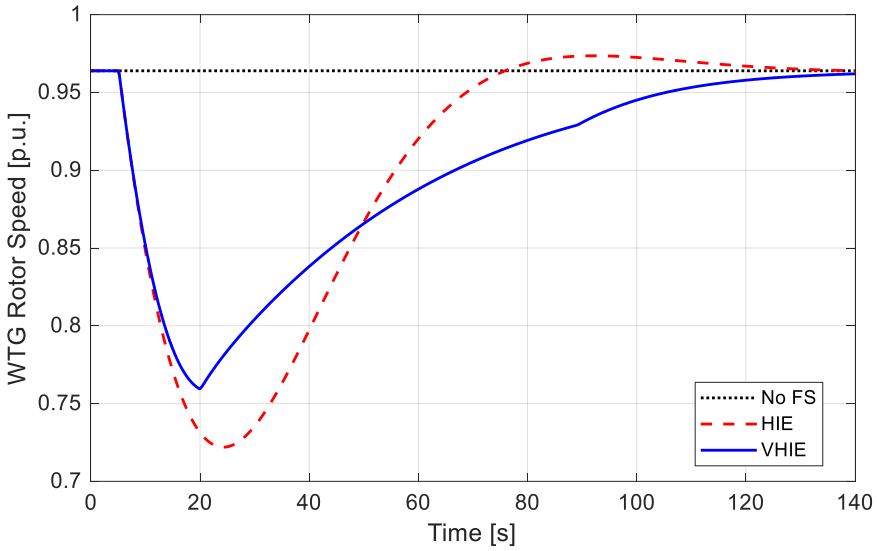

Fig. 80. WTG rotor speed time profile

As one can see, beside almost identical performances on the RoCoF, the rotor speed with VHIE has a lower reduction with respect to the HIE. In addition, the speed recovery is more performing since the VHIE avoids the rotor speed overshoot. Even if the RSR is controlled in the proposed configuration one can notice from Fig. 80 that the time needed to restore the rotor speed is substantially the same as with the HIE control strategy.

Fig. 81 highlights the power reference evolution during the simulation. It starts on the MPPT curve before increasing to perform the FS.

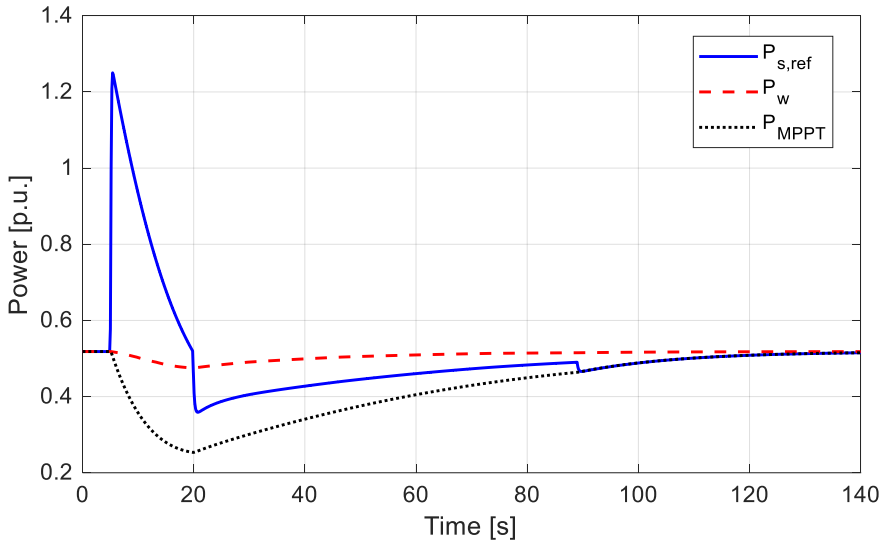

Fig. 81. Stator power reference time profile.

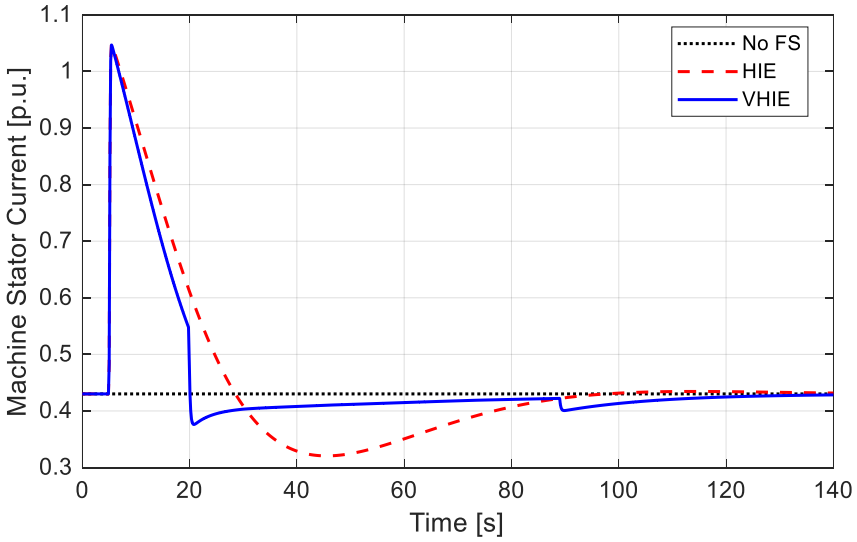

Fig. 82. Machine stator current time profile

Then, during the RSR, the power reference correctly falls between the wind power (red dashed curve) and the MPPT curve (dotted black one). Fig. 82 reports the time domain waveform of the machine current, highlighting that, even in the FS phase, the PMSG is not overloaded (20% overrating for the converter current was considered).

6.3.2 Case B

In order to highlight the stability properties of the proposed VHIE a simulation with high values of synthetic inertia is proposed. As pointed out in [121], in this configuration the HIE exhibits unstable operations due to the severe speed reduction that is not recovered by the WTG, as shown in Fig. 83.

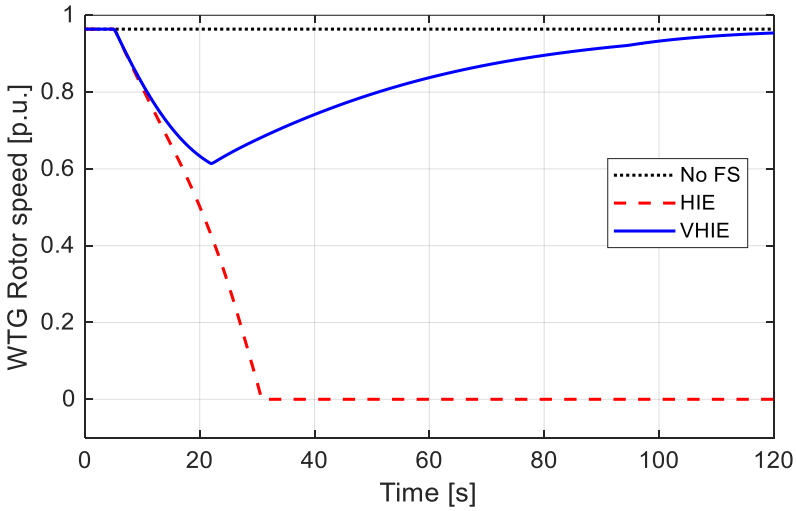

Fig. 83. WTG rotor speed time profile.

On the other hand, the VHIE is designed to reduce its contribution when the rotor speed decreases too much and thus the WTG stability is always achieved. This is a very important point because if during a FS action the WTG stalls, the network is losing further generation causing an aggravation on the system frequency. This can be seen in Fig. 84 where the WTG disconnection provides a secondary frequency

decreasing and an aggravation of the system frequency final value due to the reduction of the overall power generation (it is like having a bigger load variation).

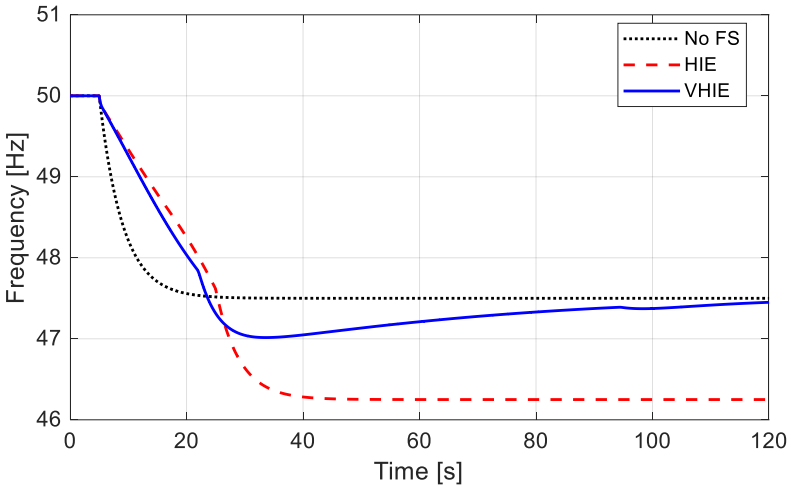

Fig. 84. Frequency time profile

6.4 Test-Case Definition

The validation of the proposed VHIE control system has been performed considering a benchmark network defined to perform wind power integration studies [144] and implemented in DIgSILENT PowerFactory. This test-case network aims at evaluating the performances of the proposed VHIE in a more realistic condition where the frequency dynamics are different from the academic ones showed in §6.3 due both to a more complex topology and to a more complete model of the synchronous generators equipped with governors, primary frequency regulators and AVRs (see [144] and [145] for their parameters). As far as the WTGs are concerned the model used is the same as §6.3 and thus accounting for all the electromagnetic dynamics of the PMSG and all the WTG control systems.

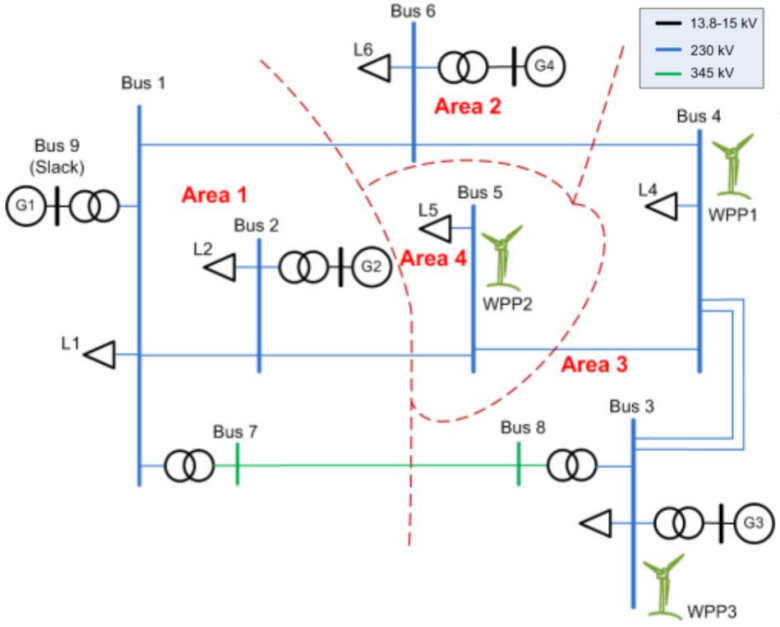

Fig. 85. Benchmark network layout

The system is a 12-bus, four machines network, characterized by a 230 kV ring and a 345 kV line. Power generation are connected to MV busses at 13.8 kV or 15 kV, as depicted in Fig. 85. Network parameters are omitted for the sake of brevity but all the data can be found in [144]. The six loads require a total active power equal to 1,470 MW and a total reactive power equal to 705 MVAr. In the Base Reference Scenario (BRS), no wind power generation is considered and the system accounts for a total installed power from synchronous generators equal to 2,248 MVA. The overall system inertia for the BRS, calculated using (153), is 3.95 s on the basis of the main generator data reported in Table 23 [144].

Table 23 Generator parameters for the BRS

Generator	Number of generators	Rated Power [MVA]	Inertia [s]
G1	6	125	4.77
G2	4	160	3.96
G3	2	192	3.30
G4	3	158	3.18

The BRS is then modified introducing three Wind Power Parks (WPPs) at Bus 3, Bus 4 and Bus 5, namely WPP1, WPP2 and WPP3. WPP1 and WPP2 represent the aggregation of 100 WTGs, each characterized by 2 MW rated power, while WPP3 accounts for the aggregation of 80 WTGs. In this configuration, from now on indicated with Wind Integration Scenario (WIS), the total installed wind power is equal to 560 MVA. Traditional power generation in WIS is reduced to 1,736 MVA resulting in a RES penetration is equal to 24% with respect to the total installed power generation. With respect to the data of Table II the WIS accounts of a reduction of two 160 MVA generators and one 192 MVA generator. The introduction of the three WPPs in place of traditional generation causes a reduction of the system inertia which is now equal to 3 s (calculated in accordance to (155)).

The load flow condition of the WIS is characterized by the same load request of the BRS while WPPs are set to produce different powers (i.e. assuming different wind conditions for each WPP) in order to account for different WTG operating points before contributing to FS (all at unitary power factor). In the WIS the WTGs of WPP1 produce 1 MW active power, WTGs of WPP2 produce 1.4 MW while WTGs of WPP3 produce 1.8 MW for a total RES production equal to 384 MW (around 26% of the total load demand). For both the BRS and the WIS a 120 MW increasing of load L1 generates a frequency transient.

The parameters of the VHIE controllers for the three WPPs are the same reported in Table I while the synthetic inertia coefficient H_{max} is set to 4 s and has been calculated in accordance to (158) imposing the inertia of the system for the WIS H_{tot} equal to the value of the inertia in the BRS.

6.5 Simulations and Results

As one can see from Fig. 86, the frequency transient in the BRS (red dashed curve) is oscillatory and characterized by a frequency nadir of 48.9 Hz. Also the RoCoF in

the BRS, red dashed curve of Fig. 87, is reasonable with minimum value around -0.4 Hz/s.

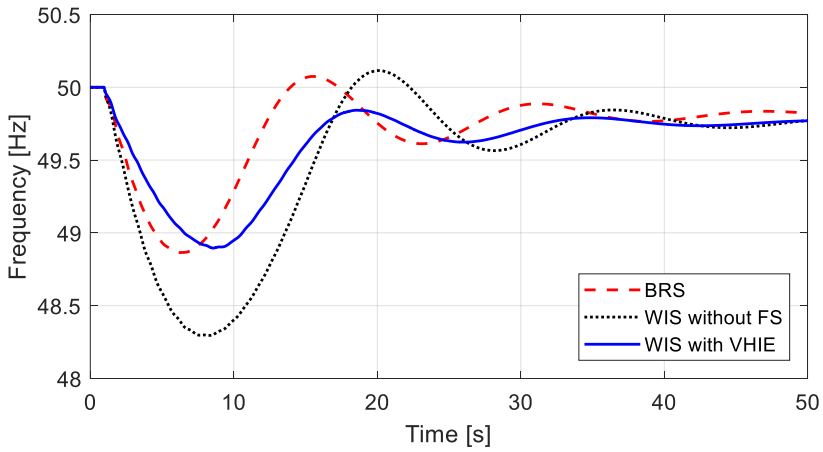

Fig. 86. Frequency time profile

For the WIS, the frequency behaviour is evaluated in two conditions: the first one without FS from the WTGs (black dotted lines) and the other with the proposed VHIE (blue solid lines).

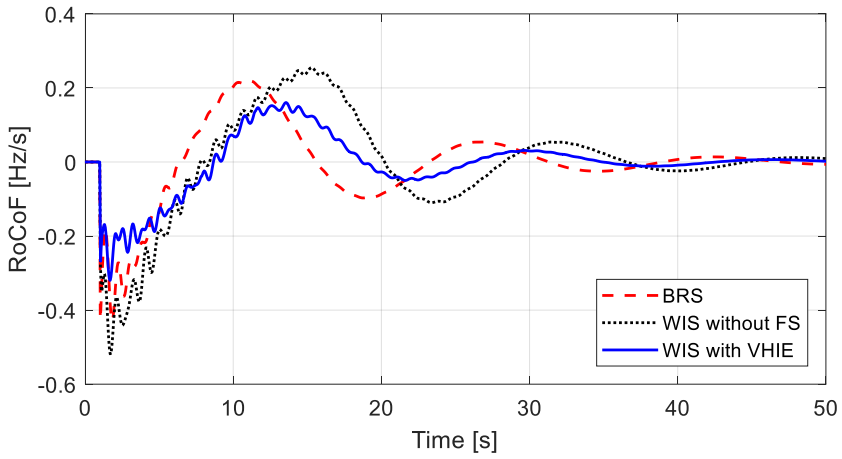

Fig. 87. System Rate of Change of Frequency time profile

Fig. 86 shows that after the introduction of the wind power generation without the FS controller the system frequency suffers from a degeneration of the frequency dynamics. The frequency nadir falls below 48.5 Hz and the initial RoCoF is steeper. This is confirmed in Fig. 87 where RoCoF for the WIS scenario without FS overcomes the limit threshold of -0.5 Hz/s. This critical condition is well coped by the proposed VHIE which provides an effective FS action.

Fig. 86 shows the increasing of the frequency nadir, coming back to the same values reach the in BRS. Also, the system RoCoF has a significant improvement since it does not exceed the value of -0.3 Hz/s and it is less swinging even if compared with the BRS.

Finally, Fig. 88 provides a plot of the power contribution in p.u. of the three WPP in order to highlight the good performances of the proposed VHIE in different operational conditions of the WTGs.

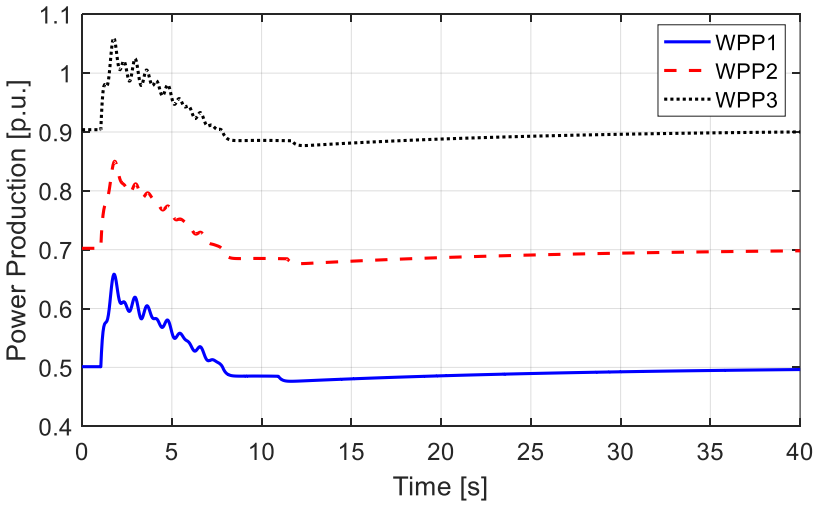

Fig. 88. WPPs power production time profile.

Moreover, it could be interesting to compare the effects of two different FS strategy in the same grid, same penetration and same external condition as explained in §6.5.

In the following picture it is possible to have at glance the benefit introduced by the VHIE in terms of Frequency, nadir and RoCoF.

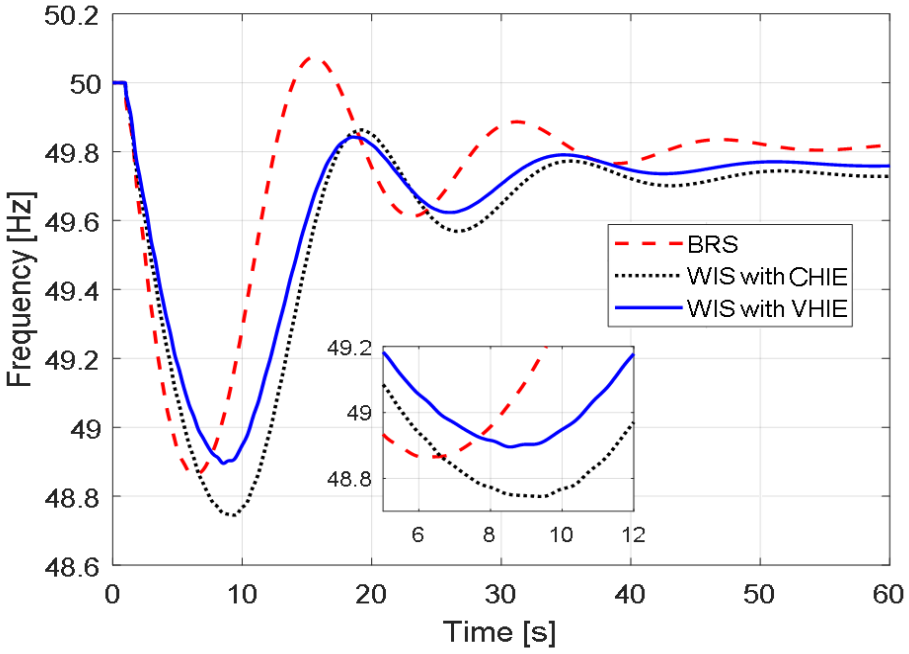

Fig. 89 Frequency comparison

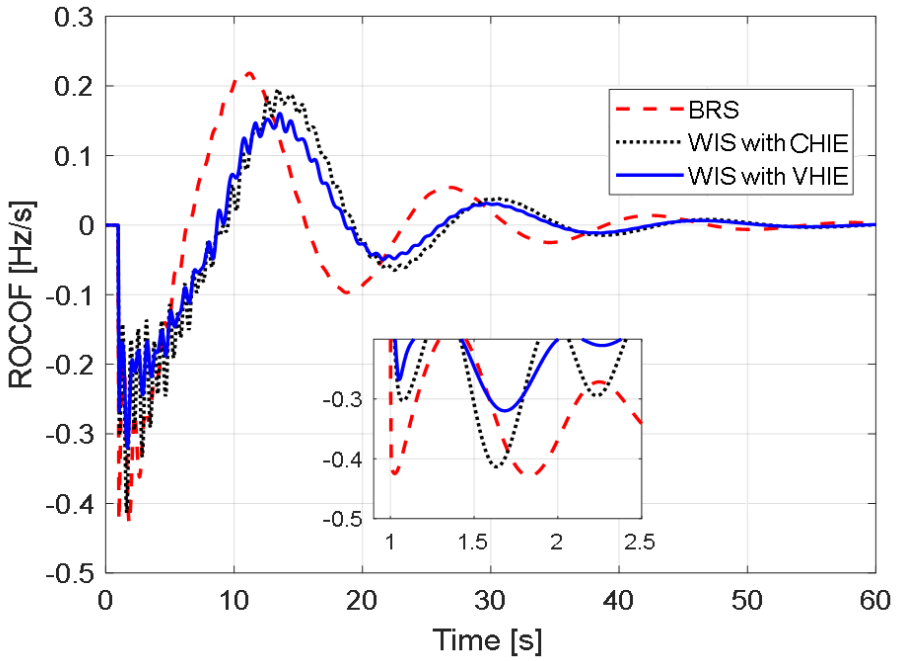

Fig. 90 RoCoF comparison

6.6 Chapter 6 Conclusions

This thesis proposed a new methodology to enable WTG to provide FS by means of a VHIE controller designed to avoid unstable operation of the WTG with a strong contribution at the first instants of the frequency transient. Moreover, the proposed architecture accounts for a suitable management of the RSR phase, that might be critical for the CHIE strategy, and for dedicated activation and deactivation logics easily implementable on industrial controllers. The performance of the proposed FS controller has been initially tested on a simplified configuration in order to assess its impact on the WTG dynamics in comparison with a classical HIE approach. Secondly, a more realistic set of simulations has been proposed on a dedicated test-case network in order to evaluate the behaviour of the VHIE when frequency dynamics are also affected by traditional generators primary frequency controller and AVRs. Simulation highlighted the better performances of the proposed VHIE on the WTG dynamics with a reduced rotor speed decreasing and a softer RSR phase. Moreover, VHIE has shown to avoid unstable behaviour exhibited by CHIE. The proposed VHIE has also shown an effective impact on the system frequency providing a reduction of the system RoCoF and the increasing of the frequency nadir restoring a condition very similar to the one characterized by all traditional power generation. Future developments will regard the possibility of integrating the proposed strategy with storage devices in order to improve the flexibility of the FS. This could give the possibility of including a droop controller making the WTG more and more similar to a traditional power plant in case of need.

7 Conclusions

This thesis has dealt with some interesting topics in electrical engineering research, i.e. microgrid control, microgrid stability and wind turbine integration into traditional grids.

As stated in Fig. 91 the interest in microgrid is quickly increasing since 2015, year in which the candidate started in researching on this topic, moving from about 3000 published articles collected in Scopus in 2015, up to more than 9000 just four years after. Again, the same could be explained for the other studied topic, i.e. synthetic inertia, that in the same time span has moved from 211 to 436 in the same database (Fig. 92).

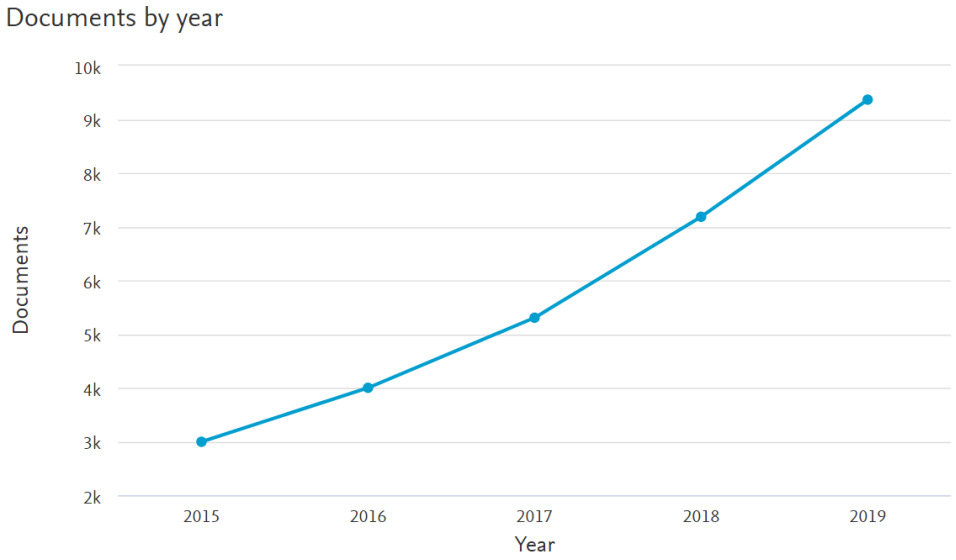

Fig. 91 Documents by year for “Microgrid”

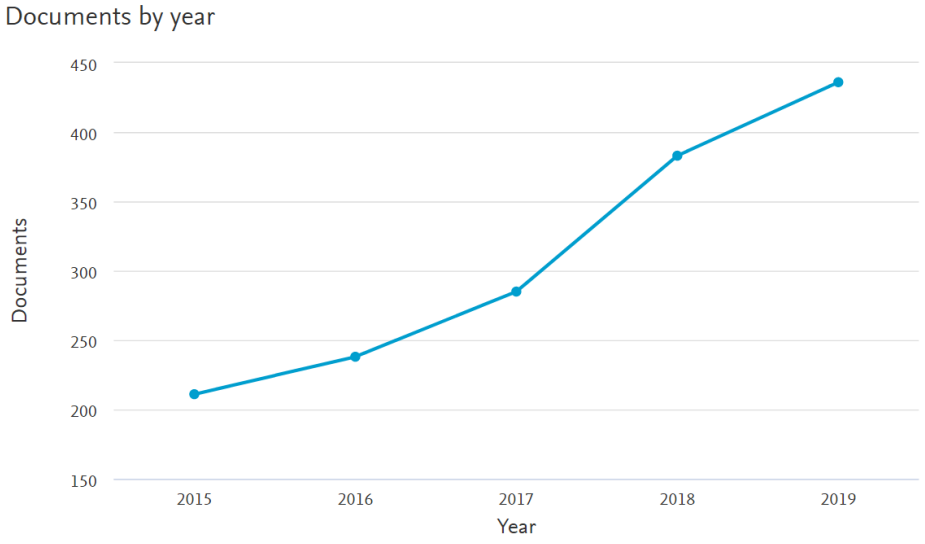

Fig. 92 Documents by year for “Synthetic inertia”

In the previous chapters, a detailed state of the art and literature review on the main topics are analysed and used in order to define a path to move the research forward.

Control problems related to the management of microgrids cover a wide range of possible topics. In this Ph.D. thesis, some of them have been considered in some details, and possible approaches for the solution of such problems have been developed. A considerable attention has been devoted to the analysis of problems relevant to modelling, stability and control. These problems have been analysed using different tools and approach, mixing experimental validation, theory and mathematical demonstrations and simulation using different software. On the other hand, a simple but very effective strategy to deplete the stored kinetic energy by a decelerating wind turbine speed. The amount of active power support depends on several static and dynamic factors, including wind speed and wind turbine inertia. The merit of this thesis is in providing a complete strategy, detailed in logic trips, impact evaluation and wind speed estimator without using an anemometer

The chosen steps for this three-years microgrid research can be summarized in few lines as follows:

- to define a reliable and simple model for microgrid simulation;
- to test it in real microgrid environment and validate it;
- to empower tools for well know microgrid control strategies and simulate them using the microgrid model;
- to define a new strategy for frequency and power flow management; and simulate it using the microgrid model;
- to test the proposal strategy in lab.

Analogous steps for the wind turbine control, i.e.:

- to study the synthetic inertia control state of the art and to understand what could be improved;
- to defining a new and simple strategy able to go over the limitations and the deficiencies of the other control;
- to test in through a powerful tool in a significant power system.

This thesis opens some new scenarios and new research area that in future could be investigated.

In particular, the MPC approach, that allows to combine the first and the second control layer in one even more complete able to manage critical situations, is already deeply investigated in this thesis. Future developments would move towards, first to grid follower inverter and then towards more complex experimental environment, e.g. at the SPM, involving also the batteries of charging cars, in order to evaluate the actual scalability of this strategy.

Moreover, the stability algorithm for microgrid could be refined and implemented in working microgrid controlled by droop strategy. Obviously, it could be adapted in order to be able to study the stability problem under other droop-based controls, such as virtual impedance.

Finally, about VHIE, a specular strategy for over-frequency contingency could be studied and developed, i.e. increasing the rotational speed and paying attention to avoid any wind turbine instability.

The efforts and the novelty were awarded with publications in internationals journals and conferences.

References

[1] A. M. Faisal, "Microgrid modelling and online management," *Espoo,* 2008.

[2] F. Katiraei, R. Iravani, N. Hatziargyriou, and A. Dimeas, "Microgrids Management – controls and operation aspects of microgrids," *IEEE Power and Energy Magazine,* vol. 6, no. 3, 2008.

[3] F. Katiraei and M. R. Iravani, "Power Management Strategies for a Microgrid With Multiple Distributed Generation Units," *IEEE Transactions on Power Systems,* vol. 21, no. 4, pp. 1821-1831, 2006.

[4] B. Delfino, F. Fornari, and R. Procopio, "An effective SSC control scheme for voltage sag compensation," *IEEE Transactions on Power Delivery,* vol. 20, no. 3, pp. 2100-2107, 2005.

[5] F. Fornari, R. Procopio, and M. H. J. Bollen, "SSC compensation capability of unbalanced voltage sags," *IEEE Transactions on Power Delivery*, vol. 20, no. 3, pp. 2030-2037, 2005.

[6] Manitoba-HVDC. *PSCAD Library*. Available: www.hvdc.ca/knowledge-library/reference-material

[7] PartSim. *SPICE Simulator*. Available: www.partsim.com/simulator

[8] Plexim. *PLECS*. Available: https://www.plexim.com/

[9] I. Bendato, A. Bonfiglio, M. Brignone, F. Delfino, F. Pampararo, and R. Procopio, "Definition and On-Field Validation of a Microgrid Energy Management System to manage Load and Renewables Uncertainties and System Operator Requirements," *Electric Power System Research Journal*, 2017.

[10] T. Porsinger, P. Janik, Z. Leonowicz, and R. Gono, "Modelling and Optimization in Microgrids," *Energies,* vol. 10, no. 4, p. 523, 2017.

[11] S. Aman, Y. Simmhan, and V. K. Prasanna, "Energy management systems: State of the art and emerging trends," *IEEE Community Magazine,* vol. 51, no. 1, pp. 114-119, 2013.

[12] J. A. P. Lopes, C. L. Moreira, and A. G. Madureira, "Defining control Strategies for Microgrids islanded Operations," *IEEE Trans. Power Syst.,* vol. 21, 2006.

[13] E. Dall'Anese, H. Zhu, and G. B. Giannakis, "Distributed optimal power flow for smart microgrids," *IEEE Trans. Smart Grid,* 2013.

[14] A. Bonfiglio *et al.*, "Approximate characterization of large Photovoltaic power plants at the Point of Interconnection," in *50th UPEC* 2015.

[15] E. Muljadi and e.a., "Equivalencing the collector system of a large wind power plant," in *PES Gen. Meeting IEEE*, 2006.

[16] A. Bonfiglio, F. Delfino, M. Invernizzi, P. Serra, and R. Procopio, "Criteria for the Equivalent Modeling of Large Photovoltaic Power Plants," in *IEEE Power and Energy Society General Meeting*, 2014.

[17] C. Changchun, D. Lihua, D. Weili, and Z. Jianyong, "Characteristic model based micro-grid equivalent modeling," in *2014 International Conference on Power System Technology*, 2014, pp. 3035-3040.

[18] A. Hussain, V.-H. Bui, and H.-M. Kim, "Robust Optimization-Based Scheduling of Multi-Microgrids Considering Uncertainties," *Energies,* vol. 9, no. 4, p. 278, 2016.

[19] C. Ahn and H. Peng, "Decentralized and Real-Time Power Dispatch Control for an Islanded Microgrid Supported by Distributed Power Sources," *Energies,* vol. 6, no. 12, p. 6439, 2013.

[20] L. Hernandez, C. Baladrón, J. Aguiar, B. Carro, A. Sanchez-Esguevillas, and J. Lloret, "Short-Term Load Forecasting for Microgrids Based on Artificial Neural Networks," *Energies*, vol. 6, no. 3, p. 1385, 2013.

[21] P. Basak, A. K. Saha, S. Chowdhury, and S. P. Chowdhury, "Microgrid: Control techniques and modeling," in *2009 44th International Universities Power Engineering Conference (UPEC)*, 2009, pp. 1-5.

[22] A. Bonfiglio *et al.*, "An optimization algorithm for the operation planning of the University of Genoa smart polygeneration microgrid," in *2013 IREP Symposium Bulk Power System Dynamics and Control - IX Optimization, Security and Control of the Emerging Power Grid*, 2013.
[23] X. Hou, Y. Sun, W. Yuan, H. Han, C. Zhong, and J. Guerrero, "Conventional P-ω/Q-V Droop Control in Highly Resistive Line of Low-Voltage Converter-Based AC Microgrid," *Energies*, vol. 9, no. 11, p. 943, 2016.
[24] M. C. Chandorkar, D. M. Divan, and R. Adapa, "Control of parallel connected inverters in standalone AC supply systems," *IEEE Transactions on Industry Applications*, vol. 29, no. 1, pp. 136-143, 1993.
[25] A. Labella, D. Mestriner, R. Procopio, and M. Brignone, "A new method to evaluate the stability of a droop controlled micro grid," in *2017 10th International Symposium on Advanced Topics in Electrical Engineering (ATEE)*, 2017, pp. 448-453.
[26] A. Bidram and A. Davoudi, "Hierarchical Structure of Microgrids Control System," *IEEE Transactions on Smart Grid*, vol. 3, no. 4, pp. 1963-1976, 2012.
[27] J. M. Guerrero, P. Chiang Loh, T.-L. Lee, and M. Chandorkar, "Advanced Control Architectures for Intelligent Microgrids—Part II," *IEEE Transactions on Industrial Electronics*, vol. 60, pp. 1263-1270, 2013.
[28] J. M. Guerrero, M. Chandorkar, T. L. Lee, and P. C. Loh, "Advanced control architectures for intelligent microgrids—Part I: Decentralized and hierarchical control," *IEEE Transactions on Industrial Electronics*, vol. 60, no. 4, pp. 1254-1262, 2013.
[29] X. Su, M. Han, J. Guerrero, and H. Sun, "Microgrid Stability Controller Based on Adaptive Robust Total SMC," *Energies*, vol. 8, no. 3, p. 1784, 2015.
[30] M. Chlela, D. Mascarella, G. Joos, and M. Kassouf, "Fallback Control for Isochronous Energy Storage Systems in Autonomous Microgrids Under Denial-of-Service Cyber-Attacks," *IEEE Transactions on Smart Grid*, vol. PP, no. 99, pp. 1-1, 2017.
[31] S. Xiao, L. Yim-Shu, and X. Dehong, "Modeling, analysis, and implementation of parallel multi-inverter systems with instantaneous average-current-sharing scheme," *IEEE Transactions on Power Electronics*, vol. 18, no. 3, pp. 844-856, 2003.
[32] A. Parisio, E. Rikos, and L. Glielmo, "A Model Predictive Control Approach to Microgrid Operation Optimization," *IEEE Transactions on Control Systems Technology*, vol. 22, no. 5, pp. 1813-1827, 2014.
[33] T.-T. Nguyen, H.-J. Yoo, and H.-M. Kim, "Analyzing the Impacts of System Parameters on MPC-Based Frequency Control for a Stand-Alone Microgrid," *Energies*, vol. 10, no. 4, p. 417, 2017.
[34] T. Kerdphol, F. Rahman, Y. Mitani, K. Hongesombut, and S. Küfeoğlu, "Virtual Inertia Control-Based Model Predictive Control for Microgrid Frequency Stabilization Considering High Renewable Energy Integration," *Sustainability*, vol. 9, no. 5, p. 773, 2017.
[35] A. Bonfiglio, F. Delfino, M. Invernizzi, A. Perfumo, and R. Procopio, "A feedback linearization scheme for the control of synchronous generators," *Electric Power Components and Systems*, Article vol. 40, no. 16, pp. 1842-1869, 2012.
[36] A. Bonfiglio, F. Delfino, F. Pampararo, R. Procopio, M. Rossi, and L. Barillari, "The Smart Polygeneration Microgrid test-bed facility of Genoa University," in *Proceedings of the Universities Power Engineering Conference*, 2012.
[37] *Council of the European Union*. Available: http://www.consilium.europa.eu/uedocs/cms_data/docs/pressdata/en/ec/93135.pdf
[38] U. Böke, "A simple model of photovoltaic module electric characteristics," in *European Conference on Power Electronics and Applications*, 2007.
[39] FIAMM. *SoNick ST523*. Available: fiamm.com/media/20150209-st523_datasheet.pdf
[40] I. Rexed, M. Behm, and G. Lindbergh, "Modelling of ZEBRA Batteries," Royal Institute of Technology2010.

[41] J. L. Sudworth, "Zebra batteries," *Journal of Power Sources*, vol. 51, pp. 105-114, 1994.
[42] M. Seyedmahmoudian, S. Mekhilef, R. Rahmani, R. Yusof, and E. Renani, "Analytical Modeling of Partially Shaded Photovoltaic Systems," *Energies*, vol. 6, no. 1, p. 128, 2013.
[43] R. Erickson and D. Maksimovic, *Fundamentals of Power Electronics,2nd edition*. Kluwer Academic, 2004.
[44] P. Kundur, N. J. Balu, and M. G. Lauby, *Power system stability and control*. McGraw-Hill, 1994.
[45] A. Labella, D. Mestriner, R. Procopio, and F. Delfino, "A simplified first harmonic model for the Savona Campus Smart Polygeneration Microgrid," in *2017 IEEE International Conference on Environment and Electrical Engineering and 2017 IEEE Industrial and Commercial Power Systems Europe (EEEIC / I&CPS Europe)*, 2017, pp. 1-6.
[46] X. Guo, Z. Lu, B. Wang, X. Sun, L. Wang, and J. M. Guerrero, "Dynamic Phasors-Based Modeling and Stability Analysis of Droop-Controlled Inverters for Microgrid Applications," *IEEE Transactions on Smart Grid*, vol. 5, no. 6, pp. 2980-2987, 2014.
[47] A. M. Stankovic, B. C. Lesieutre, and T. Aydin, "Modeling and analysis of single-phase induction machines with dynamic phasors," *IEEE Transactions on Power Systems*, vol. 14, no. 1, pp. 9-14, 1999.
[48] F. Milano, *Power system modelling and scripting*. Springer Science & Business Media, 2010.
[49] DuncanInstruments. Available: duncaninstr.com/Jupiter.htm
[50] Fluke. Available: fluke.com/products/portable-oscilloscopes/fluke-190-ii-portable-oscilloscope-190-104-s.html
[51] Y. Song, D. J. Hill, T. Liu, and Y. Zheng, "A Distributed Framework for Stability Evaluation and Enhancement of Inverter-Based Microgrids," *IEEE Transactions on Smart Grid*, vol. 8, no. 6, pp. 3020-3034, 2017.
[52] R. Majumder, "Some Aspects of Stability in Microgrids," *IEEE Transactions on Power Systems*, vol. 28, no. 3, pp. 3243-3252, 2013.
[53] F. Katiraei, M. R. Iravani, and P. W. Lehn, "Micro-grid autonomous operation during and subsequent to islanding process," *IEEE Transactions on Power Delivery*, vol. 20, no. 1, pp. 248-257, 2005.
[54] P. Krause, O. Wasynczuk, S. D. Sudhoff, and S. Pekarek, *Analysis of electric machinery and drive systems*. John Wiley & Sons, 2013.
[55] N. Bottrell, M. Prodanovic, and T. C. Green, "Dynamic Stability of a Microgrid With an Active Load," *IEEE Transactions on Power Electronics*, vol. 28, no. 11, pp. 5107-5119, 2013.
[56] A. Kahrobaeian and Y. A. R. I. Mohamed, "Analysis and Mitigation of Low-Frequency Instabilities in Autonomous Medium-Voltage Converter-Based Microgrids With Dynamic Loads," *IEEE Transactions on Industrial Electronics*, vol. 61, no. 4, pp. 1643-1658, 2014.
[57] P. Kundur *et al.*, "Definition and classification of power system stability IEEE/CIGRE joint task force on stability terms and definitions," *IEEE Transactions on Power Systems*, vol. 19, no. 3, pp. 1387-1401, 2004.
[58] L. Luo and S. V. Dhople, "Spatiotemporal Model Reduction of Inverter-Based Islanded Microgrids," *IEEE Transactions on Energy Conversion*, vol. 29, no. 4, pp. 823-832, 2014.
[59] M. Kabalan, P. Singh, and D. Niebur, "Large Signal Lyapunov-Based Stability Studies in Microgrids: A Review," *IEEE Transactions on Smart Grid*, vol. 8, no. 5, pp. 2287-2295, 2017.
[60] K. F. Krommydas and A. T. Alexandridis, "Modular Control Design and Stability Analysis of Isolated PV-Source/Battery-Storage Distributed Generation Systems,"

IEEE Journal on Emerging and Selected Topics in Circuits and Systems, vol. 5, no. 3, pp. 372-382, 2015.

[61] F. Hamidi and H. Jerbi, "On the estimation of a maximal Lyapunov function and domain of attraction determination via a genetic algorithm," in *2009 6th International Multi-Conference on Systems, Signals and Devices*, 2009, pp. 1-6.

[62] D. Marx, P. Magne, B. Nahid-Mobarakeh, S. Pierfederici, and B. Davat, "Large Signal Stability Analysis Tools in DC Power Systems With Constant Power Loads and Variable Power Loads—A Review," *IEEE Transactions on Power Electronics*, vol. 27, no. 4, pp. 1773-1787, 2012.

[63] F. Andrade, K. Kampouropoulos, L. Romeral, J. C. Vasquez, and J. M. Guerrero, "Study of large-signal stability of an inverter-based generator using a Lyapunov function," in *IECON 2014 - 40th Annual Conference of the IEEE Industrial Electronics Society*, 2014, pp. 1840-1846.

[64] F. A. Rengifo, L. Romeral, J. Cusidó, and J. J. Cárdenas, "New Model of a Converter-Based Generator Using Electrostatic Synchronous Machine Concept," *IEEE Transactions on Energy Conversion*, vol. 29, no. 2, pp. 344-353, 2014.

[65] P. Hart and B. Lesieutre, "Energy function for a grid-tied, droop-controlled inverter," in *2014 North American Power Symposium (NAPS)*, 2014, pp. 1-6.

[66] Y. Han, H. Li, P. Shen, E. A. A. Coelho, and J. M. Guerrero, "Review of Active and Reactive Power Sharing Strategies in Hierarchical Controlled Microgrids," *IEEE Transactions on Power Electronics*, vol. 32, no. 3, pp. 2427-2451, 2017.

[67] K. Yu, Q. Ai, S. Wang, J. Ni, and T. Lv, "Analysis and Optimization of Droop Controller for Microgrid System Based on Small-Signal Dynamic Model," *IEEE Transactions on Smart Grid*, vol. 7, no. 2, pp. 695-705, 2016.

[68] Y. Pan, L. Chen, X. Lu, J. Wang, F. Liu, and S. Mei, "Stability Region of Droop-Controlled Distributed Generation in Autonomous Microgrids," *IEEE Transactions on Smart Grid*, pp. 1-1, 2018.

[69] N. Pogaku, M. Prodanovic, and T. C. Green, "Modeling, Analysis and Testing of Autonomous Operation of an Inverter-Based Microgrid," *IEEE Transactions on Power Electronics*, vol. 22, no. 2, pp. 613-625, 2007.

[70] A. Bonfiglio *et al.*, "Modeling and Experimental Validation of an Islanded No-Inertia Microgrid Site," *IEEE Transactions on Sustainable Energy*, vol. 9, no. 4, pp. 1812-1821, 2018.

[71] A. Bonfiglio, M. Brignone, M. Invernizzi, A. Labella, D. Mestriner, and R. Procopio, "A Simplified Microgrid Model for the Validation of Islanded Control Logics," *Energies*, vol. 10, no. 8, p. 1141, 2017.

[72] J. J. E. Slotine and W. Li, *Applied nonlinear control*. Englewood Cliffs, N.J.: Prentice Hall, 1991, pp. xv, 459 p.

[73] D. Ernst, D. Ruiz-Vega, M. Pavella, P. M. Hirsch, and D. Sobajic, "A unified approach to transient stability contingency filtering, ranking and assessment," *IEEE Transactions on Power Systems*, vol. 16, no. 3, pp. 435-443, 2001.

[74] A. M. Dissanayake and N. C. Ekneligoda, "Transient Optimization of Parallel Connected Inverters in Islanded AC Microgrids," *IEEE Transactions on Smart Grid*, pp. 1-1, 2018.

[75] H. Han, X. Hou, J. Yang, J. Wu, M. Su, and J. M. Guerrero, "Review of Power Sharing Control Strategies for Islanding Operation of AC Microgrids," *IEEE Transactions on Smart Grid*, vol. 7, no. 1, pp. 200-215, 2016.

[76] T. Vandoorn, J. De Kooning, B. Meersman, and L. Vandevelde, "Review of primary control strategies for islanded microgrids with power-electronic interfaces," *Renewable and Sustainable Energy Reviews*, vol. 19, pp. 613-628, 2013.

[77] A. Mortezaei, M. G. Simões, M. Savaghebi, J. M. Guerrero, and A. Al-Durra, "Cooperative Control of Multi-Master–Slave Islanded Microgrid With Power Quality Enhancement Based on Conservative Power Theory," *IEEE Transactions on Smart Grid*, vol. 9, no. 4, pp. 2964-2975, 2018.

[78] S. Peyghami, H. Mokhtari, P. C. Loh, P. Davari, and F. Blaabjerg, "Distributed Primary and Secondary Power Sharing in a Droop-Controlled LVDC Microgrid With Merged AC and DC Characteristics," *IEEE Transactions on Smart Grid*, vol. 9, no. 3, pp. 2284-2294, 2018.
[79] J. Rocabert, A. Luna, F. Blaabjerg, and P. Rodriguez, "Control of power converters in AC microgrids," *IEEE transactions on power electronics*, vol. 27, no. 11, pp. 4734-4749, 2012.
[80] N. Hatziargyriou, *Microgrids: architectures and control*. John Wiley & Sons, 2014.
[81] Y. Ghiassi-Farrokhfal, F. Kazhamiaka, C. Rosenberg, and S. Keshav, "Optimal Design of Solar PV Farms With Storage," *IEEE Transactions on Sustainable Energy*, vol. 6, no. 4, pp. 1586-1593, 2015.
[82] I. Bendato *et al.*, "Design criteria for the optimal sizing of integrated photovoltaic-storage systems," *Energy*, vol. 149, pp. 505-515, 2018/04/15/ 2018.
[83] K. Sun, L. Zhang, Y. Xing, and J. M. Guerrero, "A Distributed Control Strategy Based on DC Bus Signaling for Modular Photovoltaic Generation Systems With Battery Energy Storage," *IEEE Transactions on Power Electronics*, vol. 26, no. 10, pp. 3032-3045, 2011.
[84] H. Mahmood, D. Michaelson, and J. Jiang, "Decentralized Power Management of a PV/Battery Hybrid Unit in a Droop-Controlled Islanded Microgrid," *IEEE Transactions on Power Electronics*, vol. 30, no. 12, pp. 7215-7229, 2015.
[85] H. Mahmood, D. Michaelson, and J. Jiang, "A Power Management Strategy for PV/Battery Hybrid Systems in Islanded Microgrids," *IEEE Journal of Emerging and Selected Topics in Power Electronics*, vol. 2, no. 4, pp. 870-882, 2014.
[86] S. Adhikari and F. Li, "Coordinated V-f and P-Q Control of Solar Photovoltaic Generators With MPPT and Battery Storage in Microgrids," *IEEE Transactions on Smart Grid*, vol. 5, no. 3, pp. 1270-1281, 2014.
[87] M. Mao, C. Qian, and Y. Ding, "Decentralized coordination power control for islanding microgrid based on PV/BES-VSG," *CPSS Transactions on Power Electronics and Applications*, vol. 3, no. 1, pp. 14-24, 2018.
[88] D. Wu, F. Tang, T. Dragicevic, J. C. Vasquez, and J. M. Guerrero, "Autonomous Active Power Control for Islanded AC Microgrids With Photovoltaic Generation and Energy Storage System," *IEEE Transactions on Energy Conversion*, vol. 29, no. 4, pp. 882-892, 2014.
[89] Y. Shan, J. Hu, Z. Li, and J. M. Guerrero, "A Model Predictive Control for Renewable Energy Based AC Microgrids Without Any PID Regulators," *IEEE Transactions on Power Electronics*, vol. 33, no. 11, pp. 9122-9126, 2018.
[90] A. L. Bella, S. R. Cominesi, C. Sandroni, and R. Scattolini, "Hierarchical Predictive Control of Microgrids in Islanded Operation," *IEEE Transactions on Automation Science and Engineering*, vol. 14, no. 2, pp. 536-546, 2017.
[91] C. A. Hans, P. Braun, J. Raisch, L. Grune, and C. Reincke-Collon, "Hierarchical Distributed Model Predictive Control of Interconnected Microgrids," *IEEE Transactions on Sustainable Energy*, pp. 1-1, 2018.
[92] A. Bonfiglio, F. Delfino, M. Invernizzi, R. Procopio, and P. Serra, "An approximate methodology to verify the compliance of large photovoltaic power plants to system operator steady-state requirements," *Electric Power Systems Research*, Article vol. 127, pp. 80-92, 2015, Art. no. 4337.
[93] Z. Styczynski, P. Lombardi, R. Seethapathy, M. Piekutowski, C. Ohler, and B. Roberts, "Electric energy storage systems," *CIGRE Working group C*, vol. 6, 2011.
[94] F. Allgöwer and A. Zheng, *Nonlinear model predictive control*. Birkhäuser, 2012.
[95] A. Bonfiglio *et al.*, "Modeling and Experimental Validation of an Islanded No-Inertia Microgrid Site," *IEEE Transactions on Sustainable Energy*, pp. 1-1, 2018.
[96] A. Bonfiglio, M. Brignone, F. Delfino, M. Invernizzi, F. Pampararo, and R. Procopio, "A technique for the optimal control and operation of grid-connected photovoltaic

production units," in *Proceedings of the Universities Power Engineering Conference*, 2012.
[97] N. Mohan and T. M. Undeland, *Power electronics: converters, applications, and design*. John wiley & sons, 2007.
[98] A. Smets, K. Jäger, O. Isabella, M. Zeman, and R. van Swaaij, *Solar Energy: The Physics and Engineering of Photovoltaic Conversion, Technologies and Systems*. UIT Cambridge, 2016.
[99] "IEEE Guide for Design, Operation, and Integration of Distributed Resource Island Systems with Electric Power Systems," *IEEE Std 1547.4-2011*, pp. 1-54, 2011.
[100] J. Rocabert, A. Luna, F. Blaabjerg, and P. Rodríguez, "Control of Power Converters in AC Microgrids," *IEEE Transactions on Power Electronics*, vol. 27, no. 11, pp. 4734-4749, 2012.
[101] J. Viinamäki, A. Kuperman, and T. Suntio, "Grid-Forming-Mode Operation of Boost-Power-Stage Converter in PV-Generator-Interfacing Applications," vol. 10, no. 7, p. 1033, 2017.
[102] I. L. S. M. D. P. DGCP and I. M. H. PE, "Assessment of DER Interconnection Installation for Conformance with IEEE Std 1547," *Assessment of DER Interconnection Installation for Conformance with IEEE Std 1547*, pp. 1-18, 2018.
[103] *CEI 0-16 - Technical rules for the connection of active passive consumers to the HV MV electrical networks of distribution Company*, 2008.
[104] IEEE, "IEEE Standard for Interconnection and Interoperability of Distributed Energy Resources with Associated Electric Power Systems Interfaces," *IEEE Std 1547-2018 (Revision of IEEE Std 1547-2003)*, pp. 1-138, 2018.
[105] A. M. Bouzid *et al.*, "A survey on control of electric power distributed generation systems for microgrid applications," vol. 44, pp. 751-766, 2015.
[106] M. Petronijević, N. Mitrović, V. Kostić, and B. Banković, "An Improved Scheme for Voltage Sag Override in Direct Torque Controlled Induction Motor Drives," *Energies*, vol. 10, no. 5, 2017.
[107] H. J. Ferreau, C. Kirches, A. Potschka, H. G. Bock, and M. Diehl, "qpOASES: a parametric active-set algorithm for quadratic programming," *Mathematical Programming Computation*, vol. 6, no. 4, pp. 327-363, 2014/12/01 2014.
[108] H. J. Ferreau, H. G. Bock, and M. Diehl, "An online active set strategy to overcome the limitations of explicit MPC," *International Journal of Robust*

Nonlinear Control, vol. 18, no. 8, pp. 816-830, 2008.
[109] W. W. E. A. Statistics. (2017). *WORLD WIND MARKET HAS REACHED 486 GW*. Available: http://www.wwindea.org/11961-2/
[110] P. Tielens and D. Van Hertem, "The relevance of inertia in power systems," (in English), *Renewable & Sustainable Energy Reviews*, vol. 55, pp. 999-1009, Mar 2016.
[111] ENTSO-E, "Requirements for Grid Connection Applicable to all Generators," *European Network of Transmission System Operators for Electricity, ENTSO-E (2013 March)*, 2013.
[112] EirGrid, "A proposal for Rate of Change of Frequency Remuneration Mechanism Recommendations," *(2016 May)*, 2016.
[113] G. Delille, B. Francois, and G. Malarange, "Dynamic Frequency Control Support by Energy Storage to Reduce the Impact of Wind and Solar Generation on Isolated Power System's Inertia," *IEEE Transactions on Sustainable Energy*, vol. 3, no. 4, pp. 931-939, 2012.
[114] M. Dreidy, H. Mokhlis, and S. Mekhilef, "Inertia response and frequency control techniques for renewable energy sources: A review," *Renewable and Sustainable Energy Reviews*, vol. 69, no. Supplement C, pp. 144-155, 2017/03/01/ 2017.
[115] J. Morren, J. Pierik, and S. W. H. de Haan, "Inertial response of variable speed wind turbines," *Electric Power Systems Research*, vol. 76, no. 11, pp. 980-987, 2006/07/01/ 2006.

[116] J. V. d. Vyver, J. D. Kooning, B. Meersman, L. Vandevelde, and T. L. Vandoorn, "Droop Control as an Alternative Inertial Response Strategy for the Synthetic Inertia on Wind Turbines," *IEEE Transactions on Power Systems*, vol. 31, no. 2, pp. 1129-1138, 2016.
[117] K. V. Vidyanandan and N. Senroy, "Primary frequency regulation by deloaded wind turbines using variable droop," *IEEE Transactions on Power Systems*, vol. 28, no. 2, pp. 837-846, 2013.
[118] F. Gonzalez-Longatt, E. Chikuni, and E. Rashayi, "Effects of the Synthetic Inertia from wind power on the total system inertia after a frequency disturbance," in *2013 IEEE International Conference on Industrial Technology (ICIT)*, 2013, pp. 826-832.
[119] A. D. Hansen, M. Altin, I. D. Margaris, F. Iov, and G. C. Tarnowski, "Analysis of the short-term overproduction capability of variable speed wind turbines," *Renewable Energy*, vol. 68, no. Supplement C, pp. 326-336, 2014/08/01/ 2014.
[120] F. M. Gonzalez-Longatt, A. Bonfiglio, R. Procopio, and B. Verduci, "Evaluation of inertial response controllers for full-rated power converter wind turbine (Type 4)," in *IEEE Power and Energy Society General Meeting*, 2016, vol. 2016-November.
[121] F. Gonzalez-Longatt, A. Bonfiglio, R. Procopio, and D. Bogdanov, "Practical limit of synthetic inertia in full converter wind turbine generators: Simulation approach," in *2016 19th International Symposium on Electrical Apparatus and Technologies, SIELA 2016*, 2016.
[122] Z. Wu, D. W. Gao, H. Zhang, S. Yan, and X. Wang, "Coordinated Control Strategy of Battery Energy Storage System and PMSG-WTG to Enhance System Frequency Regulation Capability," *IEEE Transactions on Sustainable Energy*, vol. 8, no. 3, pp. 1330-1343, 2017.
[123] L. Wu and D. G. Infield, "Towards an Assessment of Power System Frequency Support From Wind Plant - Modeling Aggregate Inertial Response," *IEEE Transactions on Power Systems*, vol. 28, no. 3, pp. 2283-2291, 2013.
[124] J. Morren, S. W. H. d. Haan, W. L. Kling, and J. A. Ferreira, "Wind turbines emulating inertia and supporting primary frequency control," *IEEE Transactions on Power Systems*, vol. 21, no. 1, pp. 433-434, 2006.
[125] J. M. Mauricio, A. Marano, A. Gomez-Exposito, and J. L. M. Ramos, "Frequency Regulation Contribution Through Variable-Speed Wind Energy Conversion Systems," *IEEE Transactions on Power Systems*, vol. 24, no. 1, pp. 173-180, 2009.
[126] F. Liu, Z. Liu, S. Mei, W. Wei, and Y. Yao, "ESO-Based Inertia Emulation and Rotor Speed Recovery Control for DFIGs," *IEEE Transactions on Energy Conversion*, vol. 32, no. 3, pp. 1209-1219, 2017.
[127] F. M. Gonzalez-Longatt, "Activation schemes of synthetic inertia controller for full converter wind turbine generators," in *PowerTech, 2015 IEEE Eindhoven*, 2015, pp. 1-5.
[128] F. Gonzalez-Longatt, "Frequency Control and Inertial Response Schemes for the Future Power Networks," in *Large Scale Renewable Power Generation*, J. Hossain and A. Mahmud, Eds. (Green Energy and Technology: Springer Singapore, 2014, pp. 193-231.
[129] F. M. Gonzalez-Longatt, "Impact of emulated inertia from wind power on under-frequency protection schemes of future power systems," (in English), *Journal of Modern Power Systems and Clean Energy*, pp. 1-8, 2015/08/12 2015.
[130] G. Lalor, A. Mullane, and M. O'Malley, "Frequency control and wind turbine technologies," *Power Systems, IEEE Transactions on*, vol. 20, no. 4, pp. 1905-1913, 2005.
[131] N. Miller, K. Clark, and R. Walling, "WindINERTIA: Controlled Inertial Response from GE Wind Turbine Generators," presented at the 45th Annual Minnesota Power Systems Conference, Minneapolis, Minnesota, 2009.
[132] S. Wachtel and A. Beekmann, "Contribution of Wind Energy Converters with Inertia Emulation to Frequency Control and Frequency Stability in Power Systems,"

presented at the 8th International Workshop on Large-Scale Integration of Wind Power into Power Systems as well as on Transmission Networks for Offshore Wind Farms, Bremen, Germany, 14 – 15 October, 2009, 2009.
[133] F. Gonzalez-Longatt and J. M. Roldan, "Effects of dc voltage control strategies of voltage response on multi-terminal HVDC following a disturbance," in *Universities Power Engineering Conference (UPEC), 2012 47th International*, 2012, pp. 1-6.
[134] J. Ekanayake and N. Jenkins, "Comparison of the response of doubly fed and fixed-speed induction generator wind turbines to changes in network frequency," *Energy Conversion, IEEE Transactions on*, vol. 19, no. 4, pp. 800-802, 2004.
[135] J. Morren, S. W. H. de Haan, W. L. Kling, and J. A. Ferreira, "Wind turbines emulating inertia and supporting primary frequency control," *Power Systems, IEEE Transactions on*, vol. 21, no. 1, pp. 433-434, 2006.
[136] A. Bonfiglio, F. Delfino, M. Invernizzi, and R. Procopio, "Modeling and maximum power point tracking control of wind generating units equipped with permanent magnet synchronous generators in presence of losses," *Energies*, vol. 10, no. 1, p. 102, 2017.
[137] A. Bonfiglio, F. Delfino, F. Gonzalez-Longatt, and R. Procopio, "Steady-state assessments of PMSGs in wind generating units," *International Journal of Electrical Power & Energy Systems*, vol. 90, pp. 87-93, 2017/09/01/ 2017.
[138] J. G. Slootweg, "Representing distributed resources in power system dynamics simulations," in *Power Engineering Society Summer Meeting, 2002 IEEE*, 2002, vol. 1, pp. 176-178 vol.1.
[139] O. Anaya-Lara, *Wind energy generation : modelling and control*. Oxford: Wiley, 2009, pp. xvii, 269 p.
[140] ENTSO-E, "Need for synthetic inertia for frequency regulation," March 2016.
[141] ENTSO-E, "Frequency Stability Evaluation Criteria for the Synchronous Zone of Continental Europe," March 2016.
[142] P. Energy, "Rate of Change of Frequency (ROCOF)-Review of TSO and Generator Submissions Final Report," *Commission for Energy Regulation (CER)*, 2013.
[143] (2016). *Requirements for grid connection of generators*. Available: http://eur-lex.europa.eu/legal-content/EN/TXT/PDF/?uri=CELEX:32016R0631&from=EN
[144] A. Adamczyk, M. Altin, G. Ö, R. Teodorescu, and F. Iov, "Generic 12-bus test system for wind power integration studies," in *2013 15th European Conference on Power Electronics and Applications (EPE)*, 2013, pp. 1-6.
[145] P. M. Anderson and A. A. Fouad, *Power System Control and Stability, 2nd ED.* Wiley India Pvt. Limited, 2008.